

1972

Gamma decay of states excited by 300 and 600 MeV protons on targets of boron, carbon, nitrogen, oxygen, magnesium, and calcium

Max David Holt
College of William & Mary - Arts & Sciences

Follow this and additional works at: <https://scholarworks.wm.edu/etd>



Part of the [Physics Commons](#)

Recommended Citation

Holt, Max David, "Gamma decay of states excited by 300 and 600 MeV protons on targets of boron, carbon, nitrogen, oxygen, magnesium, and calcium" (1972). *Dissertations, Theses, and Masters Projects*. Paper 1539623322.

<https://dx.doi.org/doi:10.21220/s2-nyxk-zc10>

This Dissertation is brought to you for free and open access by the Theses, Dissertations, & Master Projects at W&M ScholarWorks. It has been accepted for inclusion in Dissertations, Theses, and Masters Projects by an authorized administrator of W&M ScholarWorks. For more information, please contact scholarworks@wm.edu.

GAMMA DECAY OF STATES EXCITED BY 300 AND
600 MeV PROTONS ON TARGETS OF BORON,
CARBON, NITROGEN, OXYGEN,
MAGNESIUM, AND CALCIUM

A Thesis

Presented to

The Faculty of the Department of Physics
The College of William and Mary in Virginia

In Partial Fulfillment
Of the Requirements for the Degree of
Doctor of Philosophy

by

Max David Holt

May, 1972

APPROVAL SHEET

This thesis is submitted in partial fulfillment of
the requirements for the degree of
Doctor of Philosophy

Max David Holt

Max David Holt

Approved, May, 1972

Herbert O. Funsten

Herbert O. Funsten

Richard L. Kiefer

Richard L. Kiefer

W. J. Kosler

W.J. Kosler

Hans C. von Baeyer

Hans C. von Baeyer

Robert E. Welsh

Robert E. Welsh

552185 ..

TABLE OF CONTENTS

	Page
ACKNOWLEDGMENTS	iv
LIST OF TABLES	v
LIST OF FIGURES	vii
I. INTRODUCTION	2
II. EXPERIMENTAL METHOD	6
A. Geometry and Counters	
B. Proton Beam Flux	
C. Detector Efficiency and Energy Calibration	
D. Neutron Contamination	
E. Targets	
III. DATA ANALYSIS	16
IV. EXPERIMENTAL ERRORS	18
V. EXPERIMENTAL RESULTS	21
A. Boron Target	
B. Carbon Target	
C. Nitrogen Target	
D. Oxygen Target	
E. Magnesium Target	
F. Calcium Target	
VI. THEORETICAL CONSIDERATIONS	30
A. Inelastic Scattering	
B. Doppler Broadened γ -rays-Spectrum Shape for Inelastic Scattering	
C. Comparisons of Line Shapes with Experiment	
VII. COMPARISONS WITH OTHER EXPERIMENTS	47
VIII. CONCLUSIONS	52

IX. APPENDIX 60

- A. Tables
- B. Figures
 - Figure Captions
- C. Pulse Shape Discrimination
- D. Charge Sensitive Preamplifier
- E. Compensated Timing Circuit

ACKNOWLEDGMENTS

The author wishes to acknowledge the contributions and support of the following persons:

Dr. H. O. Funsten, his advisor, for continued encouragement and assistance during all phases of the project.

Dr. R. E. Welsh for advice while writing the manuscript and for careful readings and comments thereon.

Dr. J. Kossler for readings of the manuscript and helpful suggestions.

Dr. Joe Lieb who assisted with data taking and reduction.

Dr. R. T. Siegel, his employer while much of the manuscript was being written, for constant encouragement.

Dr. von Baeyer and R. Keifer for reading the manuscript.

Mr. Stanely Hummel and the William and Mary Machine Shop staff for fabrication of plastic scintillation counters.

Mr. Sherwin Beck for use of the Ge(Li) detector.

The operations personnel of The Space Radiation Effects Laboratory for maintaining the accelerator in a most unweildy mode of operation.

This research was supported, in part, by the National Aeronautics and Space Administration.

LIST OF TABLES

Table	Page
1. Integrated Proton Flux	61
2. Calibration Sources	62
3. Neutron Background	63
4. Target Specifications	64
5. Energy Uncertainties	65
6. Cross Section Uncertainties	66
7. Results of Boron Target (300 MeV)	67
8. Results of Carbon Target (300 MeV)	69
9. Results of Carbon Target (600 MeV)	70
10. Results of Nitrogen Target (300 MeV)	72
11. Results of Oxygen Target (300 MeV)	73
12. Results of Oxygen Target (600 MeV)	75
13. Results of Magnesium Target (300 MeV)	77
14. Level Cross Section in ^{23}Mg and ^{23}Na	80
15. Results of Calcium Target (300 MeV)	81
16. Comparisons of Cross Sections in Boron	85
17. Comparisons of Cross Sections in Carbon	87
18. Comparisons of Cross Sections in Nitrogen	89
19. Comparisons of Cross Sections in Oxygen	90
20. Comparisons of Cross Sections in Magnesium	92

Table	Page
21. Comparisons of Cross Sections in Calcium	94
22. Characteristics of Fast Amplification Stages	96
23. Characteristics of Charge-Sensitive Preamplifier	97

LIST OF FIGURES

Figure	Page
1. Experimental Area	101
2. Block Diagram--Logic and Linear Electronics	101
3. External Proton Beam Layout	102
4. Effects of Pulse Pileup	103
5. γ -ray Detector Efficiency	104
6. γ rays from Boron-300 MeV Protons	105
7. γ rays from Carbon-300 MeV Protons	106
8. γ rays from Carbon-600 MeV Protons	107
9. γ rays from Nitrogen-300 MeV Protons	108
10. γ rays from Oxygen-300 MeV Protons	109
11. γ rays from Oxygen-300 MeV Protons	110
12. γ rays from Magnesium-300 MeV Protons	111
13. γ rays from Calcium-300 MeV Protons	112
14. Proton Differential Cross Section	113
15. Calculated γ ray Spectrum	114
16. 4.44 MeV Line of ^{12}C	115
17. 4.49 MeV Line of ^{11}B	116
18. Germanium Detector	117
19. Timing with Doubly Differentiated Signals	117
20. Variations in Pulse Shapes out of Germanium Detector	118

Figure	Page
21. Pulse Shape Discrimination	119
22. Block Diagram of Pulse Shape Discriminator	120
23. Schematic Diagrams of Fast Shaping Amplifier	121
24. Pulse Shape Discriminator	122
25. Effect of Pulse Shape Discrimination	123
26. Charge Sensitive Amplifier	124
27. Schematic Diagram of Preamplifier	125
28. Compensation for Timing Errors	126
29. Diagram of Timing Circuit	127

ABSTRACT

De-excitation γ rays from medium energy proton bombardment of boron, carbon, nitrogen, oxygen, magnesium, and calcium targets have been investigated with a high resolution detection system. Good energy resolution allowed investigation of the effects of Doppler broadening of the γ rays owing to the recoil of the excited nucleus. The peak shapes produced by inelastic (p,p') scattering have been compared to the simple predictions of the plane wave impulse approximation. Energies, widths, and cross sections were determined for all targets with 300 MeV protons incident and for carbon and oxygen with 600 MeV protons. These results complement quasielastic $(p,2p)$ experiments of similar incident energies and allow comparison with lower-energy pickup reactions.

Max David Holt

Department of Physics

The College of William and Mary

GAMMA DECAY OF STATES EXCITED BY 300 AND
600 MeV PROTONS ON TARGETS OF BORON,
CARBON, NITROGEN, OXYGEN,
MAGNESIUM, AND CALCIUM

I. INTRODUCTION

In the early 1960s, Clegg and co-workers^{1,2,3,4,5,6,7} did an extensive survey of the gamma decay of nuclear states excited by medium energy protons. The 150 MeV Harwell Synchrocyclotron was used in these experiments. The de-excitation γ rays were observed using NaI crystals. Previous studies involving level structure had been conducted by measuring the energy spectrum of the particles in the exit channel. This was not practical at the higher incident energies because of the poorer energy resolution of the incident beam. The Clegg experiments thus supplemented the results of the charged particle work at lower energies. Several features were prominent in most of these investigations:

1. the number of states observed was relatively small with, in general, only two or three levels in the target nucleus excited,
2. reactions in which apparent clusters were knocked out of the nucleus were frequently observed, and
3. the γ -ray angular correlation with respect to the recoiling nucleus were consistent with a direct interaction interpretation.

The recent development of solid state detectors with resolution far superior to the NaI detectors (roughly a factor of 30 at

1 MeV γ -ray energy) has led to a continuance of these experiments.

The superior resolution of Ge(Li) detectors has many distinct experimental advantages:

1. the γ -ray energy is more accurately determined,
2. the spectral features are much less ambiguous allowing more definite assignments,
3. since the peak to background ratio is greatly improved, observance of weaker transitions should be possible, and
4. the line shapes may give additional information.

Photons emitted while the target nuclei are recoiling from the interaction will be shifted in energy due to the Doppler effect. The occurrence of this effect is dependent on:

1. the differential cross section for the interaction,
2. the lifetime of the excited nuclear state, and
3. the angular correlation of the de-excitation γ ray with respect to the recoiling nucleus.

If the details of the γ -ray line shapes are measured, there should be evidence of the influence of each of the above.

The work of Clegg indicated that several reactions should be expected. Prevalent among these are inelastic scattering, single-particle knockout, and possible cluster knockout. In the case of the knockout reactions, the spectrum shape should yield information about the internal momentum of nucleons in the target nuclei.

The experiment described was run at the Space Radiation Effects Laboratory with targets of Boron, Carbon, Nitrogen, Oxygen, Magnesium,

and Calcium. These targets were chosen with the primary hope of studying the lower excited states in inelastic scattering and because of their simple level structure. The proton beams used had energies of 300 and 600 MeV.

No attempt was made to detect the particles in the exit channel. This puts severe restrictions on the γ -ray detection system since all interactions in it will be recorded. Measures taken to preclude unwanted background included.

1. careful selection and shielding of target and detector location,
2. protection against charged particle induced signals in the Ge(Li) detector,
3. analysis of the time distribution of charge delivered by the detector (pulse shape discrimination) which improved the peak to background ratio in the spectra,
4. where possible, acceptance of events only during the beam pulse, and
5. analysis of neutron induced reactions.

These measures allowed acquisition of acceptable spectra while not restricting the reaction to a specific exit channel.

The reactions investigated included inelastic scattering in the target nuclei, single particle knockout to neighboring nuclei, and cluster knockout. In the single particle knockout reactions on even-even target nuclei, analogue states in the mirror nuclei were observed.

This work complements quasielastic (p,2p) experiments of similar energies and can be compared to lower energy pickup reactions. A distinct disadvantage of analysis of pickup type reactions via observance of de-excitation γ rays is that transitions to the ground states of neighboring nuclei are not observed.

At these bombarding energies, the impulse approximation^{8,9,10} should be valid since the wavelength of the incident proton¹¹ ($\approx 10^{-14}$ cm) is much smaller than typical nuclear dimensions. The impulse approximation assumes that the interaction takes place between the struck nucleon and the incident particle with the remainder of the target nucleus acting as a spectator. The direct interaction approach assumes that the momentum of the struck nucleon can be ignored when compared with the energy of the incident particle^{12,13,14,15,16}.

Section II will give the experimental arrangement and conditions. Section III gives details of the data analysis and Section IV is a discussion of the experimental uncertainties. The results of the γ -ray work are presented for each target in Section V. A calculation of the expected line shape due to Doppler broadening for inelastic scattering is given in Section VI. Section VII gives comparisons of this experiment with the results of other workers.

II. EXPERIMENTAL METHOD

A. Geometry and Counters

Figure 1 shows the detector arrangement for the experiments. Protons from the external beam of the SREL cyclotron impinged on the targets. The beam layout for this experiment is shown in Figure 3. The target and detectors were located just upstream of BM3 (beam monitor). The ion chamber of BM3 was used to monitor beam intensity and provide a measure of total proton flux. This target location was chosen to minimize background. It allowed a clear path of 70 feet for the beam after the target and had the lowest neutron background of several locations tested. The beam spot size at the target varied with operating conditions. The best beam spot obtained was .5cm wide by 2cm high. The most diffuse beam was 2.5 by 2.5cm. After traversing the target, the beam passed undeflected through the remainder of the transport system and was stopped in the north shielding wall of the magnet hall. The beam traveled in vacuum to within 3 feet of the target where it exited from the transport system through a .020-inch aluminum window. As indicated in Figure 1, lead shielding protected the germanium detector from protons scattered by the exit window. A 100-gauss field in magnet M4, 20 feet upstream from the target, removed low momentum particles (μ , Π , e) from the beam.

Two distinct proton beams were used with energies of 325 and 590 MeV. Since pulse pile-up of the linear electronics was of much concern, the beam extraction was adjusted to obtain the best possible time duty factor. The 600 MeV beam was extracted by scattering from a stationary internal target. This beam showed no observable time structure. For the 300 MeV beam, careful adjustment of the cyclotron RF cut-off frequency gave an improvement of about a factor of five over the usual spill time (≈ 20 μ sec). The duty factor was monitored by looking at the output of detector C on an oscilloscope. The time structure of the beam consisted of an 80- to 100- μ sec pulse every 18.5 msec. This structure was imposed by the 54 cycle/sec repetition rate of the cyclotron. Each beam pulse contained micro structure with a period of ≈ 59 nsec due to the radio frequency (17 Megahertz) of the accelerator at extraction.

Photons from the target passed through a charged-particle, anti-coincidence detector (A in Figure 1) into the germanium detector. A was a specially constructed, plastic scintillator which enclosed the germanium detector on all but the back side. It was in the shape of a hollow cylinder, closed at one end, of diameter 3-1/4-inch and length 2-inch. The walls and end of the cylinder were of 1/4-inch thick Pilot B scintillator. Light from the scintillator was collected by a lucite light pipe which encircled the "cup" and was viewed by an XP-1020 photo tube.

Counter C was a 6-inch by 6-inch by 1/4-inch plastic scintillator which detected protons scattered from the target at small angles.

The output of this counter was used to monitor the beam intensity and (for the 300 MeV beam) to signal the arrival of the proton burst.

The germanium detector was of planar construction with a depletion depth of 5mm. The front surface area of the detector was $\approx 10\text{cm}^2$ and its active volume was $\approx 4.5\text{cm}^3$. The intrinsic resolution of this detector was 2.5 keV at 1.33 MeV γ -ray energy.

The output of the germanium detector was fed to a special preamplifier (see Appendix D). In order to gain as much information as possible from the time distribution of the detector current, pulse shape discrimination circuitry was located in the experimental area adjacent to the preamplifier. This avoided distortion of the signal by the long (150-foot) cable run to the readout room. The voltage attenuation of the cable used (RG-58) at 100 megahertz was ≈ 7.5 db while the voltage attenuation at 1 megahertz is ≤ 2 db.¹⁷ This difference is sufficient to obscure the leading edge of the preamplifier output signal and remove information used for pulse shape discrimination (see Appendix C) and timing (see Appendix E). This placement of the fast circuitry also avoided noise pickup over the long run. The output from the two charged particle detectors (A and C), the linear signal from the germanium detector, and pulse shape and timing information on the germanium signal were transmitted 150 feet to the counting room.

Figure 2 shows a block diagram of the counting arrangement. Standard fast/slow techniques were used for timing the germanium signal. The slow signal from the germanium detector was fed to a

single channel analyzer which selected the energy range of interest. A coincidence was formed between the germanium timing signal (see Appendix E), a good pulse shape signal (see Appendix C), the single channel analyzer and the absence of a veto signal from the charged particle detector A.

The count rate in the anti-coincidence detector A was high (instantaneous rate \approx 1 megahertz). The timing between this counter and the fast germanium signal was kept as close as possible to allow the anti-coincidence signal to be short (\approx 60 nsec). This reduced the dead time (the discriminator was dead for an interval of twice its output width for each output pulse) of the anti-coincidence circuitry permitting higher count rates while ensuring an effective charged-particle anti. That the charged-particle detector, A, showed saturation effects at lower count rates than the germanium detector may be seen from Figure 4 which gives normalized germanium counts versus beam rate. The slight (10 per cent over the region of interest) rise in this curve for increasing beam rate is indicative of loss of anti-coincidence signals.

The discrimination level on counter C was set high enough so that it saw only scattered protons. For the 600 MeV beam, signals from this detector were scaled and used as a secondary beam monitor. For the 300 MeV beam, the count rate on this detector during beam bursts was too high to scale and it was used solely to signify the arrival of the proton burst. The first pulse from this counter opened a gate which lasted for the duration of the beam pulse (a

minimum of 60 μ sec).

Two pulse height analyzers were used during the course of the experiment; a 1024 channel Nuclear Data ND-101 and a 1600 channel Victoreen Scipp (one or the other was used for each run). The analyzer was gated to convert those signals which met the coincidence requirements. For the 300 MeV beam, the event was routed to either the upper or lower half of the memory depending on the state of the gate initiated by counter C. For each 300 MeV run we thus obtained γ -ray energy spectra (typical range of .5 to 10 MeV) for both beam on and beam off. The beam off spectra were taken to detect delayed γ rays and to give information on the ambient background. For the 600 MeV beam, this division into beam off/beam on was impossible since the beam was extracted by scattering from an internal target and had essentially a 100 per cent duty factor. Typical count rates at the pulse-height analyzer were 20 to 200 counts/min.

B. Proton Beam Flux

The proton beam passed through an argon ionization chamber one meter down stream from the target. The output of this chamber was monitored on an Elcor (model A310B) current meter. The integrated current from this unit gave the total proton flux for each run. The ion chamber was calibrated at least once during each target run by comparison with a ^{12}C irradiation. For these calibrations a polystyrene target was irradiated by the proton beam under running conditions for 10 minutes. The polystyrene was then

removed to a counting station and the annihilation radiation from induced ^{11}C was monitored for several half-lives. The counting station consisted of a 2-inch NaI crystal feeding a 400 channel pulse height analyzer. The intensity of the ^{11}C annihilation radiation was determined by comparison with a ^{22}Na source of known strength. The proton flux could then be determined from the known¹⁸ $^{12}\text{C}(\text{p},\text{n})^{11}\text{C}$ total cross sections at 300 and 600 MeV. The results of several of these runs are shown in Table 1. These calibrations were consistent to within 15 per cent and agreed with an independent calibration of the ion chamber.¹⁹ The final column of Table 1 gives the number of protons per current integrator step (3×10^{-9} coulombs) and these figures were used in all cross section calculations.

A probable source of error in the cross section measurements was pulse pile-up due to the duty factor (≤ 1 per cent) of the 300 MeV proton beam. This effect was checked by monitoring the total number of events in the γ -ray spectra versus beam current. The results of these tests for two targets (carbon and calcium) are shown in Figure 4. It can be seen that in the region at which the data were taken ($.5$ to 1×10^{-9} - coulombs on Figure 4) the effects of pile-up are less than 14 per cent. No correction was made for this effect, but it is included in the overall error specification (see section IV).

C. Detector Efficiency and Energy Calibration

The efficiency of the Ge(Li) detector system (including pulse shape discrimination) was determined with calibrated sources.²⁰ The sources used are listed in Table 2. Figure 5 shows the total efficiency of the detector for the geometry used in the experiment. No correction was made for the finite beam size at the target (≈ 1 square inch) as it was assumed that the γ rays originated from a point source.

The energy calibration was based on radioactive sources below 4.44 MeV γ -ray energy and extended to higher energies with a precision mercury pulser. A series of pulser peaks corresponding in energies to .5 to 10 MeV were least squares fitted to gaussian line shapes to determine center channels. These centers were then fitted to a system response function of the form

$$E = Ax + Bx^2 + \frac{C}{x} + D$$

where: E is the pulser amplitude and x is the channel number. Typical ratios of B/A were $\approx 10^{-5}$ MeV/channel² and the value of C was $\approx 2 \times 10^{-2}$ MeV channel. After the shape of the response function was determined by the pulser data, the curve was normalized by the best fit to the radioactive source lines.

D. Neutron Contamination

Several possible sources of γ rays other than those from prompt proton-induced reactions are possible in an experiment of

this type. These include neutron-induced nuclear excitations and neutron and proton induced beta active nuclei which subsequently decay to excited levels of interest. Residual room background was also present. There are two types of neutron sources expected:

1. neutrons generated upstream of the target which follow the general line of the proton beam, and
2. neutrons generated in the target by various X (p,xn) Y reactions.

The neutrons generated upstream (1 above) are assumed to originate from (p,xn) reactions in components of the proton transport system. Since this system has a clear aperture of six inches, the neutron "beam" is of at least this diameter. This should be compared with typical proton beams of less than 1-inch by 1-inch and target containers of 3-inch diameter. γ rays produced by these neutrons were thus reduced (by at least a factor of 4) by making the targets as small as practical. The effects of the second source were investigated by placing lead between the target and γ -ray detector to ensure that all γ rays of interest were suitably attenuated.

One interesting line can be attributed to neutron interaction in the detector exciting the first excited 0^+ state of ^{72}Ge . This line (at .692 MeV) persists in the spectra of all targets and also was not attenuated when lead was inserted between the target and detector. Chasman, et al.²¹ have studied the interactions of neutrons (1.2 to 16.3 MeV) on germanium. They obtain a cross section of ≈ 80 mb for the excitation of this line by 1.2 MeV

neutrons. Several statements are possible from the shape and intensity of this line. This state decays by internal conversion and thus is detected with 100 per cent efficiency. When the energy of the incident neutron goes above the threshold for production of this 0^+ state, the energy observed in the detector is greater than the excitation energy (.692 MeV) of the line. This is due to summing in the detector of the energy of the conversion electron with the recoil energy of the germanium atom. Chasman, et al.²² have measured the broadening of this line and compared the results to predictions of Lindhard, et al.²³ on nuclear and electronic stopping. The magnitude of this broadening was found to be about 100 keV for 2.2 MeV neutrons. Thus, the width and area of the .692 MeV line can be used to give estimates of the energy and number of neutrons present at the detector location. None of the spectra showed any broadening of the .692 MeV line and it is therefore assumed that the majority of the neutrons were of energy ≤ 1.5 MeV. In two of the targets (O and B) a second line was in close proximity to the ^{72}Ge line. In both cases, however, this line disappeared on insertion of lead between the detector and target and was thus attributed to a prompt γ ray from the target. Table 3 gives the results of the investigation of the number of neutrons at the detector location.

E. Targets

The targets used in this experiment were of natural isotopic abundances. Table 4 gives the details of each target. The liquid

and powdered targets were enclosed in thin wall (.005-inch) brass cylinders 3 inches in diameter. The liquid nitrogen was contained in a similar thin (.005-inch) brass target chamber which was attached to a 2 liter reservoir. This whole assembly was insulated with 1-inch of styrofoam on all sides. This construction maintained the liquid nitrogen target for periods of up to 12 hours. Runs were made with empty target containers to insure that they made no contribution to the γ -ray spectra.

III. DATA ANALYSIS

The energies, widths, and cross sections of the transitions studied were all determined by standard non-linear least squares fitting procedures. These fits were performed on The College of William and Mary 360/50 computer. In general, the function used was a sum of gaussians with an exponential background. The region of fitting thus included the peak of interest and as large an interval of background as practical. This was to allow as accurate a determination as possible of the background. To insure that background subtraction did not introduce large errors into the analysis, several lines were fitted with several different ranges of background channels included in the fit. The results showed only slight variation of the final parameters with various channel cut-offs and the errors overlapped in all cases. The errors shown are the statistical errors obtained from the covariance matrix used in the fitting procedure. From these results it can be seen that the exponential background is very adequate over the energy intervals required. The peak areas were then determined from the parameters of the gaussian curves.

In all the spectra (Figures 6 to 13) the solid curves indicate the fitting region and the best fit obtained.

If the line of interest was well resolved, the three gaussian

parameters (center, width, and amplitude) were allowed to vary to obtain the best fit. For some lines which were not prominent or in order to obtain limits on unobserved cross sections, one or two of the gaussian parameters were held constant. In almost all of these cases only the width was held constant. An estimate of the width based on the lifetime and spin of the level, the reaction process, and the system resolution was used in these cases. In the tables giving the results of analysis, any line in which parameters were held constant is indicated by the absence of error specifications on the appropriate parameter.

For a few cases in which the presence of two lines complicated the fitting, a stripping procedure was used. These instances involved the 4.44 MeV, 2^+ level of ^{12}C . The procedure was to obtain a standard lineshape using the 4.44 MeV ^{12}C γ ray from a PuBe source. This line was then smoothed and broadened to the width of the experimental line. The lineshape (including Compton spectrum) was then subtracted from the data. This procedure allowed extraction of information from the energy region of the Compton edge of the ^{12}C 4.44 MeV line. Instances of use of this procedure are indicated in the discussions of experimental results (section V).

IV. EXPERIMENTAL ERRORS

All uncertainties listed in Tables 7 to 14 are one statistical standard deviation errors obtained from the fitting procedure and are the diagonal elements of an error matrix. These are quoted to allow comparisons of lines within the same run. These must be combined with nonstatistical and/or systematic errors to obtain absolute errors. The sources of these errors are enumerated in the following paragraphs and are tabulated in Tables 5 and 6.

Errors in the calculated energies could arise from two sources:

1. error in the calibration lines used, and
2. errors at energies outside the range of the calibration sources introduced by the procedure of pulser extension of the ADC linearity curve.

The energies of all calibration lines were known to less than one keV (see Table 2) and should, therefore, not contribute substantially to the uncertainties. The second source of calibration errors could be considerable in the energy intervals from 2.5 to 3.5 MeV and above 3.5 MeV. Table 5A and 5B give the error from various sources at several energies. These were obtained from the fitting procedure used in constructing the ADC linearity curve.

Several sources of error exist for the cross section

measurements. The error due to pile-up losses (see section IIA) in the detector is estimated from Figure 4. The detector efficiency curve (Figure 5) is used to estimate inaccuracies due to source calibrations. Above 4.4 MeV, the detector efficiency was obtained by comparison with Monte Carlo calculations²⁴ for a similar detector; this technique results in a large uncertainty at high energies. Calibration of the ion chambers depends on the total cross section for $^{12}\text{C}(\text{p,pn})^{11}\text{C}$ as given by Cummings¹⁸ and on the accuracy of the ^{11}C activity determination. Table 1 was used to estimate an error from variations in the ion chamber used to monitor the beam current. These errors are tabulated for several energies in Table 6A and 6B.

A possible source of error in the calibration of the ion chambers is due to multiple coulomb scattering in the target since the target was not in place during the irradiation runs. Based on the article by Sternheimer,²⁵ the maximum variation in ion current in the monitor chamber for target in versus target out is < 1 per cent. These figures were based on the target parameters (see Table 4), a target to detector distance of 30cm, and a sensitive radius for the ion chamber of 7.5cm.

Below 1 MeV, absorption of γ rays in the target required corrections of up to 15 per cent. Lines below 1.2 MeV were corrected for this absorption assuming all γ rays to originate at the center of the target. This effect was ignored for lines above 1.2 MeV. Since some of the targets used were not homogeneous, variation in

thickness should also be considered. Table 4 gives errors due to variations in target thickness along the proton beamline.

V. EXPERIMENTAL RESULTS

The experimental data were presented in Tables 7 to 14. Also listed in these tables are the characteristics of the various levels and transitions. This information was taken from the compilations of references 25, 27, and 28. The cross sections quoted are 4π times the differential cross section for observing the γ ray at 90° to the incident beam.

A. Boron Target

Table 7 presents the results of the analysis of the boron data along with some characteristics of the various levels. Three lines were identified as inelastic excitation of the three lowest levels in ^{11}B . These three levels decay to the ground state by M1 emission of a γ ray. The lifetime of each of these states is less than 10^{-14} sec and they show the expected Doppler broadening.

Several levels in ^{10}B were identified. Due to the high (20 per cent) isotopic abundance of ^{10}B in natural boron, it is impossible from the present results to determine if these levels are excited by inelastic scattering from ^{10}B or from neutron knockout in ^{11}B . The figures given in Table 7 assume that the total cross section lies in the knockout reaction. The lifetime of the 1.739 MeV level is short enough (1.4×10^{-13} sec) so that its decay γ ray should show Doppler broadening; however, close analysis of this line

showed a definite contribution with no broadening. This was resolved by fitting the lineshape for the γ ray with the sum of two gaussians. The centers of both gaussians were held fixed at the accepted energy (1.092 MeV) of this line²⁶ and the width of one was held at the instrumental resolution (16 keV). The amplitude of both gaussians and width of the second gaussian were allowed to vary to obtain the best fit to the data. This gave the division shown in Table 7 where the cross section labeled "direct" is the broadened line and that labeled "cascade" is the unbroadened one. The narrow contribution can in this way be attributed to a cascade from the long lived (1.4×10^{-11} sec) state²⁶ at 2.152 MeV. The various decay modes of this level observed in this experiment are not inconsistent with the published²⁶ branching ratios.

The line at .717 MeV is very close to the level in Germanium (.692 MeV) which is excited by inelastic neutron scattering (see section IID). These two lines were resolved by holding the width and position of the ⁷²Ge line constant and fitting the total lineshape to a sum of two gaussians. The shape and position of the ⁷²Ge line were obtained from spectra taken under conditions identical to the boron run except that 2 inches of lead between the detector and target attenuated the boron γ ray. Since the ⁷²Ge line is generated by neutrons in the detector itself, it was not attenuated.

Thus, the five γ rays observed originating from ¹⁰B can be attributed to the excitation of three levels. The resulting cross sections for the excitation of these three levels are:

$$2.152 \text{ MeV}; \sigma = 3.42 \pm .85 \text{ mbarns}$$

$$1.739 \text{ MeV}; \sigma = 2.13 \pm 2. \text{ mbarns}$$

$$.717 \text{ MeV}; \sigma = 1.68 \pm 2.3 \text{ mbarns}$$

The branching ratios of reference 26 were used to calculate the level cross sections. The cross section from observation of the individual lines was taken as 4π times the differential cross section at 90° .

Only one line was seen which could be attributed to ^{10}Be . This was the decay of the 3.368 MeV state to the ground state. No evidence was obtained for other than direct excitation of this level.

B. Carbon Target

Figures 7 and 8 show the spectra obtained for carbon at 300 and 600 MeV, respectively. The only inelastic line seen was the 2^+ first excited state at 4.44 MeV. This level is short lived and shows Doppler broadening (see section VIC). The single particle knockout reactions to ^{11}B and ^{11}C could only be observed for the 600 MeV run. The first excited states of these two nuclei, both of which are near an excitation energy of 2 MeV, have been identified. As indicated by Figure 4, 2 MeV corresponds to the energy of minimum efficiency for our detector. The lack of observation of these lines in the 300 MeV data is therefore reasonable since the statistics on this run were much poorer. Tables 8 and 9 show the energies, widths, and cross sections of the lines identified.

C. Nitrogen Target

Only one transition was seen using the ^{14}N target. This was the excitation of the $^{12}\text{C}, 2^+$ level at 4.44 MeV. Limits were obtained for several inelastic levels in ^{14}N by fitting the spectra with the energies and widths of the expected lines constant. The results are shown in Table 10.

The 2.311 MeV, 0^+ level in ^{14}N could be excited directly or by cascade from the 5.104 or 3.945 levels. Since the lifetime of the 5.104 level is long, we would expect no Doppler broadening of the 2.311 level when a cascade from the 5.104 level occurs. Detailed analysis of the lineshape of the transition could not rule out excitation of the 5.104 MeV level. (The procedure used to separate these transitions was discussed in reference to the ^{10}B line at 1.092 MeV.) The best limit we were able to establish ($< .43$ mbarns) for this transition was a factor of 6 greater than the limit ($< .07$ mbarns) for the 5.104 MeV to ground state transition. The cross section of 1.4 ± 1 mbarns for the 5.104 MeV to 2.312 MeV transition is inconsistent with the ground state transition of the 5.104 MeV level and the error quoted (one statistical standard deviation) is probably too small.

The ^{12}C 4.44 MeV line was subtracted to allow more accurate determination of the limits for the 5.104 and 4.910 lines in ^{14}N . The "standard" was the ^{12}C line from a PuBe source broadened to the width of the experimental data.

D. Oxygen Target

Figures 9 and 10 show the spectra obtained for a water target at 300 and 600 MeV, respectively. Tables 11 and 12 show the cross sections, widths, and energies obtained from the fitting procedure. The only inelastic line identified in ^{16}O was the 3^- level at 6.13 MeV. Since this level has a lifetime of $> 10^{-12}$ sec, there is no Doppler Broadening.

Four lines were attributed to single particle knockout leading to excited states of ^{15}O and ^{15}N . The $3/2^-$ levels at 6 MeV showed Doppler broadening implying lifetimes for these states of $< 10^{-12}$ sec. While the $5/2^+$ levels at 5 MeV showed no broadening. This is in agreement with the accepted lifetimes of these states.²⁷ That we did not identify the $1/2^+$ levels at 5 MeV is not surprising since these levels have lifetimes of $< .5 \times 10^{-13}$ sec²⁷ and should be Doppler broadened. In this case a cross section for the $1/2^+$ levels of the same order as that for the $5/2^+$ levels would have been unobservable above the background.

Other lines of interest from the oxygen target are attributed to multiparticle (or cluster) knockout reactions to states in ^{12}C , ^{14}N , and ^{10}B . In this target (in contrast to the nitrogen target), the decays of levels excited in ^{14}N were consistent with the published²⁶ branching ratios--in particular with retard to decay of the 5.104 MeV level. We did not observe the 2.792 MeV line corresponding to the 5.104 MeV to 2.312 MeV transition. The limits obtained for the 2.792 MeV transition ($< .09$ mbarns and $< .13$ mbarns

at 300 and 600 MeV, respectively) were, however, consistent with cross sections of $.06 \pm .03$ and $.17 \pm .06$ mbarns which we would expect based on the cross section obtained for the 5.104 MeV to ground state transition and a 2 to 1 branching ratio for the crossover to cascade transitions. There is also good evidence for direct excitation of the 2.312 MeV level since the transition 3.945 to 2.312 MeV was not observed.

E. Magnesium Target

The very large number of possible states excited using magnesium of natural isotopic abundance (arising from the three isotopes-- ^{24}Mg , ^{25}Mg , ^{26}Mg) and density of states in neighboring nuclei makes the analysis subject to large errors. The high background and its irregularity may indicate the presence of many unresolved states. Several lines were also established for which an unambiguous assignment could not be made.

Figure 11 shows the spectrum for the magnesium target and Table 13 shows the cross sections, energies, and widths for those lines which could be identified.

In ^{25}Mg , the only level definitely identified was the $1/2^+$ state at .584 MeV. We obtain a relatively large (20 mbarns) cross section for excitation of this state. This cross section was calculated assuming the line came solely from inelastic scattering in the minority isotope ^{25}Mg . The level could also be excited by neutron knockout from ^{26}Mg . Excitations of a few millibarns for the levels at 1.96 and 1.61 MeV cannot be ruled out by the present

experiment in view of the close proximity of all the transitions involved to other established levels. (The lines due to the 1.369 MeV level in ^{24}Mg , the 2.078 and 2.641 MeV levels in ^{23}Na , and the 2.770 and 2.042 MeV levels in ^{23}Mg .) There is some evidence for the $1.96 \rightarrow .585$ transition; however, this lies on the Compton edge for the ^{23}Na , ^{23}Mg lines at 2.078, and 2.042 MeV, respectively, and a determination of the amplitude would require a much more detailed knowledge of the shape of the Compton spectrum than we have at this energy.

In the single particle knockout reactions to ^{23}Na and ^{23}Mg , six lines have been identified. The experimental low energy cut-off prohibited observation of two lines in ^{23}Na the analogues of which were identified in ^{23}Mg . The decays of the ^{23}Na 2.08 and ^{23}Mg 2.04 MeV, $7/2^+$ levels to the first excited states showed no Doppler broadening confirming a lower limit on the lifetimes of 5×10^{-14} seconds.²⁸ The $1/2^+$ state at 2.64 MeV in ^{23}Na and its supposed analogue at 2.77 MeV in ^{23}Mg both showed Doppler broadening implying lifetimes for these transitions of $< 10^{-12}$ seconds. Only the isotopic abundance of ^{24}Mg was taken into account in the quoted cross sections for the ^{23}Mg and ^{23}Na levels. The possibility of exciting these levels from the minority isotopes (^{25}Mg , ^{26}Mg) was not considered.

Table 14 gives the cross section for excitation of the various levels in ^{23}Mg and ^{24}Na based on the observed γ -ray cross section and published²⁸ branching ratios.

In order to confirm the ^{16}O , 3^- level at 6.13 MeV,

comparisons were made with ^{16}O data of the same run at 6 MeV γ -ray energy. By comparing amplitudes of the 6.13 MeV line and obtaining limits on the excitation of the ^{15}O and ^{15}N levels (which were observed with the oxygen target), the oxygen contamination of the magnesium target could be obtained. This analysis showed that less than 7 per cent of the observed cross section could be attributed to direct excitation of oxygen contaminants.

F. Calcium Target

Figure 12 shows the spectrum obtained with a natural calcium target. Here, as in magnesium, the large number of final states possible and the shape and magnitude of the background indicate the possibility of many unresolved lines. Table 15 gives the cross sections, energies, and widths of the lines identified. Five lines which were observed could not be unambiguously identified. In Table 15, cross sections are given for the unidentified lines. Values are quoted for both possible energy assignments (observation by photo effect or double escape). Assignment of some of these lines as photo peaks of ≈ 2 MeV would correspond to lines quoted by other authors (see section VII); the large cross sections (relative to other definite assignments in this target) so obtained make these assignments unlikely.

Only one line was identified as produced by inelastic scattering in ^{40}Ca ; this was the long-lived 3^- level at 3.74 MeV. The low-energy experimental cut-off prohibited observation of γ rays

from the 4.48 \rightarrow 3.74 transition.

Eight lines were identified as resulting from single particle knockout to excited states of ^{39}Ca and ^{39}K . The energies of the levels at 6.13 and 6.35 MeV are in slight disagreement with quoted values.²⁸

VI. THEORETICAL CONSIDERATIONS

A. Inelastic Scattering

The shape of the Doppler broadened γ -ray spectrum is dependent upon the angle of emission of the γ ray with respect to the recoiling nucleus and upon the velocity of the recoiling nucleus. For convenience of later calculations, these effects may be divided into the usually measured quantities; namely, the differential cross section for the inelastic scattering, and the angular correlation of the de-excitation γ ray with respect to the recoiling nucleus.

The angular distribution $\omega_L(\theta)$ of de-excitation γ rays with respect to some arbitrary Z axis is given by several authors^{30,31,32} as

$$W_L(\theta) \propto \sum_{m_i, m_f} P_{m_i} G(m_i, m_f) F_L^M(\theta) \quad (1)$$

where:

m_i, m_f are the Z components of the magnetic sublevels of the initial and final nuclear states,

L, M are the angular momentum quantum numbers of the γ ray with $M + m_f = m_i$,

P_{m_i} is the relative population of the m_i^{th} magnetic sublevel of the initial state,

$G(m_i, m_f)$ is the relative probability of γ decay from the m_i^{th} sublevel of the initial state to the m_f^{th} sublevel of the final state, and

$F_L^M(\theta)$ is the angular distribution function for a photon of angular momentum described by L, M .

We will be interested in studying the γ decay of nuclear levels to a ground state of zero angular momentum. Frauenfelder and Steffen³¹ show that the $G(m_i, m_f)$ is given by the square of the Clebsch-Gordan coefficient $\langle I_f, m_f, LM | I_i, m_i \rangle$ for expressing the initial state as products of the final nuclear (I_f, m_f) and electromagnetic (L, M) states. For the case of $I_f, m_f = 0$, angular momentum conservation allows only one such term with $L = I_i$, $M = m_i$ and the coefficients $G(m_i, 0) = 1$.

The angular distribution $F(\theta)$ is calculated³² by considering the energy flow or Poynting vector on a large sphere of radius r such that $kr \gg 1$ and both the electric and magnetic waves are transverse. In this case

$$F_L^M(\theta) \propto \mathbf{E}^* \cdot \mathbf{E} \approx \mathbf{H}^* \cdot \mathbf{H} \propto [Y_M^{L(L,1)}(\theta, \phi)]^\dagger [Y_M^{L(L,1)}(\theta, \phi)] \quad (2)$$

where:

\mathbf{E} & \mathbf{H} are the electric and magnetic fields

$Y_M^{L(L,1)}(\theta, \phi)$ are the vector spherical harmonics, and

$$Y_M^{L(L,1)} = \sum_{\mu} \langle j\lambda 1\mu | LM \rangle y_{j\lambda}(\theta, \phi) \chi_{\mu}$$

where $y_{j\lambda}(\theta, \phi)$ are the spherical harmonics, and

χ_μ is the vector describing the spin 1 photon.

$$F_L^M(\theta) = \sum_{\mu\lambda} \langle j\lambda 1\mu | LM \rangle \langle j\lambda' 1\mu' | LM \rangle y_{j\lambda}^*(\theta\phi) y_{j\lambda}(\theta\phi) (\chi_\mu^\dagger \chi_{\mu'})$$

since

$$(\chi_\mu^\dagger \chi_{\mu'}) = \delta_{\mu\mu'}$$

$$F_L^M(\theta) = \sum_{\mu\lambda} \langle j\lambda 1\mu | LM \rangle^2 |y_{j\lambda}(\theta\phi)|^2$$

where: $M = \mu + \lambda$.

Evaluating the Clebsh-Gordan coefficients explicitly gives:

$$F_L^M(\theta) = \frac{(L+M)(L-M+1)}{2L(L+1)} |y_{L, M-1}(\theta\phi)|^2 + \frac{M^2}{2L(L+1)} |y_{LM}(\theta\phi)|^2 + \frac{(L-M)(L+M+1)}{2L(L+1)} |y_{L, M+1}(\theta\phi)|^2 \quad (3)$$

The distribution of equation (2) assumes a pure multipole. If we had not restricted ourselves to decays to the ground state of spin zero nuclei, competing multipolarities would be possible and equation (3) would involve interference terms from products such as:

$[Y_M^{L(L,1)}]^\dagger Y_{M'}^{L'(L',1)}$ with the restriction of $m_f = 0$, equation (1)

becomes

$$W_L(\theta) = \sum_{m_i} P_i \cdot F_L^M(\theta) \quad (1')$$

and the angular distribution of the de-excitation γ rays is simply determined by the population ratios for the various magnetic sub-levels of the excited state. A simple case frequently given^{11,14} as a first approximation assumes only the $m_i = 0$ substate is populated. This can be seen most simply by choosing the z axis to lie along the recoil direction. In this case, the orbital contribution $\vec{L} = \vec{R} \times \vec{P}$ can have no z projection. Since we are studying states

excited by proton bombardment of a spin zero nucleus, the initial state has $J = 0$ and any z projection of the angular momentum must come from the projectile spin. Assuming the projectile spin is unchanged by the interaction leaves only the $m = 0$ substate populated. For $I_j = 2$ and $m_j = 0$ only, $1'$ can be written (the subscript j here is the final nuclear state for the inelastic scattering which is the initial state for the γ decay)

$$\begin{aligned} W_L(\theta) &= P_0 F_2(\theta) \propto \sin^2\theta \cos^2\theta \\ &= \frac{1}{4} (1 - \cos^2 2\theta) = \frac{1}{4} \sin^2 2\theta. \end{aligned} \quad (4)$$

This form for the γ -ray angular distribution was used in the calculation for figure 15.

The following description of the inelastic scattering process is due to Banerjee and Levinson^{12,13} and ignores exchange and antisymmetrization effects. Let us represent the target nucleus as a core surrounded by n extra-core particles whose degrees-of-freedom are given by S_1 for the first extra-core particle, S_2 for the second, et cetera. The coordinates of the projectile will be represented by S_p . In this case, the total Hamiltonian can be written as

$$H = V_p + T_p + \sum_{i=1}^n (T_i + V_i + \sum_{j \neq i} V_{ij} + V_{pi}) \quad (5)$$

where:

V_n is the interaction potential of the n^{th} particle with the core,

T_n is the kinetic energy of the n^{th} particle, and

V_{nm} is the interaction of the n^{th} with the m^{th} particle.

Within this framework, the Hamiltonian of the target nucleus, H_t , is given by

$$H_t = \sum_{i=1}^n (T_i + V_i + \sum_{j \neq i} V_{ij}) \quad (6)$$

The Schroedinger equation for the target is given by

$$H_t \psi_m(s_1, s_2 \dots s_n) = \epsilon_m \psi_m(s_1, s_2 \dots s_n) \quad (7)$$

where:

$\psi_m(s_1, s_2 \dots s_n)$ are the wave functions of the target nucleus, and

ϵ_m is the energy of the m^{th} excited nuclear state.

The Schroedinger equation for the total scattering process is

$$H\Psi(s_1, s_2 \dots s_n, s_p) = E\Psi(s_1, s_2 \dots s_n, s_p) \quad (8)$$

where:

$\Psi(s_1, s_2 \dots s_n, s_p)$ is the total wave function of the target and projectile, and

E is the total system energy.

Since the ψ_m 's form a complete set, we may expand Ψ in terms of them, viz.

$$\Psi(s_1, s_2 \dots s_n, s_p) = \sum_m \psi_m(s_1, s_2 \dots s_n) Q_m(s_p) \quad (9)$$

Using equations 5, 6, and 9, the Schroedinger equation for the total system (8) becomes

$$(H_t + V_p + T_p + \sum_{i=1}^n V_{pi}) \sum_m \psi_m Q_m = E\Psi \quad (10)$$

Multiplication of (10) on the left by ψ_f^* and integration over all coordinates of the extra-core particles gives

$$\left(V_p + T_p - \frac{k_f^2}{2m}\right) Q_f = \int \psi_f^* \sum_{i=1}^n V_{pi} \Psi \, ds_1 ds_2 \dots ds_n \quad (11)$$

where $\frac{k_f^2}{2m} = E = \epsilon_n$ is the kinetic energy of the scattered particle.

If we restrict the expansion of Ψ on the right-hand side of equation (11) to the sum of two terms (the initial and final states) thus ignoring virtual transitions to all other states of the target, we write Ψ as

$$\Psi = \psi_i Q_i + \psi_f Q_f.$$

The integral, $\int \psi_f^* \sum_{i=1}^n V_{pi} \psi_f Q_f \, ds_1 ds_2 \dots ds_n$, representing the

interaction of the projectile with the final nuclear state may be interpreted as an effective elastic potential between the projectile and the excited final state. It may then be brought to the left-hand side of equation (11) and combined with V_p to form an average interaction potential of the projectile with the nucleus \bar{V}_p .

Equation (11) may now be written

$$\left(\bar{V}_p + T_p - \frac{k_f^2}{2m}\right) Q_f = \int \psi_f^* \sum_{i=1}^n V_{pi} \psi_i Q_i \, ds_1 ds_2 \dots ds_n \quad (12)$$

The solution of (12) by Green's functions is given by Tabacman¹⁵ and yields for the inelastic scattering amplitude

$$F(\theta) = \frac{k_f \mu}{k_i} \frac{1}{2\pi} \int \phi_f^*(s_p, -k_f) \psi_f^* \sum_{i=1}^n V_{pi} \psi_i \phi_i(s_p, k_i) \times ds_1 ds_2 \dots ds_n ds_p \quad (13)$$

where:

k_i and k_f are the initial and final projectile momenta,

ϕ_n are the solutions of the homogeneous form of (11)

and may be identified as the wave functions of the projectile, and

μ is the reduced mass of the projectile in the projectile-nucleus system.

If we now write the projectile wave function as a product of a spatial and a spin part,

$$\phi_j = F_j(k_j, r_p) \chi(\sigma_p \tau_p)$$

where:

F_j contains all the spatial degrees of freedom, and

χ reflects the spin and isospin functions; equation (13)

may be written

$$\int \psi_f^* \chi_f^\dagger \int F_f^* \sum_{i=1}^n V_{pi} F_i ds_p \psi_i \chi_i ds_1 ds_2 \dots ds_n. \quad (14)$$

If we assume that the nuclear wave functions are antisymmetric for exchange of any two particles, then since the integral over ds_p is a function of r_i only, each term in the sum makes an identical contribution and the summation over i may be represented by N , the number of extra-core particles. To further simplify the derivation, we approximate V_{pi} by a delta function in the spatial coordinate, viz.

$$V_{pi} = V_o \delta(r_p - r_m)$$

where:

V_o is the scalar magnitude of the delta function, and

r_m is the radius to the struck particle.

This gives for (14),

$$NV_o \int \psi_f^* \chi_f^\dagger F_f^*(r_m, -k_f) F_i(r_m, k_i) \psi_i \chi_i ds_1 ds_2 \dots ds_n \quad (15)$$

where:

N is the number of extra-core particles and, as mentioned previously, reflects the summation over i , and

r_m is the radius of the m th extra-core particle and comes from the delta function and integration over the projectile coordinates. If we now write the spatial portion of the projectile wave functions as plane waves, equation (15) becomes

$$NV_o \int \psi_f^* \chi_f^\dagger e^{i\vec{q} \cdot \vec{r}_m} \psi_i \chi_i ds_1 ds_2 \dots ds_n \quad (16)$$

where $\vec{q} = \vec{k}_i - \vec{k}_f$ is the momentum transfer.

If we now choose the z axis to lie along q , we may expand the exponential as

$$e^{i\vec{q} \cdot \vec{r}_m} = \sum_{\ell=0}^{\infty} j_{\ell}(q r_m) Y_{\ell}^0(\theta)$$

where j_{ℓ} is the spherical Bessel function of order ℓ and

$$\frac{d\sigma}{d\Omega} = |f(\theta)|^2$$

$$= \frac{k_f}{k_i} \left(\frac{\mu}{2\pi} \right)^2 N^2 V_o^2 \left| \int \psi_f'^* \chi_f^\dagger Y_{j_f}^{m_f*} \sum_{\ell=0}^{\infty} (j_\ell(qr_m) Y_\ell^0(\theta)) \right. \\ \left. \times Y_{j_i}^{m_i} \chi_i \psi_i' ds_1 ds_2 \dots ds_n \right|^2$$

where: ψ' contain the radial dependence of the nuclear states and the angular portions of the nuclear states have been written as spherical harmonics. Due to the orthonormality of the spherical harmonics, the only term surviving will be for $j_i + \ell = j_f$. Thus, if we ignore the spin of the projectile, the cross section can be written as

$$\frac{d\sigma}{d\Omega} \propto \frac{k_f}{k_i} \left(\frac{\mu}{2\pi} \right)^2 N^2 V_o^2 |j_\ell(qr_m)|^2 |G(r_m)|^2 \quad (17)$$

where $G = \int \psi_f'^* j_\ell(qr_\ell) \psi_i' dr_1 dr_2 \dots dr_n$, is a form factor dependent on the radial wave function $\psi'(r_1, r_2 \dots r_n)$. Thus, in the simplest case of plane waves for the projectiles and a delta function interaction, the differential cross section for scattering from a spin zero nucleus is given by the square of the spherical Bessel function of order ℓ , where ℓ is the spin of the excited state. Also in this simple case, since V contains no operator in the spin space of the projectile, the z component of the angular momentum cannot change and for an initial state with $J = 0$, only the $m = 0$ substate of the final state can be excited.

The theory of direct interactions has been elaborated by

several authors.^{12,14,15,33} Banerjee¹² and Satchler¹⁴ have extended the approach by using distorted waves for the projectiles. Recently, Bassel and Wilkin³³ have calculated the differential cross section for inelastic scattering to the first 2^+ state of ^{12}C using Glauber theory.

All of the calculations detailed in section VIB assume that the $\pm m$ states for a given m are equally populated. This is possible in the plane wave case with an unpolarized incident beam since the classical recoil direction is well defined by the momentum transfer and gives an axis of symmetry about which the $\pm m$ components will be equal. As Banerjee and Levinson¹³ point out, when distorted waves are used a symmetry axis still exists but it is not necessarily the recoil direction.

A more realistic nucleon-nucleon potential would include terms coupling the spin of the projectile and nucleus. This would allow spin flip of the projectile and population of the $m = \pm 1$ substates of the final state.

Figure 14 shows the differential cross sections used in section VIB. Shown are the square of the second order Bessel function, $|j_2(qr_0)|^2$ where $r_0 = 2.96 \text{ F}$; the differential cross section calculated by Bassel and Wilkin³³; and a smooth line representation of the data obtained at 185 MeV proton energy by Clegg.¹ All are arbitrarily normalized and plotted versus momentum transfer, q .

B. Doppler Broadened γ -rays- Spectrum Shape for Inelastic Scattering

The energy spectrum for γ rays from inelastic proton scattering

is expected to show effects due to the recoil velocity of the excited nucleus. The detailed spectrum shape is dependent on:

1. the ratio of the slowing down time of the recoil nucleus to the lifetime of the excited state,
2. the proton differential cross section, and
3. the γ -ray angular correlation with respect to the incident proton.

In the two lines for which comparisons were possible, the lifetimes of the excited states (5.63×10^{-14} sec and $.144 \times 10^{-14}$ sec)²⁶ are much shorter than slowing down times of nuclei in matter ($\approx 5 \times 10^{-13}$ sec).³⁴ The effects of (1) above were therefore ignored.

A semi-random method was used to calculate the γ -ray energy spectrum which involved calculation of the γ -ray energy at the germanium detector for all possible proton scattering angles. This was not a true Monte Carlo calculation as the various parameters were incremented by fixed amounts rather than being chosen at random. The procedure can be represented by the following equation:

$$\frac{N\gamma_i}{\Delta E_i} = \Sigma \frac{d\sigma}{d\Omega_p} \omega(\theta\gamma, \phi\gamma) d\Omega_p J(\text{cm}^2\text{L}) \theta\gamma \phi\gamma \quad (18)$$

where: $\frac{N\gamma_i}{\Delta E_i}$ is the number of γ rays in the energy interval ΔE_i ,

θ_p, ϕ_p are the polar angles of the scattered proton with respect to the incident beam, $d\Omega_p$ is the incremental solid angle into which the proton scatters, $\frac{d\sigma}{d\Omega_p}$ is the differential cross section for proton scattering into $d\Omega_p$ at θ_p, ϕ_p , $\omega(\theta\gamma, \phi\gamma)$ is the probability of gamma

decay at angles $\theta\gamma$, $\phi\gamma$ with respect to the recoil nucleus, J (cm^2L) $\theta\gamma$, $\phi\gamma$ is the Jacobian for transformation of the γ -ray cross section from the center of mass to the lab, and the summation extends over all θ_p , ϕ_p , $\theta\gamma$, $\phi\gamma$ for which the energy of the de-excitation γ ray was in the energy interval ΔE_i .

The calculation was carried out on the William and Mary IBM 360/50 computer and proceeded as follows:

1. A proton scattering angle was selected in the P-nucleus center of mass system and the point was weighted by $\frac{d\sigma}{d\Omega_i} d\Omega_i$.
2. A transformation was made to the laboratory system where the angles $\theta\gamma$, $\phi\gamma$ compatible with experimental conditions were calculated. The point was also weighted by the probability of γ decay into $\theta\gamma_i$, $\phi\gamma_i$.
3. A transformation was made to the center of mass of the recoiling nucleus where the energy of the emitted γ ray was calculated.
4. A final transformation was made back to the laboratory to obtain the final γ -ray energy and Jacobian.
5. The previous value of the energy bin appropriate to the final γ -ray energy was incremented by the weight of this point times the final transformation Jacobian. The energy bin width (ΔE_i) was made slightly smaller than the instrumental resolution. The Jacobian was included in the weight of the point to correct for the change in solid angle subtended by the γ -ray detector introduced by the transformation in step 4 (the proton solid angle, $d\Omega_p$, was not

corrected since the proton was not observed). A reliable "spectrum" could be generated in this fashion by considering $\approx 30K$ proton interactions. This procedure treats the $(p,p'\gamma)$ interaction as two independent events in which Doppler effects are calculated to all orders (the ratio of first to second order Doppler shifts is ≈ 30 to 1). The proton differential cross section and the γ -ray angular correlation could be fed into the calculation.

The second method used to calculate the γ -ray energy spectrum followed the procedure of Kolata, et al.³⁵ which considers the Doppler energy shift to first order. This shift, ΔE , is given by

$$\Delta E = E_0 \beta \cos \alpha \quad (19)$$

where:

E_0 is the unshifted γ -ray energy,

β is the velocity of the recoiling nucleus with respect to c , and

α is the angle between the recoil direction of the nucleus and γ -ray detector.

In the coordinate system in which the Z axis lies along the incident beam direction, the number of γ rays reaching the detector is

$$d^2N_\gamma = \omega(\alpha) \sigma(\theta) \sin\theta \, d\theta \, d\phi \quad (20)$$

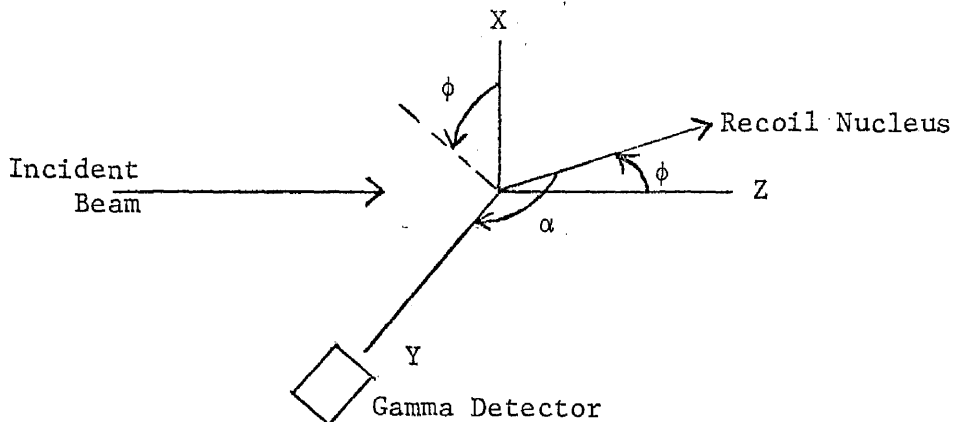
where:

$\omega(\alpha)$ is the probability for γ decay in direction α , and

$\sigma(\theta)$ is the cross section for nuclear recoil at θ ,

(assuming an unpolarized incident beam and cylindrical symmetry about the incident beam direction), and

the coordinate system is shown in the diagram below.



The energy shift of this γ ray is given by

$$\Delta E = E_0 \beta \cos \alpha = E_0 \beta \sin \theta \sin \phi. \quad (19')$$

For constant θ from (19')

$$d(\Delta E) = (E_0^2 \beta^2 \sin^2 \theta - \Delta E^2)^{1/2} d\phi \quad (21)$$

where: (21) is valid for detection at right angles to the incident proton beam direction.

The equations (21) and (20) give for the energy spectrum of the γ ray

$$\frac{d^2 N_\gamma}{d(\Delta E)} = \frac{\sigma(\theta) \sin \theta d\theta \omega'(\theta, \Delta E)}{(E_0^2 \beta^2 \sin^2 \theta - \Delta E^2)^{1/2}} \quad (22)$$

where the independent variables in the angular correlation function have been changed ($\omega(\alpha) = \omega'(\theta, \Delta E)$). Equation (22) must now be integrated over θ to obtain $\frac{dN_\gamma}{d(\Delta E)}$. This integration was performed numerically after calculating the relevant kinematical variables.

A comparison of the two computational methods is shown in Figure 15. The proton cross section used was the square of the second order Bessel function ($|j_2(qr_0)|^2$) and the γ -ray angular

distribution was calculated assuming only the $m = 0$ substate was populated. It can be seen that the two methods agree quite well with slight nonsymmetry occurring in the semi-random calculation due to higher order Doppler effects and to the solid angle transformation.

C. Comparison of Line Shapes with Experiment

The transition of the ^{12}C 4.44 MeV level to the ground state was compared with calculations of the Doppler line shape. Figure 16 shows the energy spectrum calculated using the square of a second order Bessel function for the proton differential cross section and various population ratios of the magnetic sublevels. In all cases $P_1 = P_{-1}$ and/or $P_2 = P_{-2}$. Four cases are shown in the figure:

1. population of the $m = 0$ substate only ($P_0 = 1$),
2. population of the $m = \pm 1$ substates only
($P_{\pm 1} = 1$),
3. population of the $m = \pm 2$ substates only
($P_{\pm 2} = 1$), and
4. equal population of the $m = 0$ and $m = \pm 1$ substates.

The calculations were carried out for ten values of relative population of the $m = 0$ and $m = \pm 1$ substates from $P_0 = 1, P_{\pm 1} = 0$ to $P_0 = 0, P_{\pm 1} = 1$. These showed a smooth variation between the $P_0 = 1$ and $P_{\pm 1} = 1$ limits. As can be seen by comparison with the

^{12}C spectrum of Figure 7, all distributions in which the $m = 0$ contribution dominates show too pronounced a dip at $\Delta E = 0$.

If the curves of Figure 16 are compared with the ^{12}C spectrum of Figure 7, the greatest discrepancy is seen around ΔE (the Doppler shift) = 0. The theoretical curves which are dominated by an $m = 0$ contribution (predicted by plane wave impulse approximation with no spin flip of the incident particle), go to zero at $\Delta E = 0$ whereas the data show only a slight dip. The data of Figure 7 are shown, after subtraction of an exponential background, in Figure 15 along with calculations using $|j_2(qr_0)|^2$ as a proton differential cross section. The value of r_0 used was 2.96 fermis and was chosen as the best fit to the data. It agrees reasonably well with the value of 2.3 fermis used by Blair and Sherif³⁶ in optical model fits to elastic scattering. The calculated curve for excitation of only the $m = 0$ substate shows much too pronounced a dip at $\Delta E = 0$. If spin flip of the incident proton is allowed, we may also excite the $m = \pm 1$ substates. Schmidt and Brown¹¹ find a spin flip component in excitation of the 2^+ , 4.44 MeV level of ^{12}C which varies from 20- to 40-per cent with proton scattering angle. This was measured at a proton energy of 10 MeV and may not be valid at our higher energies. Rowe, et.al.⁴ find a spin flip component which varies from 6- to 50-per cent for proton scattering angles from 15° to 45° . The work of Rowe, et.al.⁴ was done at 150 MeV proton energy and is more applicable to our situation. The curve shown in Figure 15 for $P_0 = .5$, $P_{\pm 1} = .5$ fits the data

much better. In addition to spin flip, if we allow distorted waves, it is also possible to excite the $m = \pm 2$ substates. This further reduces the $\Delta E = 0$ dip in the line shape.

In addition to the effects of the m state population ratios, the curves will be effected by the form of the proton differential cross section. Since the $\Delta E = 0$ contribution must come from forward scattering (or scattering in the plane whose perpendicular is in the direction of the γ -ray detector), our data favors cross sections which have a larger relative contribution at smaller angles. From Figure 14 we are in best agreement with the cross section obtained by Bassel and Wilkin.³³

Figure 17 shows the data from the 4.59 MeV line in B. The solid curve was calculated using a $|j_1(qr_0)|^2$ (an M1 transition) and an isotropic γ -ray distribution. Here, also, the calculated width of 145 keV agrees with our experimental value of 147 ± 27 keV. The γ -ray distribution can only be isotropic if spin flip of the incident proton is allowed (in order to populate the $m = \pm 5/2$ substates from the spin $3/2$ ground state). If spin flip of the incident particle is not allowed the distribution is given by $F_1(\theta) \propto 2 + \sin^2\theta$ which is only 33 per cent nonisotropic. This assures equal population of the $m = \pm 3/2, \pm 1/2$ substates.

VII. COMPARISONS WITH OTHER EXPERIMENTS

Tables 16 through 21 show the cross sections obtained in this experiment and the results of other authors. The experiments most similar to the present one are those by Clegg, et.al.^{1,3,6,37} and Zobel et.al.³⁸ In addition, the results of lower energy pickup reactions are shown. Where possible spectroscopic factors from these experiments are given as the ratios of these within a target should agree with our ratios.

In general, the cross sections we obtain are less than those found by Zobel and Clegg. This is to be expected at the higher energies of our experiment due to absorption of the incident beam and lower nucleon-nucleon cross section.

For two of the targets (oxygen and carbon) spectra were obtained for both 300 and 600 MeV. The large error on the absolute cross sections, however, rules out any quantitative information on energy dependence.

The previous data on boron are in general agreement with our results. In particular, the cross sections obtained by Clegg⁷ for a separated ^{10}B target and a natural boron target seem to bear out our assumption of excitation of these levels by neutron knockout rather than inelastic scattering in the minority isotope. If the ^{10}B lines originated from inelastic scattering, we would obtain a

cross section for observation of the .717 MeV line of about 28 mbarns. This is incompatible with Clegg's result of $1.8 \pm .9$ mbarns. Our nonobservance of the levels at 6.7 and 6.8 MeV is reasonable considering the efficiency of our detector at this energy.

Much experimental work has been done on carbon; the data shown in Table 17 are intended as representative. Notably absent from our results are higher excited states in ^{11}B and ^{11}C seen in the (p,d) and (p,2p) experiments at lower energies. However, cross sections of the same order as the 2 MeV levels cannot be ruled out by our results. In particular, the second excited states of these nuclei at 4 MeV could be obscured by the relatively large cross section for the ^{12}C 4.44 MeV line (for equal excitation of the 2 MeV and 4 MeV knockout lines, we would see a peak amplitude for the 4 MeV knockout reactions of about one-tenth the inelastic peak for the ^{12}C 4.44 MeV line). The intermediate coupling model for ^{11}C and ^{11}B allows excitation of these states by single particle knockout.^{39,40} The tables of Cohen and Kurath⁶² give a ratio of 2 to 1 for excitation of the $1/2^-$ level at 2 MeV to the $3/2^-$ level at 5 MeV.

For the oxygen target, the resolution of the germanium detector allowed us to separate the three levels near 4 MeV into contributions from the 3^- level in ^{16}O and the $3/2^-$ levels in ^{15}N and ^{15}O . Comparison with the pickup reactions suggest that we should have seen the $1/2^+$ levels at 5 MeV in ^{15}O and ^{15}N as well as the $5/2^+$ levels. As Warburton, et.al.²⁷ showed, however, the $1/2^+$ levels are short lived and, thus, in our case, will exhibit Doppler

broadening. A cross section of the same order as that for the $5/2^+$ level would, therefore, be lost in the background in this experiment. In the simple shell model picture, the $3/2^-$ levels at 6 MeV in ^{15}O and ^{15}N correspond to knockout of a $P3/2$ particle from the filled p shell of the ^{16}O ground state. The simple impulse approximation single-particle knockout on a simple jj coupling, filled P 1/2 shell ground state for ^{16}O cannot explain excitation of the $5/2^+$ levels. Recent experiments and calculations show,^{41,42,43} however, that the ground state of ^{16}O includes a large percentage of 2 particle--2 hole configurations. Purser, et.al.⁴³ find for the ^{16}O ground state

$$\begin{aligned} \psi_{\text{GS}}(^{16}\text{O}) = & .82 | (P3/2)^8 (P1/2)^4 \rangle + .54 | (P3/2)^8 (P1/2)^2 (d5/2)^2 \rangle \\ & + .20 | (P3/2)^8 (P1/2)^2 (S1/2)^2 \rangle \end{aligned}$$

The statistical factor for extraction of a single particle from ^{16}O is unity⁶³; and the two $d5/2$ particles will, on the average, be one proton and one neutron. If we now look at the above wave function as a sum over components of various two particle--two hole states, the cross section for exciting a specific level in the A-1 nuclei by single particle knockout is given by the square of the amplitude of each component times the number of particles in the state summed over all components which contain the state. This would predict a ratio of about 13 to 1 for excitation of the $3/2^-$ levels as opposed to the $5/2^+$ levels in ^{15}N and ^{15}O . Our results for this ratio are:

	300 MeV protons		600 MeV protons
$^{15}_N$	5 ± 2.3	(p,2p)	5.1 ± 1.7
$^{15}_O$	9.4 ± 3.4	(p,pn)	7.4 ± 2.4

In Magnesium (see Table 20), we were able to resolve several mirror levels in ^{23}Na and ^{23}Mg . The large (20 mbarns) cross section we obtain for excitation of the .584 MeV level in ^{25}Mg is not consistent with either inelastic scattering in ^{25}Mg or neutron knock-out in ^{26}Mg since we see no other lines from ^{25}Mg . In the ^{25}Mg (p,p') ^{25}Mg work by Miura, et.al.⁴⁵ This line is seen but with a lower cross section than the 1.611 MeV to ground state transition. The .584 MeV level is also observed in the ^{26}Mg ($^3He,\alpha$) ^{25}Mg work, but once again not as the most prominent line. Our cross section is certainly due to both reactions and must include some contamination. Our lack of observation of lines other than from the 1.369 MeV level in ^{24}Mg agrees with the work of Miura, et.al.,⁴⁵ who observed the 1.369 MeV level with an intensity thirteen times greater than the next most intense line.

In calcium, general agreement is obtained with other experiments (see Table 21). In particular, observation of only the 3.73 MeV level in ^{40}Ca is consistent with Clegg's work and^{1,37} the long lifetime of the state. The single-particle knockout reactions to ^{39}K and ^{39}Ca are in general agreement with the pickup results (see Table 21). The high cross section for excitation of the $7/2^-$ levels at 2.8 MeV cannot be explained by the simple shell model and, indeed, would require a very large admixture of $1F7/2$ in the ground

state of ^{40}Ca .⁴⁶ As our cross sections for these levels are higher than those obtained in the pickup reactions, we may be including some events in these lines which are due to other reactions.

Evidence was also seen in most targets for cluster or several particle knockout. Since no exit particles were detected it is not possible to say what particles were in the exit channel; however, the state of the residual nucleus is established in most cases. It is possible that the states seen were excited by multiple interactions in the target. Deuteron knockout was seen in ^{14}N to the 4.44 MeV state of ^{12}C and in ^{16}O to the 5.104 MeV state in ^{14}N . Alpha particle knockout was evidenced by the occurrence of the 2^+ , 4.44 MeV level of ^{12}C being excited from the ^{16}O target. Two alpha (or ^8Be) knockout was seen with the ^{24}Mg target in which the 3^- , 6.13 MeV level of ^{16}O was excited. There was also evidence for ^6Li knockout of ^{16}O as lines in ^{10}B were identified. In these cluster knockouts, the 2^+ , 4.44 MeV state of ^{12}C , the 3^- , 6.13 MeV state of ^{16}O , and the 1^+ , 2.152 MeV state of ^{10}B seem to be strongly excited. The unidentified lines in the calcium target may be due to cluster knockout; however, definite assignments could not be made even though elements down through ^{32}S were searched.



VIII CONCLUSIONS

The features seen by Clegg, et.al. at 150 MeV proton energy are, in general, reproduced at our energies. That is, only the lowest one or two levels are excited strongly in the target nuclei; with even-even target nuclei, the lowest two or three levels of neighboring mirror nuclei are excited by single particle knockout; there are several cases of multiparticle knockout to excited states of A-2, A-4, A-6, or A-8.

The cross sections we observed for all types of reactions were lower than those of Clegg by factors of from 2 to 3. This discrepancy can be explained as a characteristic of the higher projectile energies we used. Absorption effects should become more important at higher energies because of the increase in the number of exit channels open; in particular, the meson production channel is open at our energy. Further, the nucleon-nucleon cross section is decreasing with increasing energy in the region of interest.

The data on the Doppler broadened energy spectrum of the 2^+ , 4.44 MeV level in ^{12}C has been compared to the simple predictions of the plane wave impulse approximation. In the case of a spin-independent interaction potential, the curve obtained for the γ -ray energy spectrum has the proper width but fails to conform to the details of the experimental energy distribution. This

disagreement occurs for energy shifts of zero. Since most of the contribution to the energy spectrum at $\Delta E = 0$ comes from forward scattering (a contribution is also possible from scattering in the plane whose perpendicular points to the γ -ray detector), our data favor proton differential cross sections which have a greater relative contribution for momentum transfers near zero than does $|j_2(qr_0)|^2$; indeed, our data are in closest agreement with the differential cross section calculated using the high energy approximation of Bassel and Wilkin.³³ Secondly, m state population ratios other than the simple no spin flip, $m = 0$ approximation will change the shape of the energy spectrum. If spin flip of the incident proton is allowed, the $m = \pm 1$ substates are populated. Spin flip fractions of .5 would be required to explain our data. In addition, if distorted waves are allowed, the $m = \pm 2$ components can be excited. A 30 per cent admixture of $m = \pm 2$ would suitably explain our line shape. Nonsymmetric population of the $\pm m$ components about the classical recoil direction is also possible using distorted waves. No investigation was done of this effect.

Single particle knockout reactions to analogue states in the neighboring mirror nuclei were seen for the even-even targets. In particular, the levels in ^{15}O and ^{15}N excited with an ^{16}O target showed a difference in cross section for knockout of a proton as opposed to a neutron. Excitation of the $5/2^+$ levels in ^{15}O and ^{15}N , which requires a deformed ^{16}O ground state wave function to be explained in a particle knockout model, showed a higher cross

section for knockout of a proton (by about 30 per cent) as opposed to knockout of a neutron. This increase is in the ratio of the ratio of $5/2^+$ excitations to the excitation of the $3/2^-$ levels, so it should not be due to differences in the nucleon-nucleon cross sections. It may, therefore, be a final state interaction in which either of the two exit protons more likely excites the $5/2^+$ state than do the proton-neutron pair. If this were to be due to a Coulomb effect in the ground state of ^{16}O , then, the 2-proton part of the two particle-two hole component would have to be large. Since there are more bound states in ^{15}N than in ^{15}O , the discrepancy may occur from unobserved γ decays which preferentially populate the $5/2^+$ levels.

We also see several lines corresponding to knockout of several particles from the target nucleus. While it is experimentally impossible to determine whether these are individual particles or clusters, we see the effect when the exit particles could form a nucleus with $A = 2n$; that is, one or two alpha particles, a deuteron, or a ^6Li nuclei. We do not see states which would correspond to knockout of ^3He , T, et cetera. There are also specific states which are strongly excited. The 4.44 MeV, 2^+ state of ^{12}C is seen with both nitrogen and oxygen targets, the 6.13 MeV, 3^- state of ^{16}O is seen with the magnesium target, and the ^{10}B 2.152 MeV level was excited in the oxygen target.

While not attempted in the present investigation, the procedure developed here can be utilized with particle knockout reactions

to determine nucleon momentum distributions in the nucleus. This would be possible since, in the impulse approximation, the momentum of the residual nucleus after knockout will be equal in magnitude to the momentum of the struck particle before impact. This momentum distribution will add Doppler effects to the lineshapes of subsequent γ -ray decay lines.

REFERENCES

- ¹G. L. Salmon, K. J. Foley, and A. B. Clegg, Nucl. Phys. 41, 364 (1963).
- ²D. J. Rowe, A. B. Clegg, G. L. Salmon, and D. Newton, Proc. Phys. Soc. 81, 332 (1963).
- ³K. J. Foley, G. L. Salmon, and A. B. Clegg, Nucl. Phys. 31, 43 (1962).
- ⁴D. J. Rowe, G. L. Salmon, A. B. Clegg, and D. Newton, Nucl. Phys. 54, 193 (1964).
- ⁵D. J. Rowe, A. B. Clegg, G. L. Salmon, and P. S. Fisher, Proc. Phys. Soc. 80, 1205 (1962).
- ⁶G. L. Salmon, A. B. Clegg, K. J. Foley, P. S. Fisher, and D. J. Rowe, Proc. Phys. Soc. 79, 14 (1962).
- ⁷A. B. Clegg, K. J. Foley, G. L. Salmon, and R. E. Segel, Proc. Phys. Soc. 73, 319 (1961).
- ⁸S. T. Butler, Phys. Rev. 106, 272 (1956).
- ⁹R. M. Hayborn and H. McManus, Phys. Rev. 136, B1170 (1966).
- ¹⁰Yoshihiko Nishida, Nucl. Phys. 43, 598 (1963).
- ¹¹F. H. Schmidt, Ronald E. Brown, J. B. Gerhart, and Wojciech A. Kolasinski, Nucl. Phys. 52, 355 (1964).
- ¹²Manoj K. Banerjee and Carl A. Levinson, Ann. Phys. 2, 471 (1957).
- ¹³Carl A. Levinson and Manoj K. Banerjee, Ann. Phys. 2, 499 (1957).
- ¹⁴A. B. Clegg and G. R. Satchler, Nucl. Phys. 27, 431 (1961).
- ¹⁵W. Tobocman, Theory of Direct Nuclear Reactions (London: Oxford University Press, Amenhouse, 1961), E. C. 4.

- ¹⁶A. K. Kerman, H. McManus, and R. M. Thaler, *Ann. Phys.* 8, 551 (1959).
- ¹⁷Radiation Counting Handbook, Lawrence Radiation Laboratory, University of California, Note CC2-2C, 3 (1966).
- ¹⁸J. B. Cummings, *Ann. Rev. Nucl. Sci.*, 13, 261 (1963).
- ¹⁹SREL Internal Report, SCl (1967).
- ²⁰IAEA Standard Source, Set 80.
- ²¹C. Chasman, K. W. Jones, and R. A. Ristinen, *Nucl. Inst. and Methods* 37, 1 (1965).
- ²²C. Chasman, K. W. Jones, and R. A. Ristinen, *Phys. Rev. Letters* 15, 245 (1965).
- ²³Lindhard, *Mat. and Det. Kom*, 14, 34 (1965).
- ²⁴K. Kim, University of North Carolina, Private Communication.
- ²⁵R. M. Sternheimer, *Rev. Sc. Inst.* 25, No. 11, 9070 (1954).
- ²⁶Ajzenberger Selove and Lauritsen, *Nucl. Phys.* 11, 1, (1959).
- ²⁷E. K. Warburton, K. W. Jones, C. Chasman, and R. A. Ristinen, *Phys. Rev. Letters* 14, 146 (1965).
- ²⁸P. M. Endt and C. Van Der Leun, *Nucl. Phys.* A105, 1, (1967).
- ²⁹Nuclear Data, ed., Katharine Way (New York: Academic Press, 1966), Vol. 2, No. 4.
- ³⁰John M. Blatt and Victor F. Weiskopf, Theoretical Nuclear Physics (New York: John Wiley and Sons, 1952), p. 594.
- ³¹Kai Siegbahn, Alpha-, Beta-, and Gamma-Ray Spectroscopy (Amsterdam: North-Holland Publishing Company, 1965), Vol. 2, p. 1005.
- ³²Amos de-Shalit and Igal Talmi, Nuclear Shell Theory (New York: Academic Press, 1963), p. 156.
- ³³Robert H. Bassel and Colin Wilkin, *Phys. Rev.* 174, 1179 (1968).

- ³⁴C. Broude, P. J. M. Sumulders, and T. K. Alexander, Nucl. Phys. A90, 321 (1967).
- ³⁵J. J. Kolate, R. Auble, and A. Galonsky, Phys. Rev. 162, 957 (1967).
- ³⁶H. Sherif and J. S. Blair, Nucl. Phys. A140, 33 (1970).
- ³⁷K. J. Foley, A. E. Clegg, and G. L. Salmon, Nucl. Phys. 37, 23 (1962).
- ³⁸W. Zobel, F. C. Maionschein, J. H. Todd, and G. T. Chapman, ORNL-4183, UC-34, Physics.
- ³⁹Inglis, Rev. Mod. Phys. 25, 390 (1953).
- ⁴⁰A. Goswami and M. K. Pal, Nucl. Phys. 44, 294 (1963).
- ⁴¹W. P. Alford and K. H. Purser, Nucl. Phys. A132, 86 (1969).
- ⁴²A. M. Green and M. Rito, Nucl. Phys. A130, 112 (1969).
- ⁴³K. H. Purser, W. P. Alford, D. Cline, H. W. Fulbright, H. E. Grove, and M. S. Krick, Nucl. Phys. A132, 75 (1969).
- ⁴⁴J. Nurzynski, Nucl. Phys. A141, 257 (1970).
- ⁴⁵Iwar Miura, Tetsuo Wakatsuki, Yasuo Hirao, and Eiju Okada, J. Phys. Soc. Japan, 14, 239 (1959).
- ⁴⁶S. M. Perez, Nucl. Phys. A136, 599 (1969).
- ⁴⁷C. Glashausser, M. Kondo, M. E. Rickey, and E. Rost, Phys. Letters 14, 113 (1965).
- ⁴⁸J. C. Hiebert, E. Newman, and R. H. Bassel, Phys. Rev. 154, 898 (1967).
- ⁴⁹S. Hinds and R. Middleton, Nucl. Phys. 84, 651 (1966).
- ⁵⁰H. G. Pugh, D. L. Hendrie, Marc Chabre, and E. Boshitz, Phys. Rev. 155, 1054 (1966).
- ⁵¹H. G. Pugh, D. L. Hendrie, Marc Chabre, and E. Boshitz, Phys. Rev. Letters 14, 434 (1965).
- ⁵²Pierre Radvanyi, Jeannine Genin, and Claude Detrax, Phys. Rev. 125, 295 (1962).

- ⁵³A. J. Houdager, T. Y. Li, and S. K. Mark, Can. J. of Phys. 48, 765 (1970).
- ⁵⁴O. Karban, J. Lowe, P. D. Greaves, and V. Hinizdo, Nucl. Phys. A133, 255 (1969).
- ⁵⁵B. A. Watson, R. E. Segel, J. J. Kroepel, and P. P. Singh, Phys. Rev. 187, 1351 (1969).
- ⁵⁶F. S. Goulding, Nucl. Inst. and Meth. 43, 1 (1966).
- ⁵⁷J. W. Mayer, Nucl. Inst. and Meth. 43, 55 (1966).
- ⁵⁸M. G. Strauss, R. N. Larsen, and L. L. Sifter, Nucl. Instr. and Meth. 46, 45 (1967).
- ⁵⁹U. Tamm, W. Michaelis, and P. Coussieu, Nucl. Inst. and Meth. 48, 301 (1967).
- ⁶⁰Millard, Rev. Sc. Instr. 38, 1969 (1967).
- ⁶¹T. Huam and M. Smedsdal, Nucl. Instr. and Meth. 24, 55 (1963).
- ⁶²S. Cohen and D. Kurath, Nucl. Phys. A101, 1 (1967).
- ⁶³J. B. French, Nuclear Spectroscopy (New York and London: Academic Press, 1960), Part B, p. 890.

APPENDIX

TABLE 1
BEAM INTENSITY CALIBRATION

Run No.	Proton Energy	No. of Protons (per 3×10^{-9} Coulombs)
3319	300 MeV	3.38×10^7
3318	300 MeV	2.92×10^7
3150	300 MeV	3.46×10^7
3153	300 MeV	2.82×10^7
3159	300 MeV	3.24×10^7
1026	600 MeV	3.32×10^7
3221	600 MeV	4.46×10^7

TABLE 2
SPECIFICS OF CALIBRATION SOURCES

Source	Calibration Line (MeV)	Intensity (Disintegrations/Sec)
PuBe	4.4381 (2nd escape)	7.98×10^3
Th ²²⁸	2.61447 (2nd escape photo peak)	2.68×10^6
Th ²²⁸	0.859	$.322 \times 10^6$
Th ²²⁸	0.510	(Not used for efficiency)
	0.582	2.33×10^6
Co ⁶⁰	1.17323 (photo peak)	3.85×10^5
	1.3325 (photo peak)	3.85×10^5
Na ²²	1.2746 (photo peak)	(Not used for efficiency)
	0.511 annihilation rays	(Not used for efficiency)
Cs ¹³⁷	0.661595	3.30×10^5
Y ⁸⁸	1.84 (2nd escape photo peak)	8.66×10^4
	0.8975	7.96×10^4

TABLE 3
NEUTRON BACKGROUND AT DETECTOR

TARGET	ENERGY (KeV)	Number of Neutrons/CM ² (per 10 ⁷ Protons)	
		LEAD IN	LEAD OUT
Boron	693.6±2	3.32±.63	1.52±.13
Carbon	694.0±1	3.24±.32	
Nitrogen	694.4±1.4	6.14±.77	1.38±.1
Oxygen	699.4±2	4.06±.45	.782±.07
Magnesium	692.4±1.3	4.42±.34	.36±.08

TABLE 4
SPECIFICS OF TARGETS

Target	Form	Thickness (gm/cm ²)	Isotopic Abundance
Carbon	graphite	4.8	¹² C 98.9%
Oxygen	water	7.37	¹⁶ O ≈ 100 %
Nitrogen	liquid N ₂	5.6±.7	¹⁴ N ≈ 100 %
Calcium	granules	10.5±1.2	⁴⁰ Ca 97 %
Magnesium	granules	5.1±.8	²⁴ Mg 78.8%
			²⁵ Mg 10.1%
			²⁶ Mg 11.1%
Boron	granules	2.2±.3	¹⁰ B 18.8%
			¹¹ B 81.2%

TABLE 5A

UNCERTAINTIES ON ABSOLUTE ENERGY MEASUREMENT AT
300 MeV PROTON ENERGY

(Energies and Uncertainties are in keV)							
Energy	500	1000	2000	3000	4000	5000	6000
Pulser							
Nonlinearity	.6	1.2	1.0	2.0	2.0	3.0	3.0
Interpolation							
Error	.2	.4	.9	2.0	4.0	6.0	8.0

TABLE 5B

UNCERTAINTIES ON ABSOLUTE ENERGY MEASUREMENT AT
600 MeV PROTON ENERGY

(Energies and Uncertainties are in keV)						
Energy	1000	2000	3000	4000	5000	6000.
Pulser						
Nonlinearity	1	3.3	4.2	5.3	6	6
Interpolation						
Error	1.6	3	5	6.5	8	10

TABLE 6A
 UNCERTAINTIES ON ABSOLUTE CROSS SECTIONS FOR
 300 MeV PROTON ENERGY

Energy (MeV)	2.0	4.0	6.0
Pile Up Losses	14%	14%	14%
Detector Efficiency	10%	15%	40%
$^{12}\text{C}(p,)^{11}\text{C}$ Cross Section	10%	10%	10%
Ion Chambers	10%	10%	10%

TABLE 6B
 UNCERTAINTIES ON ABSOLUTE CROSS SECTIONS FOR
 600 MeV PROTON ENERGY

Energy (MeV)	2.0	4.0	6.0
Pile Up Losses	15%	15%	5%
Detector Efficiency	10%	15%	40%
$^{12}\text{C}(p,)^{11}\text{C}$ Cross Section	13%	13%	13%
Ion Chambers	15%	15%	15%

TABLE 7

BORON TARGET

ELEMENT	TRANSITION ENERGY EXPERIMENTAL (MeV)	BRANCHING RATIO	TRANSITION	LIFETIME $\times 10^{-14}$ SEC (MULTIPOLARITIES)	$4\pi Id\sigma/d\Omega$ (mbarns)	WIDTH EXPERIMENTAL (keV)
^{11}B	(DE) 2.1274		$2.127 \rightarrow 0$.494 (M1)	5 ± 3.4	70.4
	(PP) 2.127		$1/2^- \rightarrow 3/2^-$		< 4.5	70.6
	4.429 \pm .009		$4.459 \rightarrow 0$.144 (M1)	$3.4 \pm .7$	147 ± 27
			$(5/2^-) \rightarrow 3/2^-$			
	5.035	.88	$5.035 \rightarrow 0$.0385 (M1)	$1.36 \pm .42$	158
			$3/2^- \rightarrow 3/2^-$			
	2.908	.12	$5.035 \rightarrow 2.127$.410 (M1)		
			$3/2^- \rightarrow 1/2^-$			
	6.758	.83	$6.758 \rightarrow 0$			
			$(7/2^-) \rightarrow (3/2^-)$			
2.299	.17	$6.758 \rightarrow 4.459$				
		$(7/2^-) \rightarrow (5/2^-)$				
6.808	.79	$6.808 \rightarrow 0$				
		$(3/2^-) \rightarrow 3/2^-$				
4.581	.21	$6.808 \rightarrow 2.127$				
		$(3/2^-) \rightarrow 1/2^-$				

TABLE 7--Continued

ELEMENT	TRANSITION ENERGY EXPERIMENTAL (MeV)	BRANCHING RATIO	TRANSITION	LIFETIME $\times 10^{-14}$ SEC (MULTIPOLARITIES)	$4\pi I\sigma/d\Omega$ (mbarns)	WIDTH EXPERIMENTAL (keV)
^{10}B	$.7166 \pm .0008$		$.717 \rightarrow 0$ $1^+ \rightarrow 0^+$	9.7×10^4	$6.98 \pm 1.$	19.2 ± 2
Cascade	1.018		$1.739 \rightarrow .717$ $0^+ \rightarrow 1^+, \Delta T=1$	13.8	$1.73 \pm 1.$	14
Direct	11		11	11	$2.13 \pm 2.$	36 ± 20
	(DE) 2.152 (PP)	.3	$2.152 \rightarrow 0$ $1^+ \rightarrow 3^+$	1420	< 1.52 $< .77$	14 14
	1.435	.4	$2.152 \rightarrow .717$ $1^+ \rightarrow 1^+$	1090	$1.44 \pm .6$	14
	$.411 \pm .017$.3	$2.152 \rightarrow 1.739$ $1^+ \rightarrow 0^+, \Delta T=1$	771	$1.98 \pm .6$	14.5 ± 3.3
^{10}Be	$3.3546 \pm .003$		$3.368 \rightarrow 0$ $2^+ \rightarrow 0^+$	17	$5.55 \pm .7$	70 ± 6

TABLE 8

CARBON TARGET (300 MeV)

ELEMENT	TRANSITION ENERGY EXPERIMENTAL (MeV)	BRANCHING RATIO	TRANSITION (MULTIPOLARITIES)	LIFETIME $\times 10^{-14}$ SEC	$4\pi d\sigma/d\Omega$ (mbarns)	WIDTH EXPERIMENTAL (keV)
^{12}C	$4.4293 \pm .004$		$4.44 \rightarrow 0$ $2^+ \rightarrow 0^+$	5.63	$4.12 \pm .3$	177 ± 10

TABLE 9

CARBON TARGET (600 MeV)

ELEMENT	TRANSITION ENERGY EXPERIMENTAL (MeV)	BRANCHING RATIO	TRANSITION	LIFETIME $\times 10^{-14}$ SEC (MULTIPOLARITIES)	$4\pi I d\sigma/d\Omega$ (mbarns)	WIDTH EXPERIMENTAL (keV)
^{12}C	$4.4397 \pm .0029$		$4.44 \rightarrow 0$ $2^+ \rightarrow 0^+$	5.63(E2)	$2.9 \pm .2$	157 ± 7.8
^{11}B	2.127		$2.13 \rightarrow 0$ $1/2^- \rightarrow 3/2^-$.494(M1)	$.91 \pm .18$	35
			$4.46 \rightarrow 0$ $5/2^- \rightarrow 3/2^-$.114(M1)		
		.88	$5.03 \rightarrow 0$ $3/2^- \rightarrow 3/2^-$.0385(M1)		
		.12	$5.03 \rightarrow 2.127$ $3/2^- \rightarrow 3/2^-$.410(M1)		
		.83	$6.758 \rightarrow 0$ $7/2^- \rightarrow 3/2^-$			
		.17	$6.758 \rightarrow 4.459$ $7/2^- \rightarrow 5/2^-$			

TABLE 9--Continued

ELEMENT	TRANSITION ENERGY EXPERIMENTAL (MeV)	BRANCHING RATIO	TRANSITION	LIFETIME $\times 10^{-14}$ SEC (MULTIPOLARITIES)	$4\pi I_{d\sigma}/d\Omega$ (mbarns)	WIDTH EXPERIMENTAL (keV)
^{11}C		.79	6.808 \rightarrow 0			
			$3/2^- \rightarrow 1/2^-$			
		.21	6.808 \rightarrow 2.127			
			$3/2^- \rightarrow 1/2^-$			
			1.99 \rightarrow 0		2.002	.42 \pm .08
			$1/2^- \rightarrow 3/2^-$			
			4.32 \rightarrow 0			
			$5/2^- \rightarrow 3/2^-$			
			4.81 \rightarrow 0			
			$3/2^- \rightarrow 3/2^-$			
			6.35 \rightarrow 0			
			$3/2^- \rightarrow 3/2^-$			
		6.49 \rightarrow 0				
		$3/2^- \rightarrow 3/2^-$				

TABLE 10

NITROGEN TARGET

ELEMENT	TRANSITION ENERGY EXPERIMENTAL (MeV)	BRANCHING RATIO	TRANSITION	LIFETIME $\times 10^{-14}$ SEC (MULTIPOLARITIES)	$4Hd\sigma/d\Omega$ (mbarns)	WIDTH EXPERIMENTAL (kev)
^{14}N	Cascade 2.312		$2.311 \rightarrow 0$	7.9 (M1)	(PP) < .524	14
			$0^+ \rightarrow 1^+, \Delta T = 1$		(DE) < .431	14
	Direct	.04	$3.945 \rightarrow 0$	13.5	(PP) < 1.24	62
			$1^+ \rightarrow 1^+$		(DE) < 1.06	62
^{12}C	1.637	.96	$3.945 \rightarrow 2.312$.47	< .47	46
			$1^+ \rightarrow 0^+, \Delta T = 1$			
	4.910		$4.910 \rightarrow 0$	< 56.6	< .37	129
			$0^- \rightarrow 1^+$			
5.10	.67	$5.10 \rightarrow 0$	1508 (E1)	< .07	14	
		$2^- \rightarrow 1^+$				
2.792	.33	$5.10 \rightarrow 2.312$	4180 (M2)	(PP) < 1.63	14	
		$2^- \rightarrow 0^+, \Delta T = 1$		(DE) 1.4 \pm 1.		
^{12}C	4.432 \pm .003		$4.44 \rightarrow 0$		9.5 \pm .6	162 \pm 8
			$2^+ \rightarrow 0^+$			

TABLE 11

OXYGEN TARGET (300 MeV)

ELEMENT	TRANSITION ENERGY EXPERIMENTAL (MeV)	BRANCHING RATIO	TRANSITION	LIFETIME $\times 10^{-14}$ SEC (MULTIPOLARITIES)	$4\pi d\sigma/d\Omega$ (mbarns)	WIDTH EXPERIMENTAL (keV)
^{16}O	$6.1288 \pm .0009$		$6.3 \rightarrow 0$ $3^- \rightarrow 0^+$	(E3)	$.56 \pm .1$	15 ± 2.3
^{15}N	$5.2692 \pm .004$		$5.27 \rightarrow 0$ $5/2^+ \rightarrow 1/2^-$	270 (E3/M2)	$.38 \pm .16$	23.6 ± 9
			$5.3 \rightarrow 0$ $1/2^+ \rightarrow 1/2^-$	<50 (E1)		
	$6.3187 \pm .004$		$6.33 \rightarrow 0$ $3/2^- \rightarrow 1/2^-$	<50 (E2/M1)	$1.91 \pm .3$	96 ± 12
^{15}O			$5.20 \rightarrow 0$ $1/2^+ \rightarrow 1/2^-$	<50 (E1)		
	$5.2409 \pm .0031$		$5.24 \rightarrow 0$ $5/2^+ \rightarrow 1/2^-$	320 (E3/M2)	$.43 \pm .15$	22 ± 7
	$6.1622 \pm .003$		$6.165 \rightarrow 0$ $3/2^- \rightarrow 1/2^-$	<50 (E2/M1)	$4.03 \pm .3$	118.5 ± 7
^{14}N	5.104	.67	$5.104 \rightarrow 0$ $2^- \rightarrow 1^+$	1580 (E1)	$.12 \pm .05$	20
	2.794	.33	$5.104 \rightarrow 2.312$ $2^- \rightarrow 0^+, \Delta T=1$	4.40	(PP) < .31 (DE) < .09	14
Cascade	2.312		$2.312 \rightarrow 0$ $0^+ \rightarrow 1^+, \Delta T=1$	7.9	(PP) $.42 \pm .38$ (DE) $.51 \pm .3$	14

TABLE 11--Continued

ELEMENT	TRANSITION ENERGY EXPERIMENTAL (MeV)	BRANCHING RATIO	TRANSITION	LIFETIME $\times 10^{-14}$ SEC (MULTIPOLARITIES)	$4\pi I d\sigma/d\Omega$ (mbarns)	WIDTH EXPERIMENTAL (keV)
Direct	2.312		$2.312 \rightarrow 0$	7.9	(PP) 1.3 ± 1	
			$0^+ \rightarrow 1^+, \Delta T = 1$		(DE) 1.6 ± 1	62
^{12}C	$4.4526 \pm .004$		$4.44 \rightarrow 0$	5.63	$4.43 \pm .34$	189.4 ± 12
			$2^+ \rightarrow 0^+$			
^{10}B Cascade	1.018		$1.739 \rightarrow .717$	13.8	$< .12$	14
			$0^+ \rightarrow 1^+, \Delta T = 1$			
Direct	$.720 \pm .0016$		11	11	$< .28$	38
			$.717 \rightarrow 0$	9.7×10^4	$.6 \pm .09$	19
	2.152	.3	$2.152 \rightarrow 0$	1420	(PP) $< .311$	
			$1^+ \rightarrow 3^+$		(DE) $< .38$	14
	1.435	.4	$2.152 \rightarrow .717$	1090 (M1)	$.25 \pm .2$	14
			$1^+ \rightarrow 1^+$			
	.411	.3	$2.152 \rightarrow 1.739$	771	$.14 \pm .08$	14
			$1^+ \rightarrow 0^+, \Delta T = 1$			

TABLE 12

OXYGEN TARGET (600 MeV)

ELEMENT	TRANSITION ENERGY EXPERIMENTAL (MeV)	BRANCHING RATIO	TRANSITION	LIFETIME $\times 10^{-14}$ SEC (MULTIPOLARITIES)	$4\pi d\sigma/d\Omega$ (mbarns)	WIDTH EXPERIMENTAL (keV)
^{16}O	$6.1308 \pm .0008$		$6.13 \rightarrow 0$ $3^- \rightarrow 0^+$	(E3)	$1.12 \pm .164$	20 ± 1
^{15}N	$5.2705 \pm .0022$ $5.2713 \pm .0022$		$5.27 \rightarrow 0$ $5/2^+ \rightarrow 1/2^-$	270 (E3/M2)	$.59 \pm .17$ $.59 \pm .17$	23 ± 6 21 ± 5
	$6.3127 \pm .005$		$5.31 \rightarrow 0$ $1/2^+ \rightarrow 1/2^-$	< 50 (E1)		
			$6.33 \rightarrow 0$ $3/2^- \rightarrow 1/2^-$	< 50 (E2/M1)	$3. \pm .4$	109.5 ± 12.6
^{15}O			$5.20 \rightarrow 0$ $1/2^+ \rightarrow 1/2^-$	< 50 (E1)		
	$5.2393 \pm .0023$ $5.2394 \pm .0027$		$5.24 \rightarrow 0$ $5/2^+ \rightarrow 1/2^-$	320 (E3/M2)	$.46 \pm .16$ $.46 \pm .14$	20 ± 6 26 ± 7
	$6.1599 \pm .0055$		$6.165 \rightarrow 0$ $3/2^- \rightarrow 1/2^-$	< 50 (E2/M1)	$3.39 \pm .45$	113 ± 11
^{14}N	$5.1043 \pm .0027$.67	$5.104 \rightarrow 0$ $2^- \rightarrow 1^+$	1580 (E1)	$.34 \pm .11$	26 ± 6.5
	2.792	.33	$5.104 \rightarrow 2.312$ $2^- \rightarrow 0^+, \Delta T=1$	4140	(PP) < .64 (DE) < .13	13

TABLE 12--Continued

ELEMENT	TRANSITION ENERGY EXPERIMENTAL (MeV)	BRANCHING RATIO	TRANSITION (MULTIPOLARITIES)	LIFETIME $\times 10^{-14}$ SEC (MULTIPOLARITIES)	$4\pi I_0\sigma/d\Omega$ (mbarns)	WIDTH EXPERIMENTAL (keV)		
^{12}C	2.312		2.312 \rightarrow 0 $0^+ \rightarrow 1^+, \Delta T=1$		(PP) < .39 (DE) .79 \pm .6	13		
			4.43 \rightarrow 0 $2^+ \rightarrow 0^+$		5.63		3.7 \pm .3	147 \pm 9
^{10}B	1022		1.739 \rightarrow .717 $0^+ \rightarrow 1^+, \Delta T=1$	13.8		11		
			Direct					< .33
^{12}C	2.152	.3	.717 \rightarrow 0 $1^+ \rightarrow 3^+$	9.7 $\times 10^4$		15		
			2.152 \rightarrow 0 $1^+ \rightarrow 3^+$				1420	(PP) < .41 (DE) < .43
			1.435				1090 (ML)	.52 \pm .18
^{10}B	1.739	.3	2.152 \rightarrow 1.739 $1^+ \rightarrow 0^+, \Delta T=1$	771		15		
			Direct					

TABLE 13

MAGNESIUM TARGET (300 MeV)

ELEMENT	TRANSITION ENERGY EXPERIMENTAL (MeV)	BRANCHING RATIO	TRANSITION	LIFETIME $\times 10^{14}$ SEC (MULTIPOLARITIES)	$4\pi I d\sigma/d\Omega$ (mbarns)	WIDTH EXPERIMENTAL (keV)
^{25}Mg	$.584 \pm .003$.5	$.584 \rightarrow 0$ $1/2^+ \rightarrow 5/2^+$	490000 (E2)	20 ± 5	18 ± 4
			$1.962 \rightarrow .584$ $5/2^+ \rightarrow 1/2^+$	66		
			$1.962 \rightarrow 0$ $5/2^+ \rightarrow 5/2^+$			
			$1.611 \rightarrow 0$ $5/2^+ \rightarrow 5/2^+$	2.2		
^{24}Mg	$1.3718 \pm .003$.49	$.976 \rightarrow .584$ $3/2^+ \rightarrow 1/2^+$	700 (M1/E2)		
			$.976 \rightarrow 0$ $3/2^+ \rightarrow 5/2^+$	700 (M1)		
^{23}Na	$1.641 \pm .003$.9	$1.369 \rightarrow 0$ $2^+ \rightarrow 0^+$	140 (E2)	8.6 ± 2.3	45 ± 9.5
			$.439 \rightarrow 0$ $5/2^+ \rightarrow 3/2^+$	160 (M1)		
			$2.080 \rightarrow .439$ $7/2^+ \rightarrow 5/2^+$	> 4.1	$1.5 \pm .6$	14

TABLE 13--Continued

ELEMENT	TRANSITION ENERGY EXPERIMENTAL (MeV)	BRANCHING RATIO	TRANSITION	LIFETIME $\times 10^{-14}$ SEC (MULTIPOLARITIES)	$4\pi I d\sigma/d\Omega$ (mbarns)	WIDTH EXPERIMENTAL (keV)
^{23}Mg		.1	2.080 \rightarrow 0 7/2 $^+$ \rightarrow 3/2 $^+$	4.1 (E2)		
		.65	2.391 \rightarrow 0 1/2 $^+$ \rightarrow 3/2 $^+$			
		.35	2.391 \rightarrow .439 1/2 $^+$ \rightarrow 5/2 $^+$			
			2.64 \rightarrow 0 1/2 $^+$ \rightarrow 3/2 $^+$	>1.5	3.2 \pm 2.2	95 \pm 53
			.449 \rightarrow 0 5/2 $^+$ \rightarrow 3/2 $^+$		4.4 \pm 1.5	17 \pm 6
		.85	2.04 \rightarrow .449 7/2 $^+$ \rightarrow 5/2 $^+$		1.8 \pm .8	14 \pm 4
		.15	2.04 \rightarrow 0 7/2 $^+$ \rightarrow 3/2 $^+$			
		.7	2.35 \rightarrow .449 1/2 $^+$ \rightarrow 5/2 $^+$			
		.3	2.35 \rightarrow 0 1/2 $^+$ \rightarrow 3/2 $^+$			

TABLE 13--Continued

ELEMENT	TRANSITION ENERGY EXPERIMENTAL (MeV)	BRANCHING RATIO	TRANSITION	LIFETIME $\times 10^{-14}$ SEC (MULTIPOLARITIES)	$4\pi\sigma/d\Omega$ (mbarns)	WIDTH EXPERIMENTAL (keV)
^{16}O	2.791±.010		2.77→0 3/2		2.3±1.1	64±24
	3.342±.002	.9	3.798→.451 3/2 ⁻ →5/2 ⁺		.81±.5	17±6
	6.133±.002		6.13→0 3 ⁻ →0 ⁺		1±.2	27±4

TABLE 14
 CROSS SECTIONS FOR EXCITATION OF LEVELS IN ^{23}Mg AND ^{23}Na
 FOR NATURAL MAGNESIUM TARGET

	Level	Cross Section (mbarns)	Level	Cross Section (mbarns)
^{23}Na	2.080 $7/2^+$	$1.7 \pm .7$	^{23}Mg 2.040 $7/2^+$	2.2 ± 1.0
	2.64 $1/2^+$	3.2 ± 2.2	2.77 ($1/2^+$)	2.3 ± 1.1
	.439 $5/2^+$.449 $5/2^+$	1.4 ± 2.3
			3.8 $3/2^-$	$.9 \pm .6$

TABLE 15

CALCIUM TARGET (300 MeV)

ELEMENT	TRANSITION ENERGY EXPERIMENTAL (MeV)	BRANCHING RATIO	TRANSITION	LIFETIME X 10 ⁻¹⁴ SEC (MULTIPOLARITIES)	4πdσ/dr (mbarns)	WIDTH EXPERIMENTAL (keV)
39Ca	1.459		2.47→0 1/2 ⁺ →3/2 ⁺	>10	1.4±.3	41
			2.80→0 (5/2, 7/2) ⁻ →3/2 ⁺		3.0±1.6	23±8
	2.75±.002		3.03			
			3.94 (1/2, 3/2) ⁻			
			5.13→0 (3/2, 5/2) ⁺ →3/2 ⁺		.9±.13	39±9
39K	6.127±.003		5.48→0			
			6.13→0		1.2±.3	40±7
	1.506		2.53→0 1/2 ⁺ →3/2 ⁺	>10	3.8±2.4	41
			2.82→0 7/2 ⁻ →3/2 ⁺	1000	5.6±1	29±4

TABLE 15--Continued

ELEMENT	TRANSITION ENERGY EXPERIMENTAL (MeV)	BRANCHING RATIO	TRANSITION	LIFETIME X 10 ⁻¹⁴ SEC (MULTIPOLARITIES)	4Hdσ/dr (mbarns)	WIDTH EXPERIMENTAL (keV)
³⁸ Ca	5.259±.005		5.28→0 (3/2→5/2) ⁺ 3/2 ⁺		1±.3	48±11
			5.62→0			
	6.299±.004		6.35→0		.5±.3	28±11
⁴⁰ Ca			2.2→0 2 ⁺ →0			
			3.72 3 ⁻			
			4.36 0 ⁺			
			4.84 (2 ⁺)			
	3.737±.001		3.73→0 3 ⁻ →0 ⁺	8500 (E3)	2.5±.25	18±2
		4.48→3.73 5 ⁻ →3 ⁻				

TABLE 15--Continued

ELEMENT	TRANSITION ENERGY EXPERIMENTAL (MeV)	BRANCHING RATIO	TRANSITION	LIFETIME $\times 10^{14}$ SEC (MULTIPOLARITIES)	$4\pi I d\sigma/dr$ (mbarns)	WIDTH EXPERIMENTAL (keV)
^{38}Ar		.65	$5.6 \rightarrow 3.73$ $4^- \rightarrow 3^-$			
		.35	$5.6 \rightarrow 4.48$ $4^- \rightarrow 5^-$			
			$6.8 \rightarrow 0$			
^{20}Ne			$3.81 \rightarrow 2.167$ $3^- \rightarrow 2^+$			
			$2.21 \rightarrow 0$			
^{36}A			$2^+ \rightarrow 6^+$ 1.64			
			$1.99 \rightarrow 0$ $2^+ \rightarrow 0^+$			
^{32}S			2.21			
	$1.376 \pm .002$				3.9 ± 2.4	15 ± 7
	$2.734 \pm .002$ $(1.712 \pm .002)$				8.23 ± 3.53 (DE) 19.1 ± 8 (P)	73 ± 24

TABLE 15--Continued

ELEMENT	TRANSITION ENERGY EXPERIMENTAL (MeV)	BRANCHING RATIO	TRANSITION	LIFETIME $\times 10^{-14}$ SEC (MULTIPOLARITIES)	$4\pi I\sigma/d\Omega$ (mbarns)	WIDTH EXPERIMENTAL (keV)
	3.163±.002 (2.141±.002)				2.35±.6 (DE) 10.5±3 (P)	24±5
	3.193±.001 (2.171±.001)				1.93±.6 (DE) 5±1.6 (P)	16±4
	3.252±.003 (2.230±.003)				2.35±.6 (DE) 12.1±3 (P)	42±8

TABLE 16

BORON TARGET

ELEMENT	LEVEL	$4\pi d\sigma/d\Omega$ (mbarns) THIS EXPERIMENT	$^{11}\text{B}(P, _)$ (a)	$^{10}\text{B}(P, _)$ (b)	$(P, _)$ (c)	(P, P') (d)	(P, P') (e)	$^{10}\text{B}(P, P)$ (f)
^{11}B	2.127 \rightarrow 0	5 \pm 3.4		2.1 \pm .8	1.25 \pm .06		.3	
	4.459 \rightarrow 0	3.4 \pm .7	3.8 \pm .06		1.6 \pm .2	3.8 \pm .2	1.	
	5.035 \rightarrow 0	1.36 \pm .42	<.5		.4 \pm .1			
	5.035 \rightarrow 2.127				1.0 \pm .2			
	6.758 \rightarrow 0		1.3 \pm .7		.8 \pm .1		.8	
	6.758 \rightarrow 4.459							
^{10}B	6.808 \rightarrow 0							
	6.808 \rightarrow 2.127							
	.717 \rightarrow 0	6.98 \pm 1.	12 \pm 1.6	1.8 \pm .9				8.5
	1.739 \rightarrow .717	3.86 \pm 2.2	8 \pm 1.	1.0 \pm .3	3.1 \pm .8			1.07
	2.152 \rightarrow 0	<.77	1.8 \pm .6	1. \pm .4				5.4
	2.152 \rightarrow .717	1.44 \pm .6	3.5 \pm .9	.7 \pm .3	1.4 \pm 1.2			
2.152 1.739	1.98 \pm .6							

TABLE 16--Continued

ELEMENT	LEVEL	$4\pi I d\sigma/d\Omega$ (mbarns) THIS EXPERIMENT	(a) $^{11}\text{B}(P, _)$	(b) $^{10}\text{B}(P, _)$	(c) $(P, _)$	(d) (P, P')	(e) (P, P')	(f) $^{10}\text{B}(P, P)$
^{10}Be	3.368 ± 0	5.55 ± 0.7	3 ± 0.6		1.0 ± 0.2			
7	(a) 150 MeV protons on natural boron							
7	(b) 150 MeV protons on ^{10}B							
38	(c) 50.6 MeV protons, $d\sigma/d\Omega$ (mb/sr) at 135° γ -ray angle							
54	(d) 30.3 MeV proton, $d\sigma/d\Omega$ at $\approx 43^\circ$ C.M.							
53	(e) 100 MeV protons, relative amplitudes shown at 22° (Lab)							
55	(f) 12 MeV protons, total cross section (mbarns)							

TABLE 17

CARBON TARGET

ELEMENT	LEVEL	$4\pi d\sigma/d\Omega$ THIS EXPERIMENT	(a) (P, $\bar{}$)	(b) (P, $\bar{}$)	(c) (P, D)	(d) (P, D)	(e) (P, 2P)
^{12}C	4.44 \rightarrow 0	2.9 \pm .2	6.6 \pm 1.0	.89 \pm .23*			
^{11}B	2.13 \rightarrow 0	.91 \pm .18					1
	4.46 \rightarrow 0			3.5 \pm .3			.9
	5.03 \rightarrow 0		2.3 \pm 1.				.8
	5.03 \rightarrow 2.127						
	6.76 \rightarrow 0		2.1 \pm .7	.24 \pm .09*			1.1
	6.76 \rightarrow 4.459						
	6.08 \rightarrow 0						
	6.08 \rightarrow 2.127						
^{11}C	1.99 \rightarrow 0	.42 \pm .08		2.3 \pm 2.0	1	1	
	4.32 \rightarrow 0			.9 \pm .1	1.2	.7	
	4.81 \rightarrow 0					.8	
	6.35 \rightarrow 0				.4		
	6.49 \rightarrow 0					.7	

TABLE 17--Continued

ELEMENT	LEVEL	$4\pi I_{d\sigma}/d\Omega$ THIS EXPERIMENT	(a) (P,)	(b) (P,)	(c) (P, D)	(d) (P, D)	(e) (P, 2P)
^{10}B	.72→0		4.5±.5				
	1.74→.72		1.8±.2				
	2.15→1.74		.6±.2				
	3.58→.72		.9±.4				

⁷(a) 150 MeV protons γ ray detected

³⁸(b) 50 MeV protons 135° γ -ray angle; *145 MeV protons

⁵²(c) 154 MeV protons, deuterons detected at 20° (Lab), relative cross sections

⁵¹(d) 50 MeV protons, deuterons at 23° (Lab), relative cross sections

⁵⁰(e) 50 MeV protons, angle between exiting protons -35°, relative cross sections

TABLE 18
NITROGEN TARGET

ELEMENT	LEVEL	$4\pi d\sigma/d\Omega$ THIS EXPERIMENT	(a) (P, <u> </u>)
^{14}N	2.311→0	<.5	.6±.2
	3.945→0		
	3.945→2.312	<.47	.4±.1
	4.910→0	<.37	
	5.10→0	<.07	
	5.10→2.312	1.4±1.0	
^{12}C	4.44→0	9.5±.6	20±.5
^{10}B	.72→0		3±.5
	1.74→.72		1±.2

⁷(a) 150 MeV protons, γ ray observed, σ (mbarns)

TABLE 19

OXYGEN TARGET (300 MeV)

ELEMENT	LEVEL	$4\pi d\sigma/d\Omega$ THIS EXPERIMENT	(a) (P,)	(b) (P,)	(c) (D,T) (D, ^3He)	(d) (D, ^3H)
^{16}O	6.13 \rightarrow 0	.56 \pm .1	22.7 \pm 3	6.8 \pm .5*		
^{15}N	5.27 \rightarrow 0	.38 \pm .16	2.6 \pm .7	4.1 \pm .5*	.36	.31
	5.3 \rightarrow 0					.039
^{15}O	6.33 \rightarrow 0	1.91 \pm .3		4.4 \pm 1.6		3.72
	5.20 \rightarrow 0				.027	
	5.24 \rightarrow 0	.43 \pm .15		.96 \pm .39	.043	
^{14}N	6.165 \rightarrow 0	4.03 \pm .3			3.1	
	5.104 \rightarrow 0	.12 \pm .05				
	5.104 \rightarrow 2.312	<.09				
^{12}C	2.312 \rightarrow 0	2 \pm 1.1	2.9 \pm .8			
	4.44 \rightarrow 0	4.43 \pm .34	8.3 \pm 1.7	1.26 \pm .46		
^{10}B	1.739 \rightarrow .717	<.12	4.4 \pm 1.1			
	.717 \rightarrow 0	.6 \pm .09	3.9 \pm 1.0			
	2.152 \rightarrow 0	<.31				

TABLE 19--Continued

ELEMENT	LEVEL	$4I\sigma/d\Omega$ THIS EXPERIMENT	(a) (P, <u> </u>)	(b) (P, <u> </u>)	(c) (D, T)	(d) ^3_3H (D, ^3He)
	2.152→.717	.25±.2	1.0±.5			
	2.152→1.739	.14±.08				

³(a) 150 MeV protons, γ ray observed, σ (mbarns)

³⁸(b) 145 MeV protons, σ (mb/sr) γ ray at 135°, * 43 MeV protons

⁴³(c) 20 MeV deuterons, spectroscopic factors

⁴⁸(d) 20 MeV deuterons, spectroscopic factors

TABLE 20

MAGNESIUM TARGET

ELEMENT	TRANSITION	$4\pi d\sigma/d\Omega$ THIS EXPERIMENT	(a) (P, $_$)	(b) (P, $_$)	(c) (P, P')	(d) $^{26}\text{Mg}(\text{}^3\text{He}, \alpha)^{25}\text{Mg}$
^{25}Mg	0.584 \rightarrow 0	20 \pm 5			(no estimate given but was seen)	.06
	1.962 \rightarrow .967				1	.089
	1.962 \rightarrow .584				10	.038
	1.962 \rightarrow 0				7	.106
^{24}Mg	0.976 \rightarrow 0.584					
	0.976 \rightarrow 0					
^{23}Na	1.369 \rightarrow 0	8.6 \pm 2.3	36.6 \pm 5	18 \pm 9	100 (next largest =7)	
	0.439 \rightarrow 0					
	2.08 \rightarrow .439	1.5 \pm .6		16 \pm 9		
	2.08 \rightarrow 0					
	2.391 \rightarrow 0					
	2.391 \rightarrow .439					

TABLE 20--Continued

ELEMENT	TRANSITION	$4\pi d\sigma/d\Omega$ THIS EXPERIMENT	(a) (P, $\bar{\nu}$)	(b) (P, $\bar{\nu}$)	(c) (P, P')	(d) $^{26}\text{Mg}(^3\text{He}, \alpha)^{25}\text{Mg}$
^{23}Mg	2.64 \rightarrow 0	3.2 \pm 1.1	23 \pm 5	4.7 \pm 1.6		
	.449 \rightarrow 0	4.4 \pm 1.5				
	2.04 \rightarrow .449	1.8 \pm .8				
	2.04 \rightarrow 0					
	2.35 \rightarrow .449					
^{16}O	2.35 \rightarrow 0					
	2.77 \rightarrow 0	2.3 \pm 1.1				
	3.798 \rightarrow .451	.81 \pm .5				
	6.13 \rightarrow 0	1 \pm .2				
					1.9 \pm 1.2	

33 (a) 150 MeV protons, γ -ray observed, σ (mbarns)

34 (b) 40 MeV protons, $d\sigma/d\Omega$ at γ -ray angle of 135 $^\circ$

41 (c) 5.7 MeV protons, γ ray observed, relative intensity

40 (d) 10.2 MeV ^3He , spectroscopic factors

TABLE 21

CALCIUM TARGET

ELEMENT	LEVEL	${}^4\text{He}d\sigma/d\Omega$ THIS EXPERIMENT	(a) (P, $_$)	(b) (P, P')	(c) (He 3 , α)	(d, t)	(d) (d, ${}^3\text{He}$)	(e) (t, α)
${}^{39}\text{Ca}$	2.47 \rightarrow 0	1.4 \pm 1.3	35 \pm 10		1	.83		
	2.80 \rightarrow 0	3.0 \pm 1.6				.43		
	3.03					yes		
	3.94							
	5.13 \rightarrow 0	.9 \pm .3			.7	1.66		
	5.48 \rightarrow 0				.3	no		
${}^{39}\text{K}$	6.13 \rightarrow 0	1.2 \pm .3			.7	no		
	2.53 \rightarrow 0	3.8 \pm 2.4					1.62	51
	2.82 \rightarrow 0	5.6 \pm 1					.46	16.5
	5.28 \rightarrow 0	1. \pm .3					1.09	25.2
	5.62 \rightarrow 0						.68	19.6
${}^{40}\text{Ca}$	6.35 \rightarrow 0	.5 \pm .3						
	3.73 \rightarrow 0	2.5 \pm .25	13 \pm 4	8 \pm .5			1.26	29.9
	4.48 \rightarrow 3.73			1.21 \pm .19				

TABLE 21--Continued

ELEMENT	LEVEL	$4\pi d\sigma/d\Omega$ THIS EXPERIMENT	(a) (P, <u> </u>)	(b) (P, P')	(c) (He ³ , α)	(d) (d, t)	(e) (t, α)
	5.6→3.73			1 ± .15			
	5.6→4.48						
	6.8→0			1.1 ± .15			
³⁸ A _T	2.21→0		32 ± 5				
³⁶ A _T	1.99→0		37 ± 9				
³² S	2.21		65 ± 9				
¹ (a)	150 MeV protons, γ -ray detected, $4\pi d\sigma/\Omega$						
³⁷ (b)	150 MeV protons, σ , scattered proton and γ -ray detected						
⁴⁶ (c)	27.5 MeV protons, 30 MeV ³ He, exit particle detected, relative amplitude at 30° (Lab)						
⁴⁷ (d)	Spectroscopic factor						
⁴⁸ (e)	Triton energy--9.6 MeV, relative amplitudes						

TABLE 22

CHARACTERISTICS OF PULSE SHAPE DISCRIMINATOR

Linear stages	
Rise time	15 ns
Gain	20
Noise (referenced to input of pre-amplifier)	30 KeV rms
Overall	
Sensitivity	.5 MeV (10 MV)
Dynamic range	20 to 1.
Rejection ratio	100% for 5% slow component over entire range

TABLE 23

CHARACTERISTICS OF CHARGE SENSITIVE PREAMPLIFIER

Output range	± 10 V.
Input capacitance range	20-70 pf.
Rise time (30 pf. input capacitance)	10 n sec.
Noise contribution	10 KeV F W.H.M.
Output	20mv/MeV into 50Ω
Output impedance	50 - 125Ω
Decay time constant	8.2 μ sec
Supply voltages	± 24 v
	- 12 v

FIGURE CAPTIONS

Figure

1. Layout of experimental area. A is the charged-particle, anti-coincidence detector and C is the monitor counter.
2. Block diagram of logic and linear electronics. The five signals on the left originate in the experimental area.
3. External proton beams of the SREL synchrocyclotron. The target was located just upstream of BM3 (monitor ion chamber).
4. Count rate as a function of beam current. The count rate is for all "good" events between 1 and 6 MeV.
5. Total efficiency of the Ge(Li) detector. The sources used are indicated on the figure and in Table 2. The data were obtained by placing the sources at the location of the center of the target. The solid line is an eye fit to the data points extended based on Monte Carlo efficiency calculations of reference 24.
6. γ -ray spectrum obtained for a boron target of 300 MeV proton energy. The solid lines are the best fit over the indicated region.
7. γ -ray spectrum obtained for a carbon target of 300 MeV proton energy.
8. γ -ray spectrum obtained for a carbon target of 600 MeV proton energy.
9. γ -ray spectrum obtained for a liquid nitrogen target at 300 MeV proton energy. The Xs give the spectrum shape after subtracting out the contribution from the ^{12}C 4.44 MeV line.
10. The γ -ray spectrum obtained for a water target at 300 MeV proton energy.
11. The γ -ray spectrum obtained for a water target at 600 MeV proton energy.
12. The γ -ray spectrum obtained for a magnesium target at 300 MeV proton energy.

13. The γ -ray spectrum obtained for a calcium target at 300 MeV proton energy.
14. Proton differential cross sections used in calculating the Doppler broadening of the ^{12}C 4.44 MeV line. The curve labeled A is reproduced from Bassel and Wilkens³¹ and that labeled C from Clegg, et al.¹⁶
15. Comparison of Monte Carlo and first order Doppler calculations with the data obtained for the 4.44 MeV line of ^{12}C . The bar gives the statistical error on the data. The abscissas gives the deviation of the γ -ray energy from 4.44 MeV. The theoretical curves were normalized to the data.
16. γ -ray spectra calculated for various populations of the substrates for the 2^+ , 4.44 MeV level of ^{12}C assuming a $\sin^2 2 n\rightarrow\gamma$, where $n\rightarrow\gamma$ is the angle between the recoiling nucleus and the γ ray. In all cases $P_{+1} = P_{-1}$ or $P_{+2} = P_{-2}$ where $P_{\pm 1} = 0$ or $P_{\pm 2} = 0$ respectively.
17. Comparison of the Monte Carlo calculation with the data obtained for the 4.49 MeV level in ^{11}B . The error bar represents on statistical standard deviation. The proton distribution used was $|j_1(qR)|^2$ and the γ -rays were assumed isotropic.
18. Planar lithium drifted germanium detector, a is the highly conductive surface, b is the compensated, intrinsic region, and c is the uncompensated or dead region.
19. a shows a block diagram of a double delay line amplifier. Signals at points 1, 2, and 3 are shown in b. The abscissas of b is time while the ordinate shows the voltage at the indicated point.
20. Wave forms out of the preamplifier for detector inputs in which different fractions of the total charge was released in the dead region of the detector. Also shown (curves labeled IIA, IIIA, IVA) is difference in voltage between each dead region event and the corresponding intrinsic region event. The cross hatched area indicates the noise level of the fast amplifiers used.
21. a shows a block diagram of a proposed pulse shape discriminator. b gives the response for a good event and c for a bad event.

22. a gives a block diagram of the pulse shape discriminator actually constructed. b gives its wave forms for a good event and c for a bad event. d shows how the same circuit discriminate against pulse pileup.
23. Schematic diagram of the fast amplification stages of the pulse shape discriminator.
24. Schematic diagram of the discriminator section of the pulse shape and compensated timing discriminators.
25. Improvement in peak to background ratio as a result of pulse shape discrimination.
26. Charge sensitive feedback loop configuration.
27. Schematic diagram of the charge sensitive, FET preamplifier.
28. a shows the simple circuit used in analysis of timing compensation. b gives a typical, linearly rising input signal. The times and thresholds are explained in the text. c shows the wave forms at various points in the circuit and d is a block diagram of the completed compensated timing discriminator.
29. The timing circuit of a standard univibrator. The similarity between this circuit and that of Figure 28a should be noted.

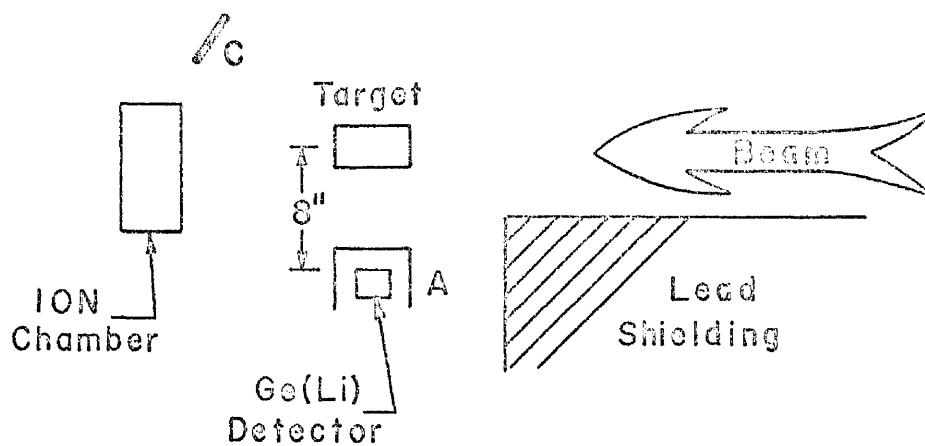


Figure 1

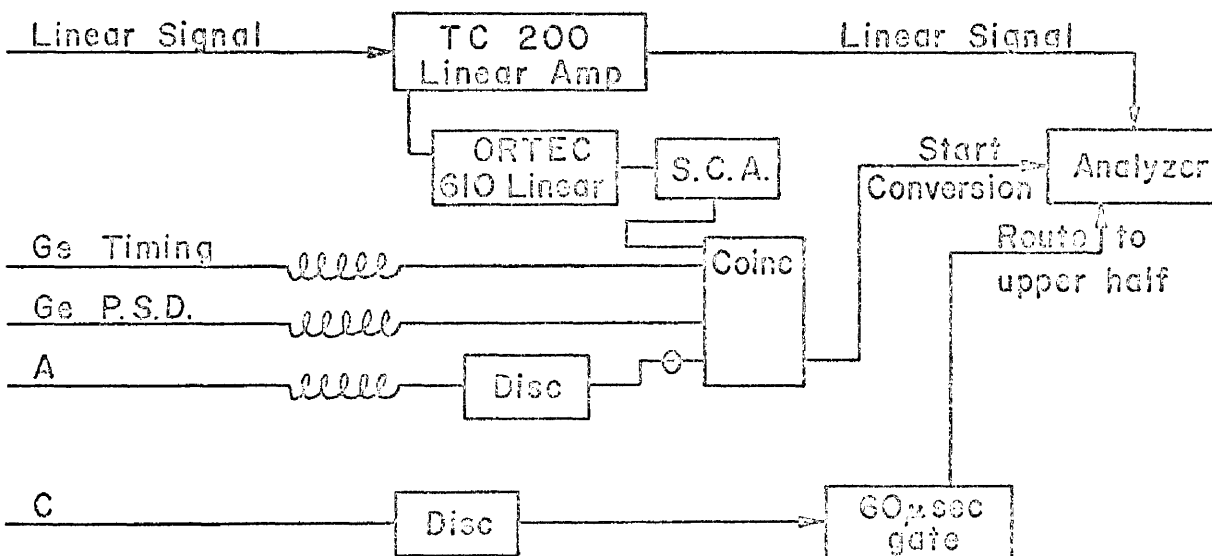


Figure 2

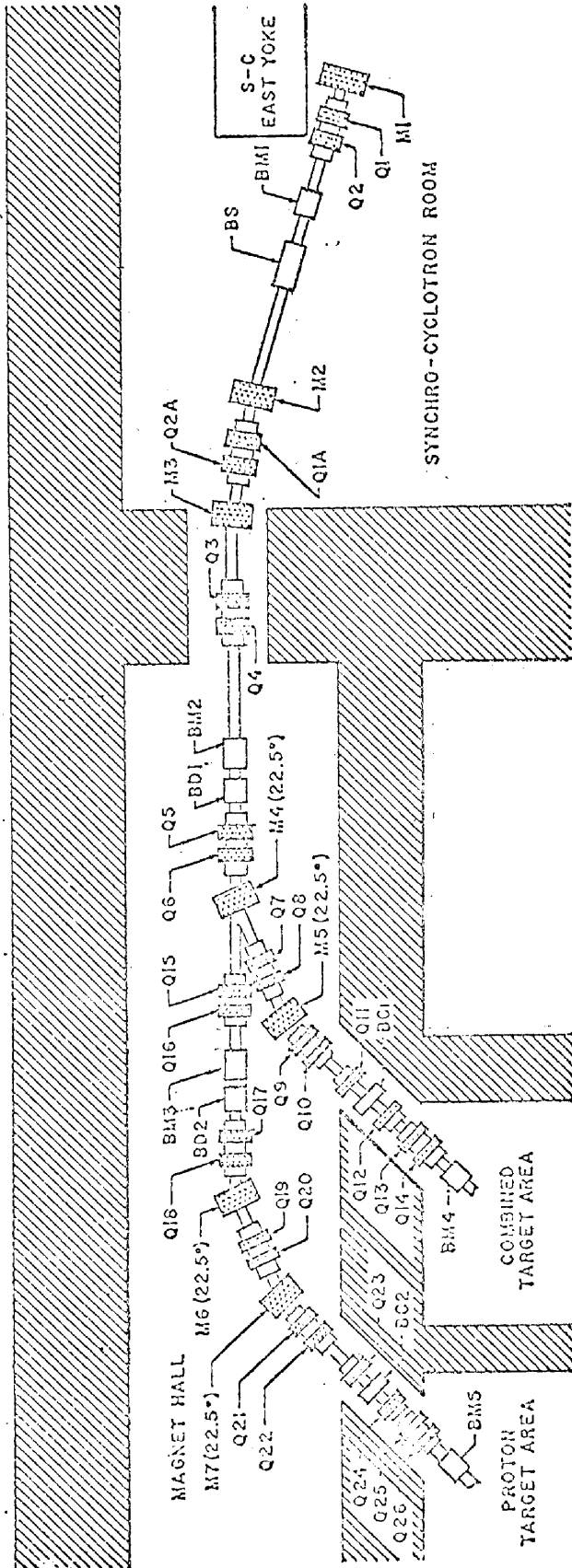


Figure 3

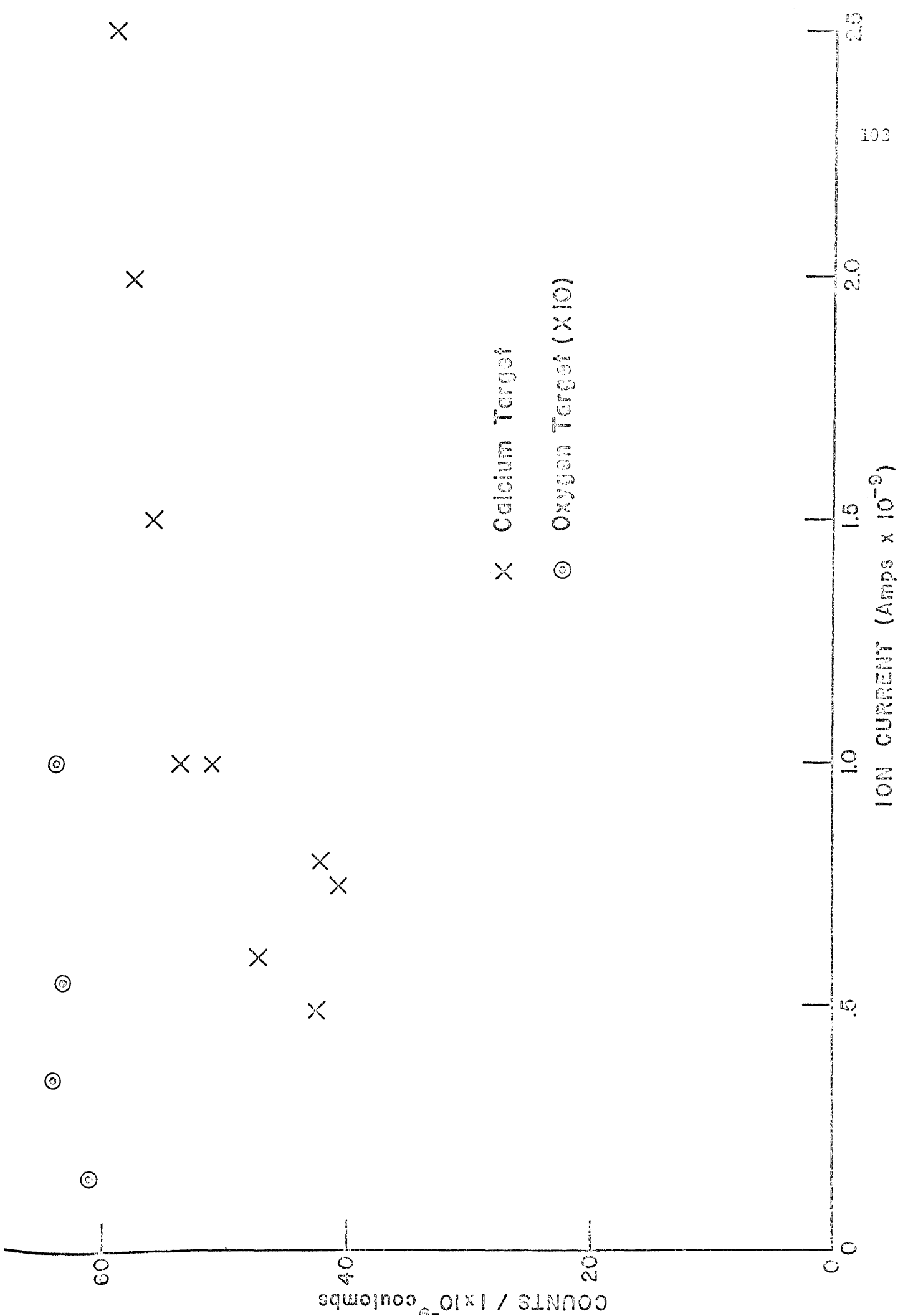
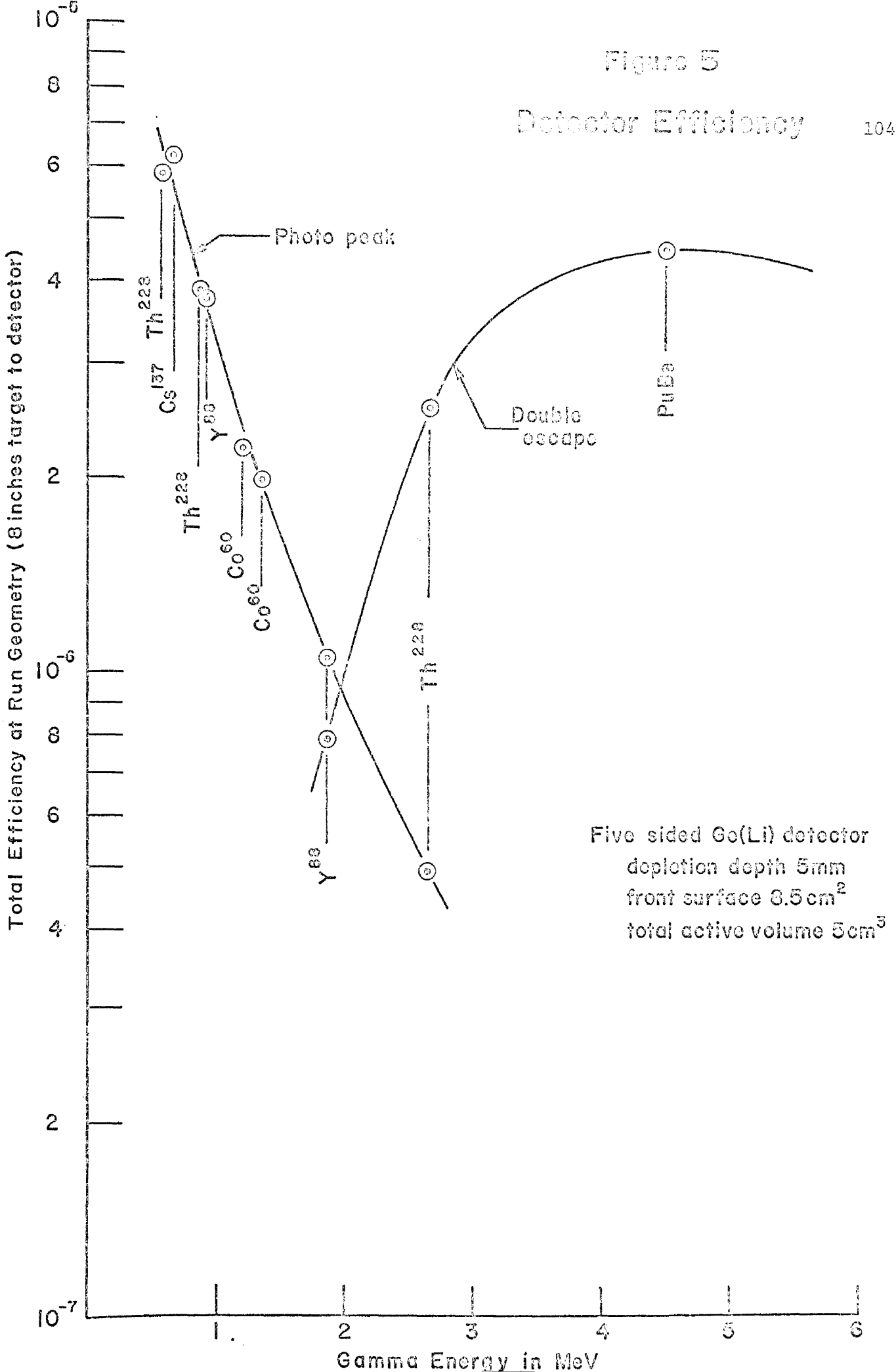


Figure 4

Figure 5

Detector Efficiency



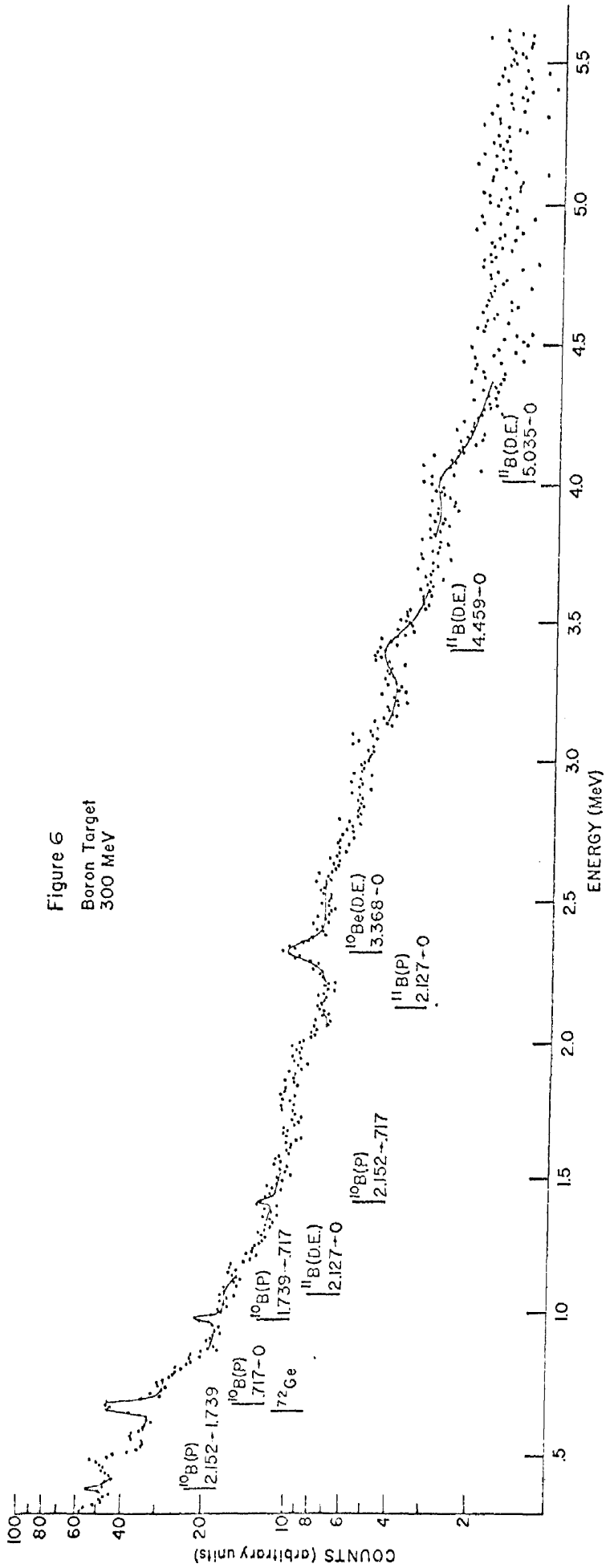
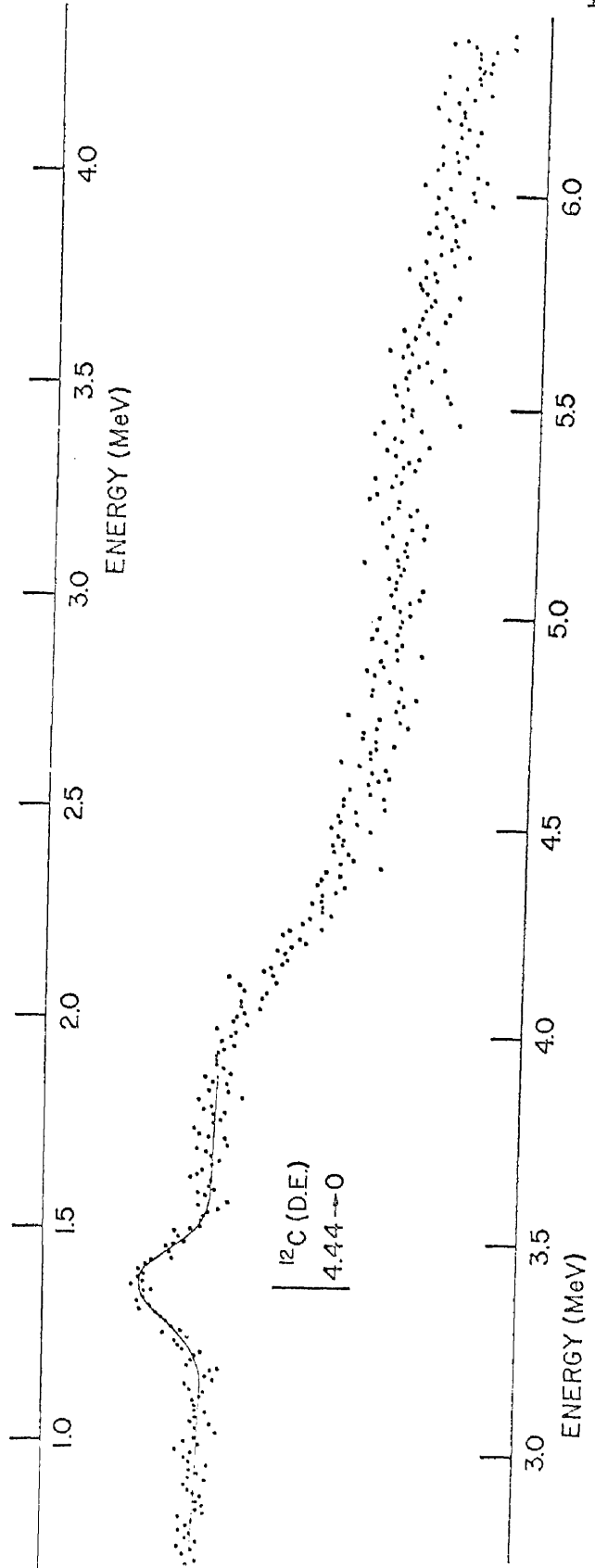
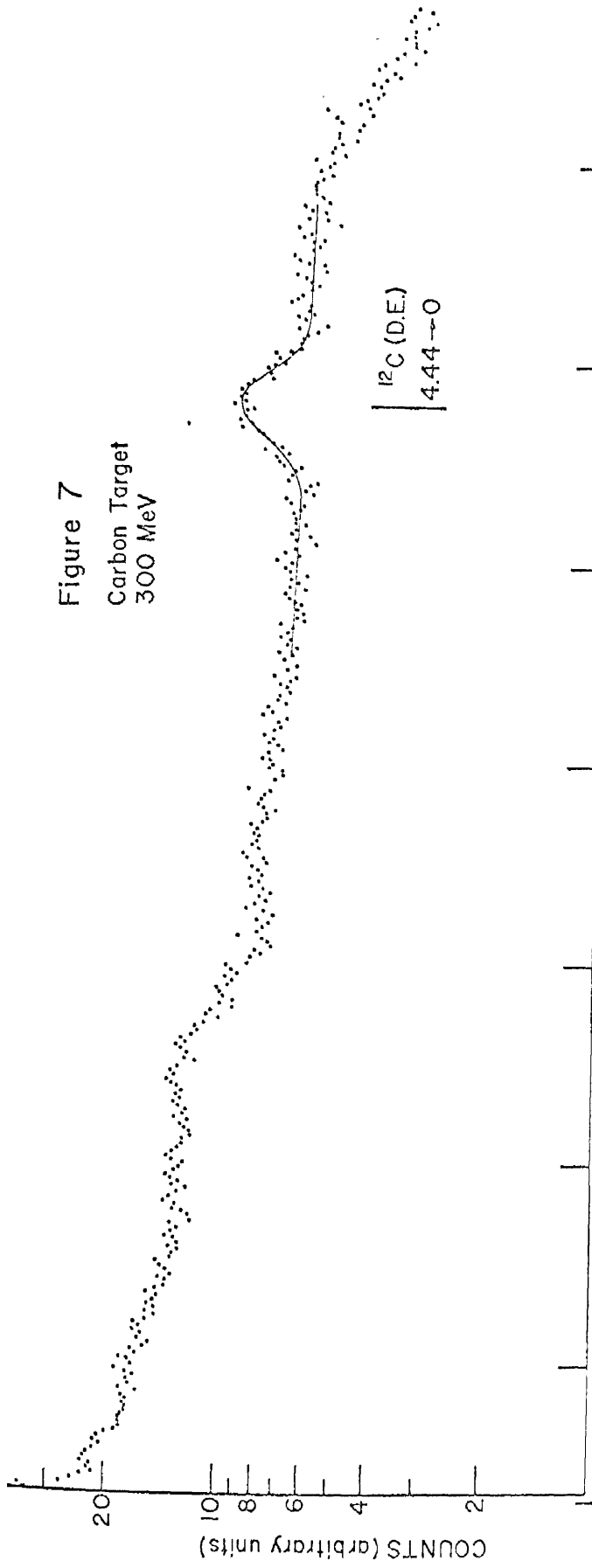
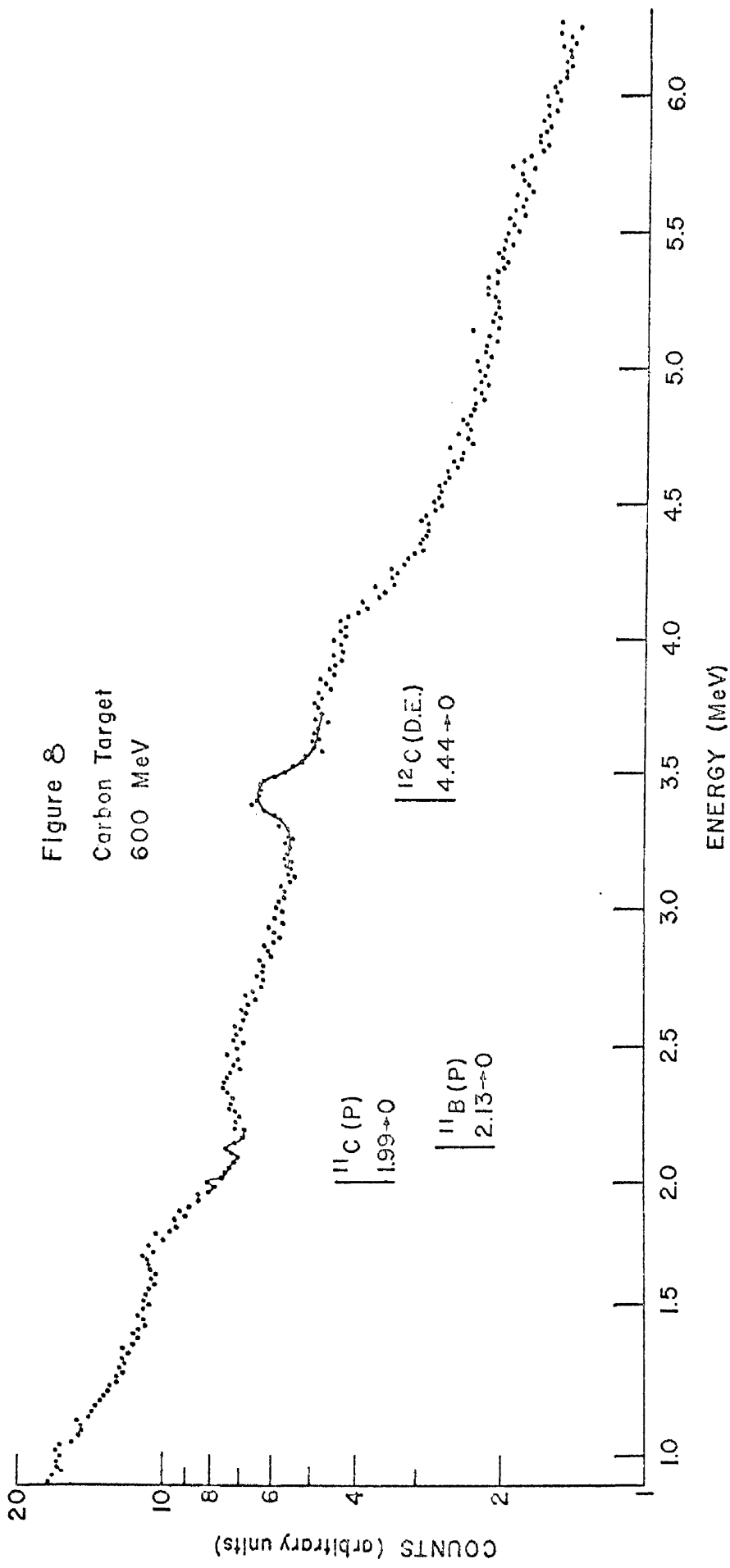
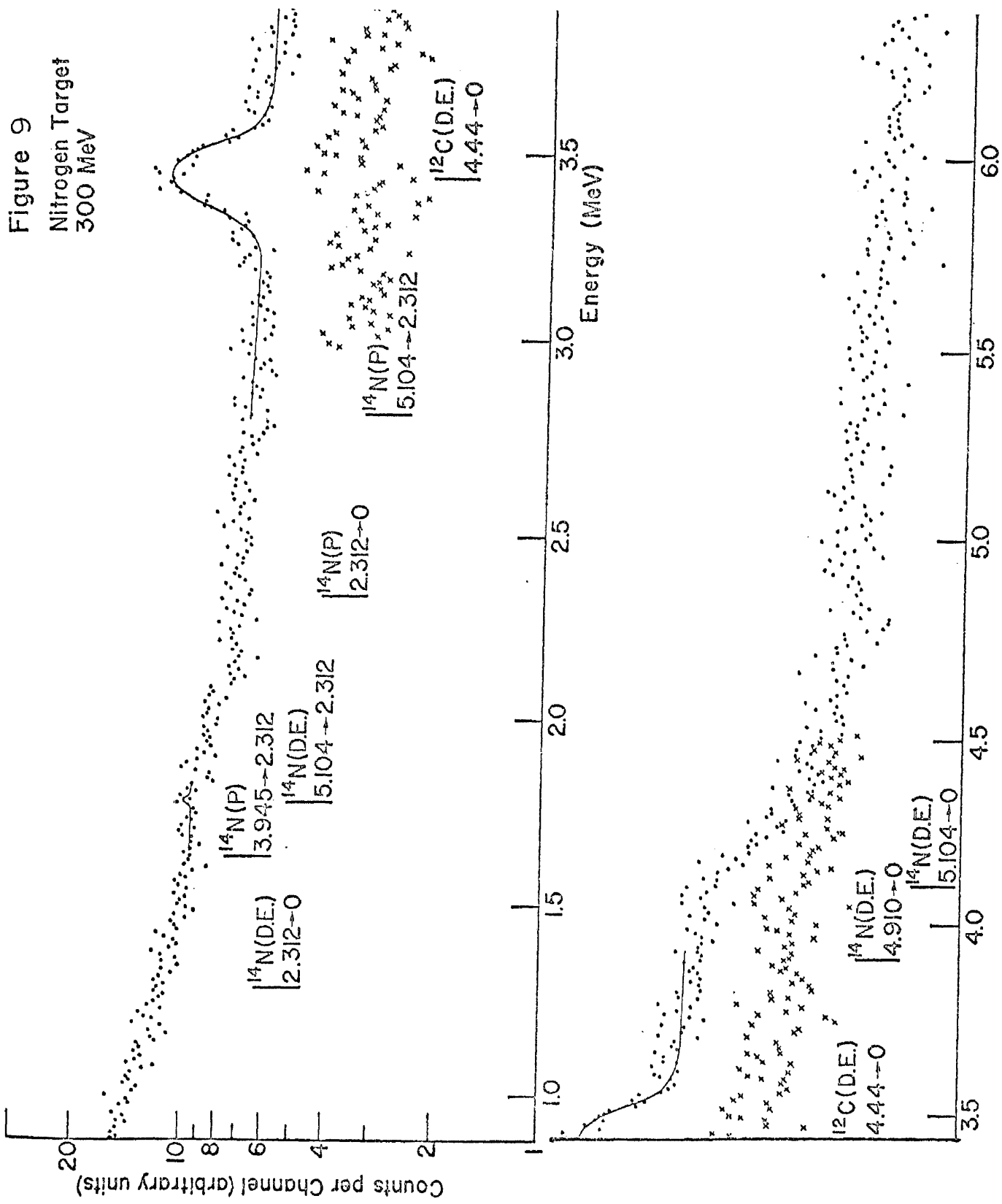


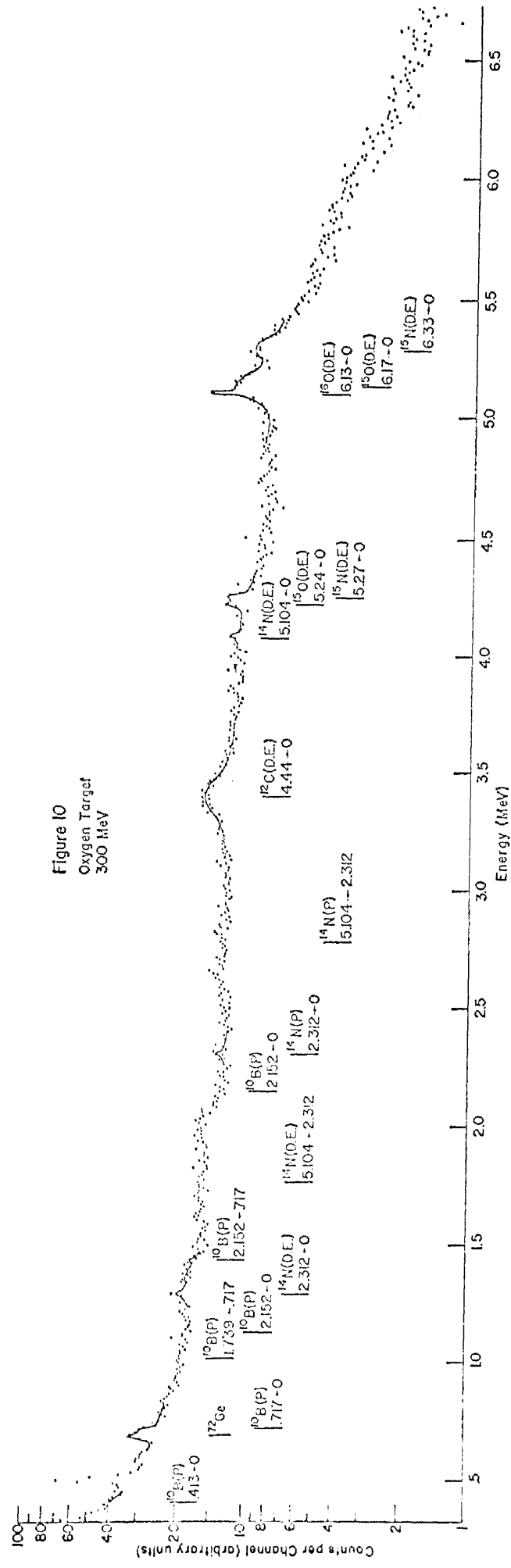
Figure 7

Carbon Target
300 MeV









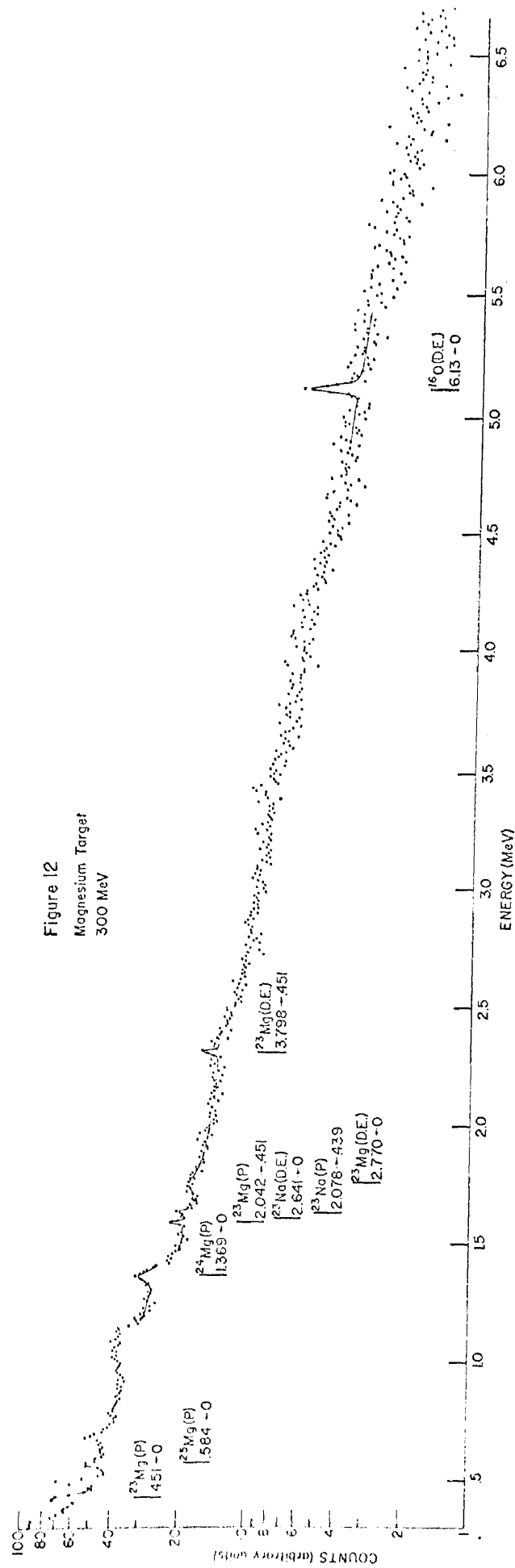
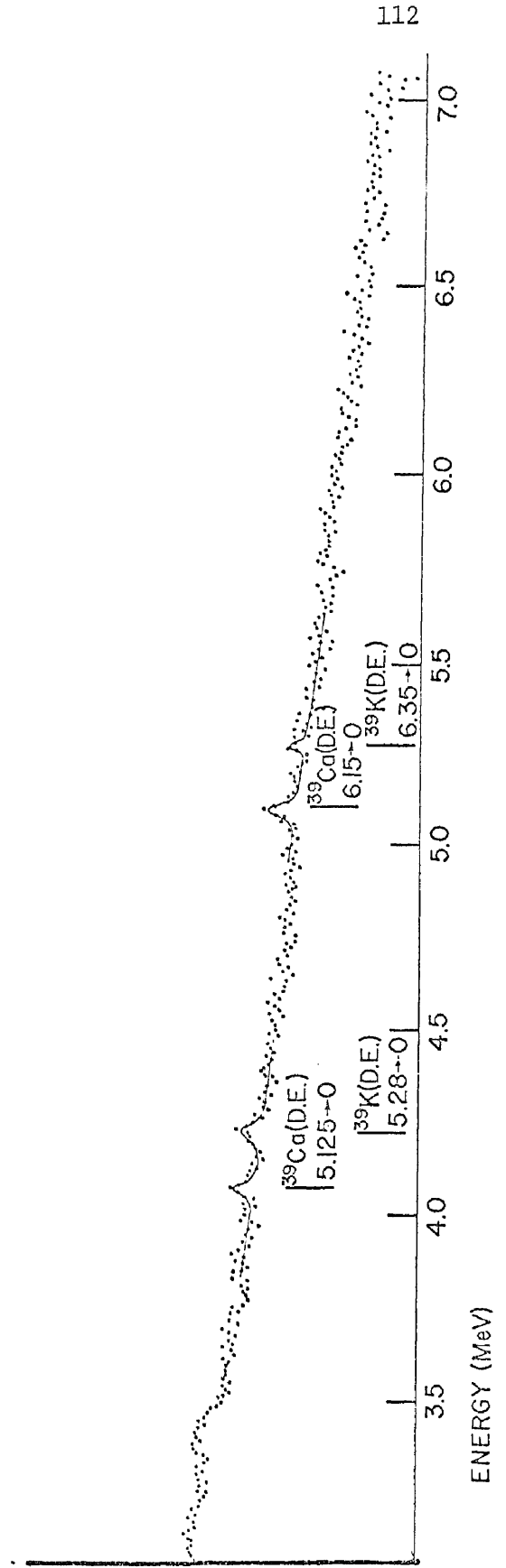
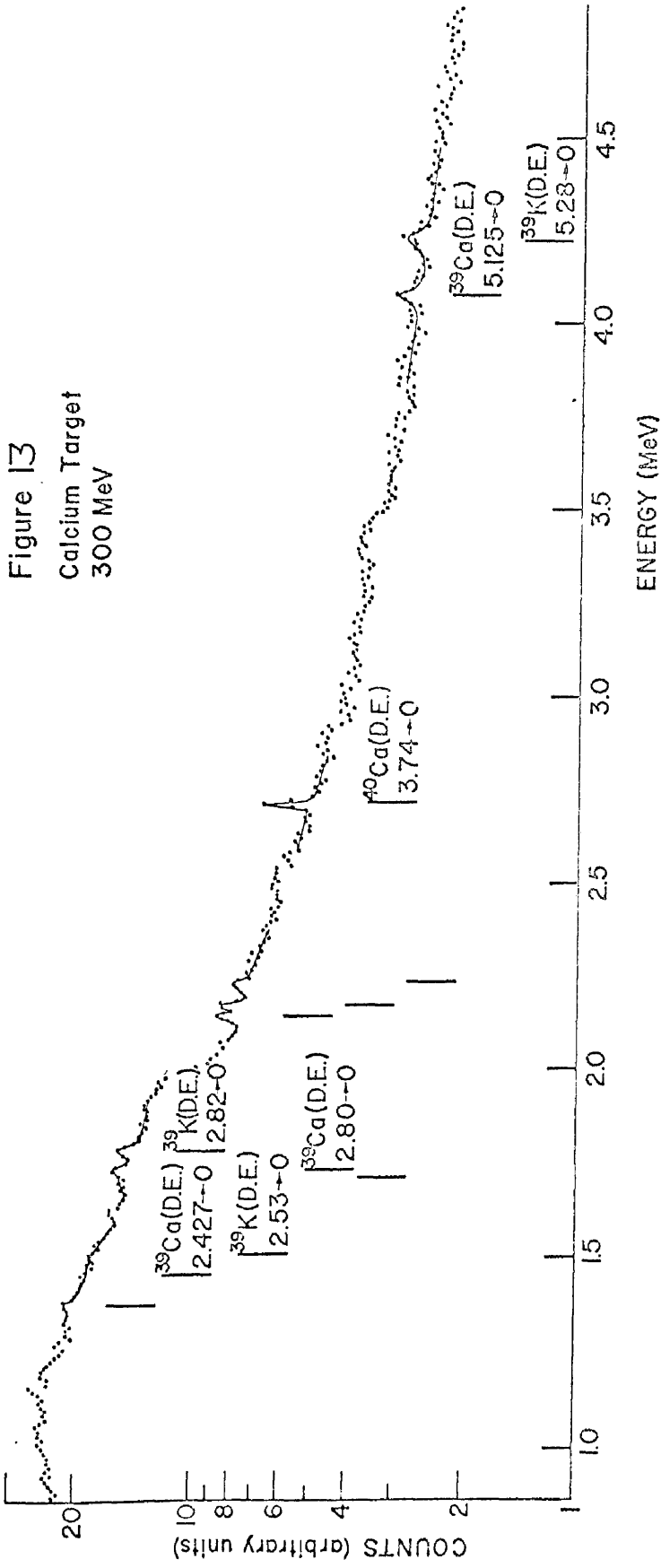


Figure 13

Calcium Target
300 MeV



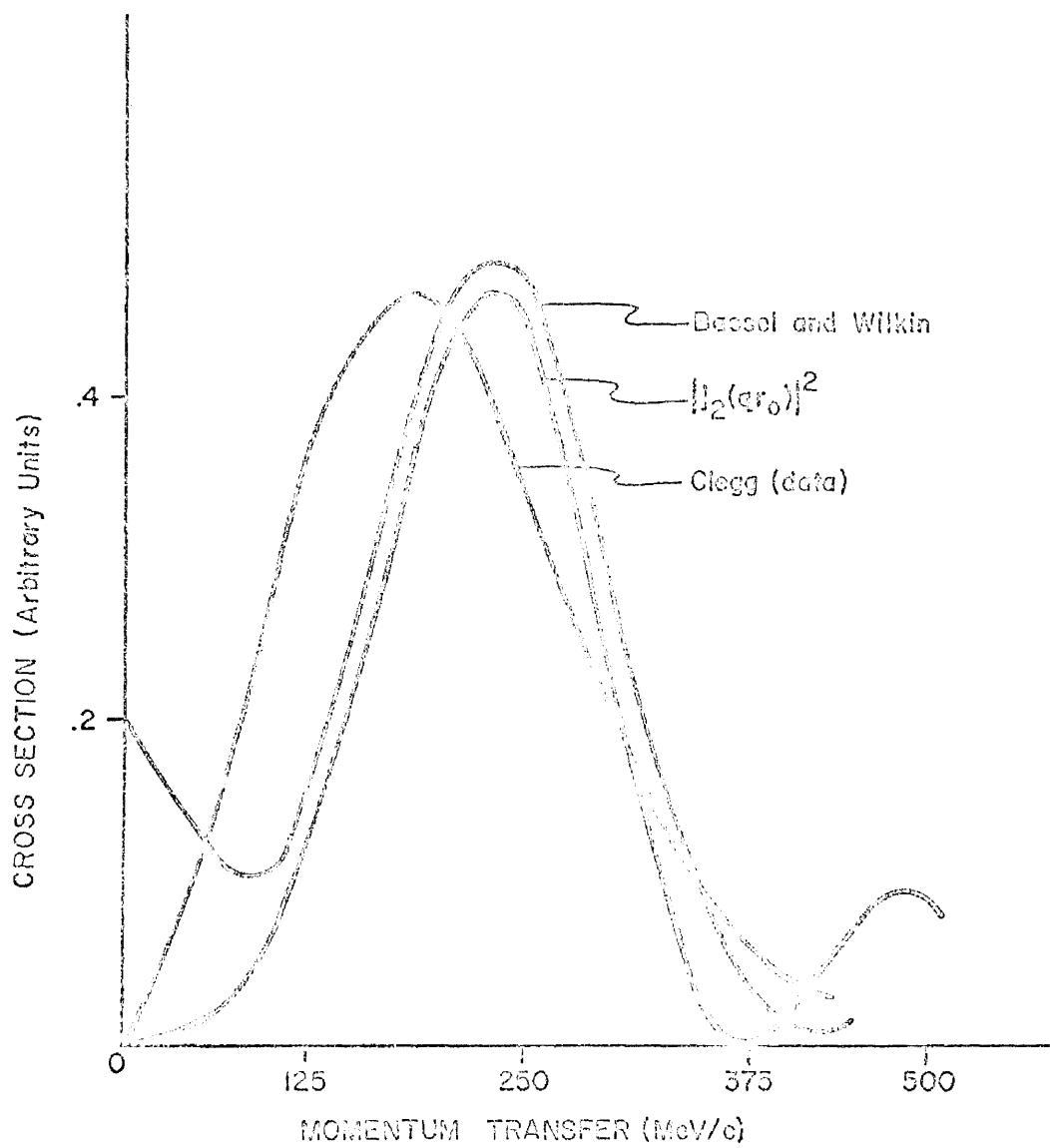
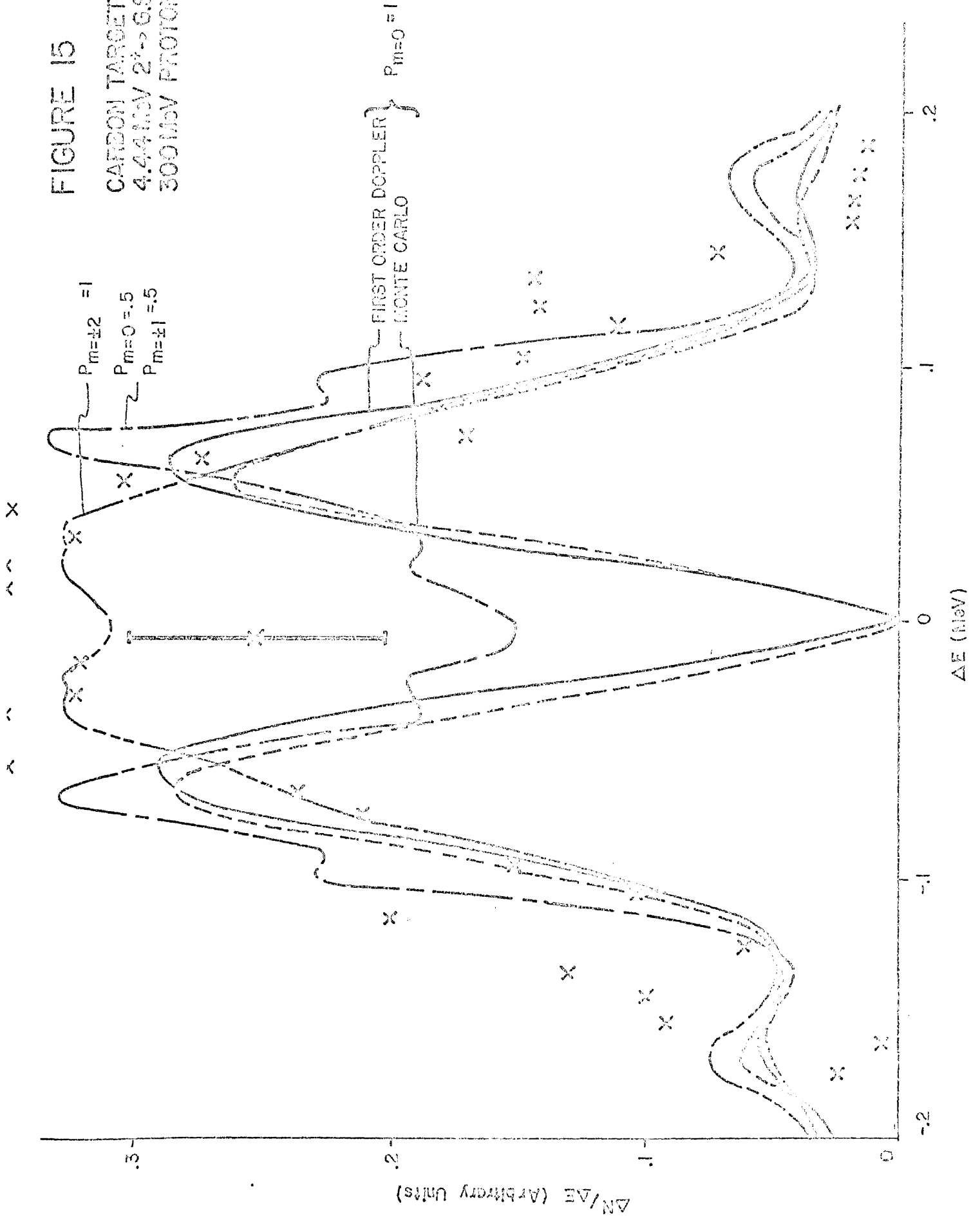


FIGURE 14

FIGURE 15

CARBON TARGET
4.44 MeV $2^+ \rightarrow 0^+$ G.S.
300 MeV PROTONS



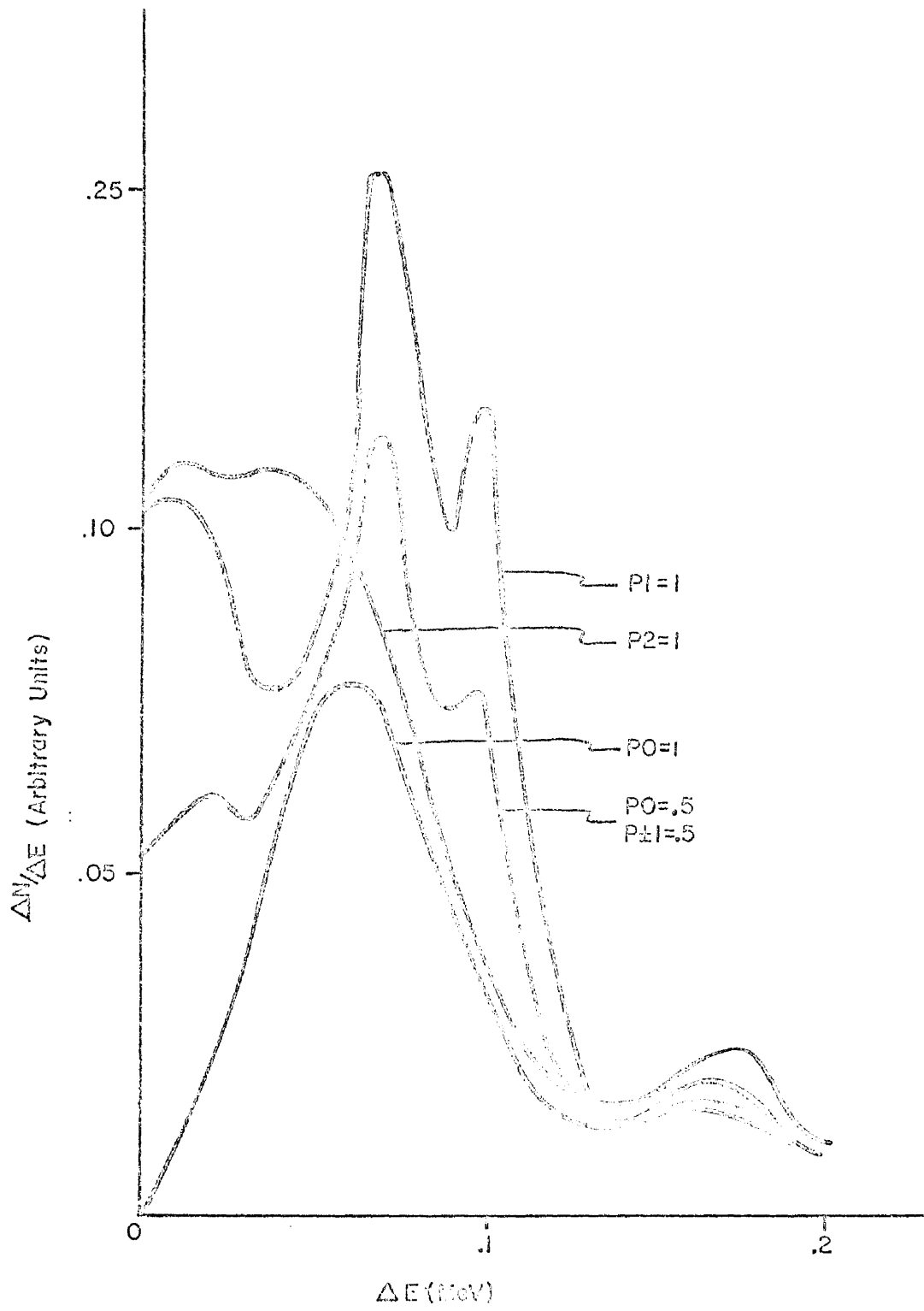
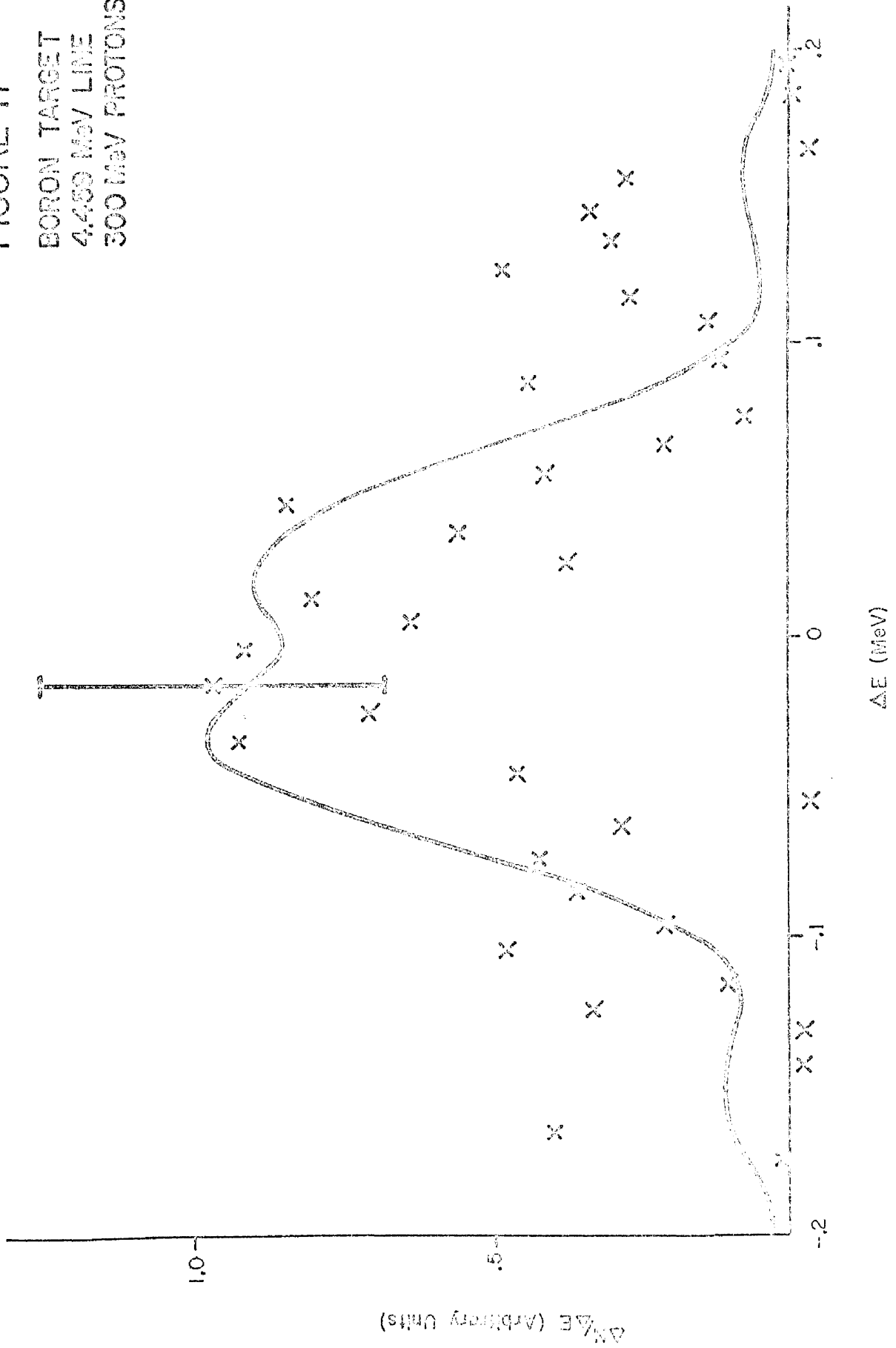
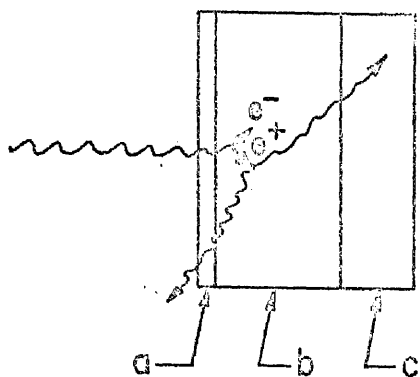


FIGURE 16

FIGURE 17
BORON TARGET
4.459 MeV LINE
300 MeV PROTONS





Bulk Properties
 $\mu \approx 6 \times 10^3 \frac{\text{cm}^2}{\text{V}\cdot\text{sec}}$
 $\xi \approx 39 \text{ cm}^2/\text{sec}$
 $\tau \approx 10^{-4} \text{ sec}$

$E \approx 1000 \text{ V/cm}$
 $W \approx 5 \text{ mm}$

Figure 18

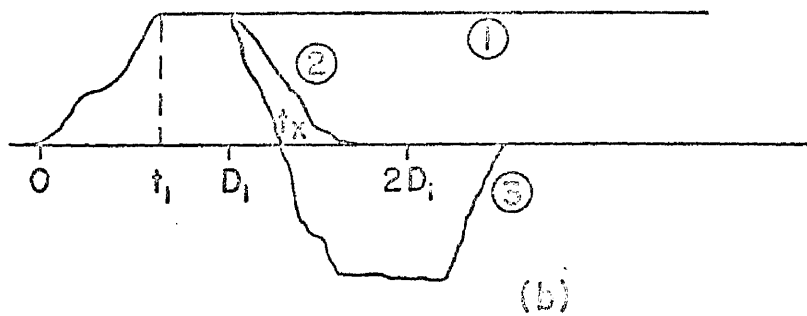
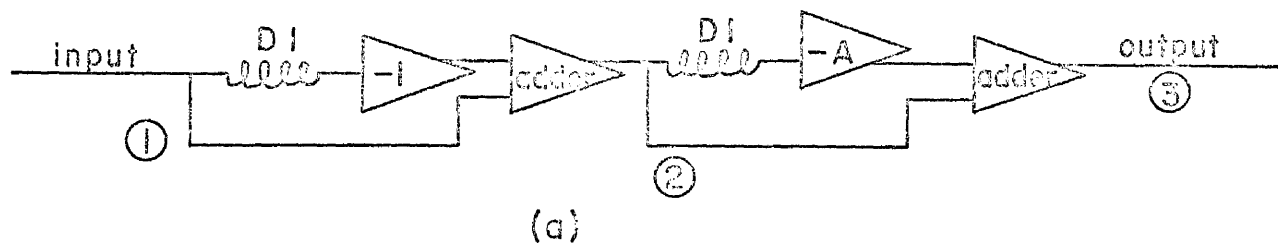


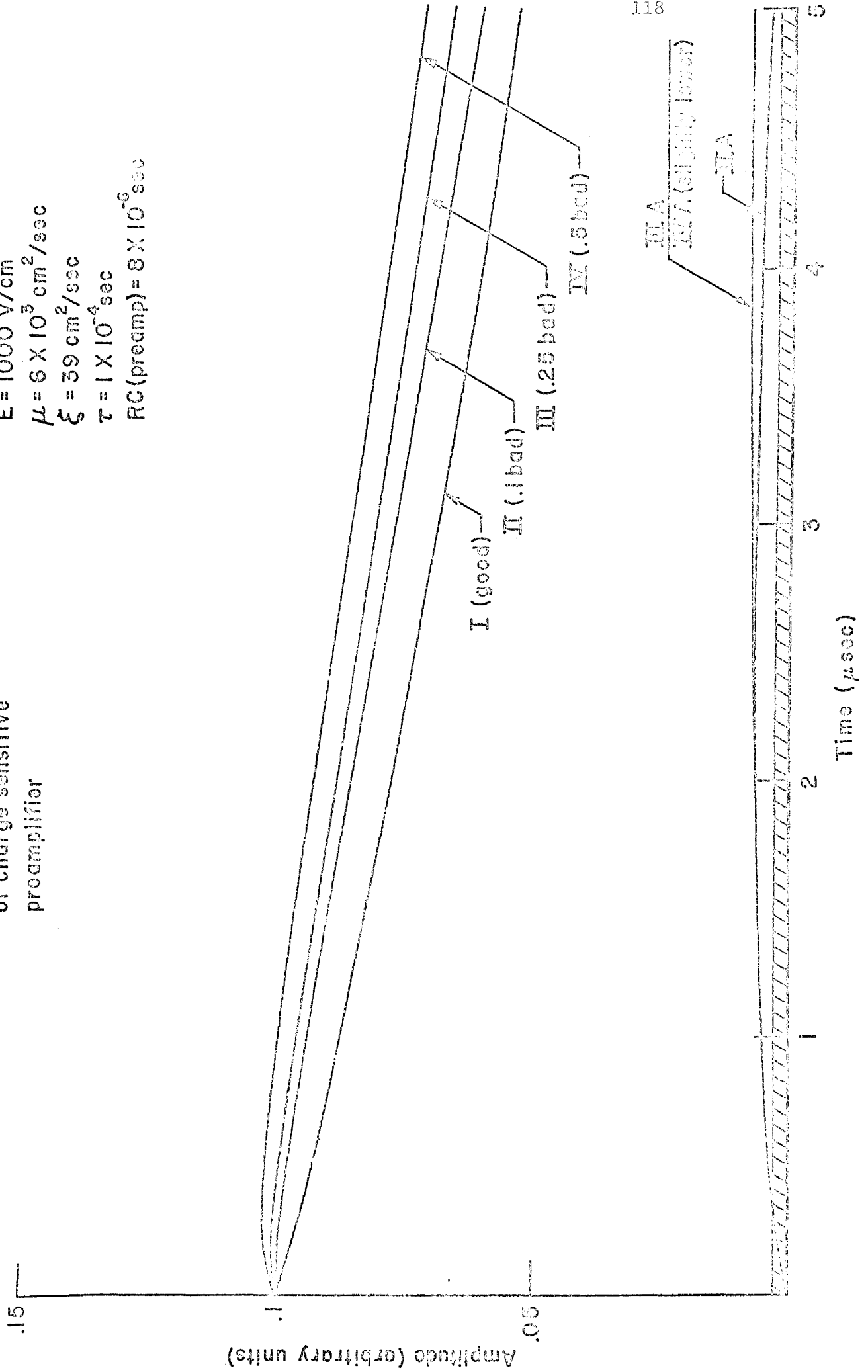
Figure 19

Figure 20

Voltage waveform out
of charge sensitive
preamplifier

Detector Properties

- $E = 1000 \text{ V/cm}$
- $\mu = 6 \times 10^3 \text{ cm}^2/\text{sec}$
- $\xi = 39 \text{ cm}^2/\text{sec}$
- $\tau = 1 \times 10^{-4} \text{ sec}$
- $RC(\text{preamp}) = 8 \times 10^{-6} \text{ sec}$



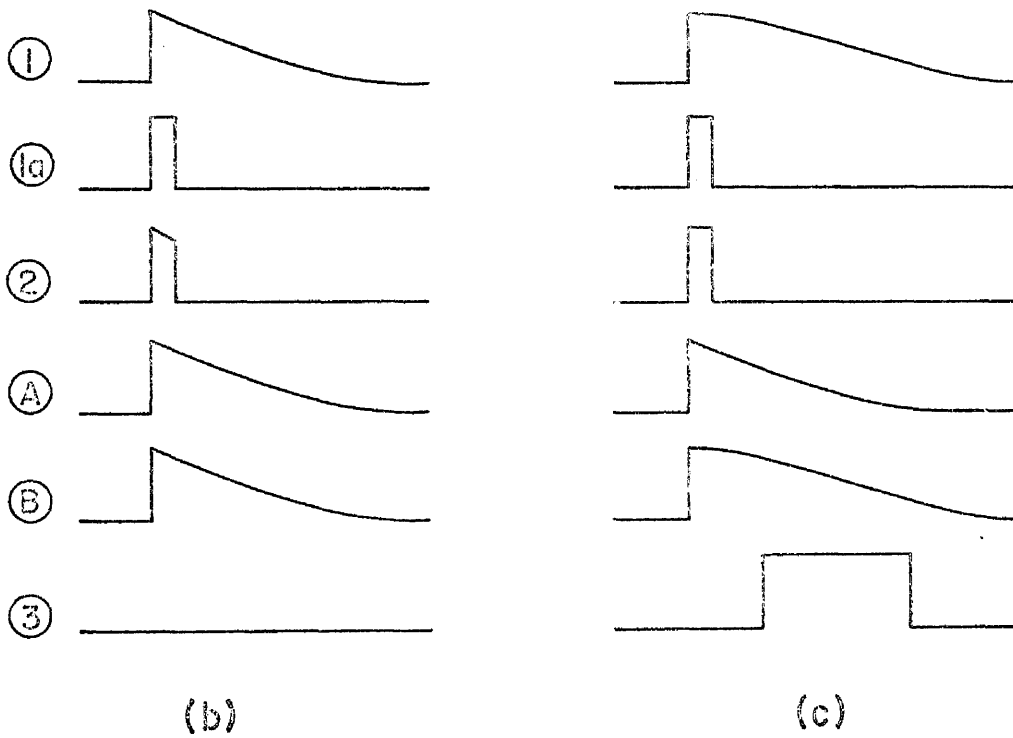
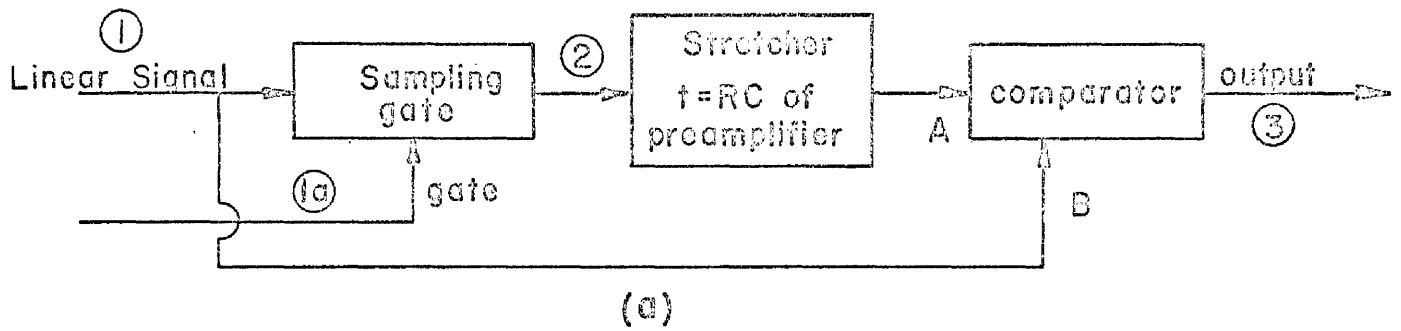
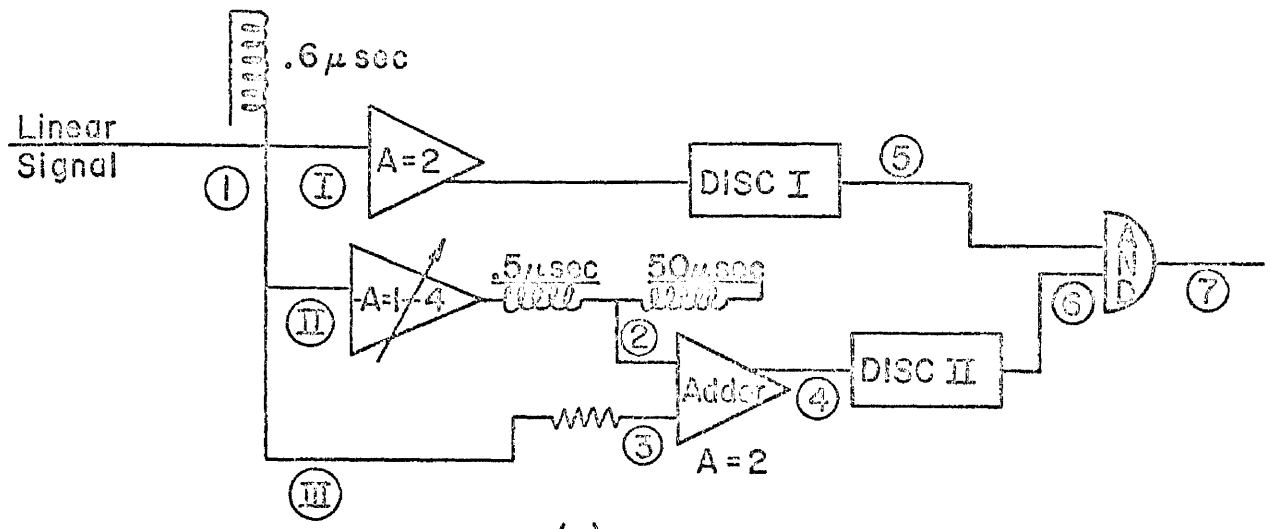
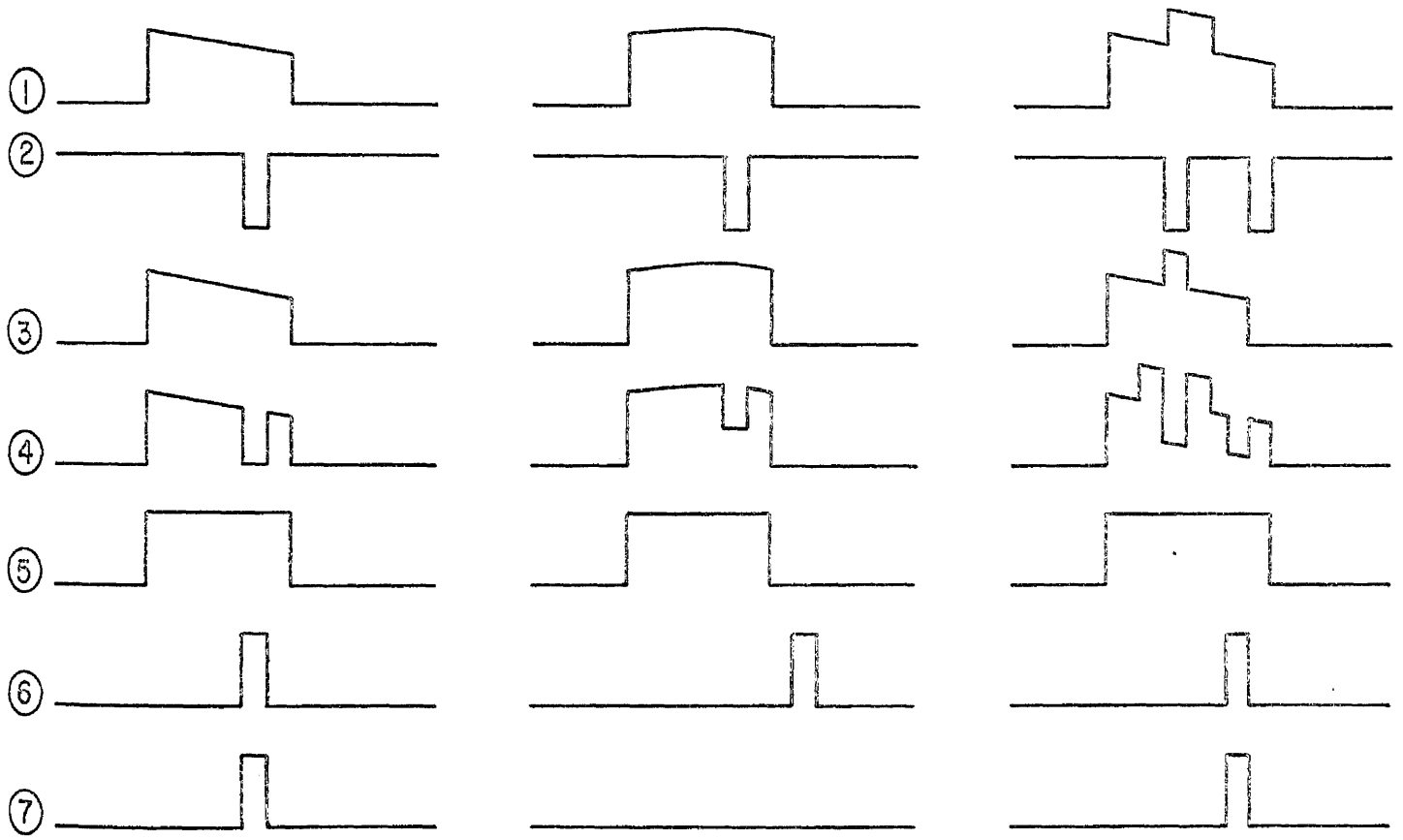


Figure 21



(a)



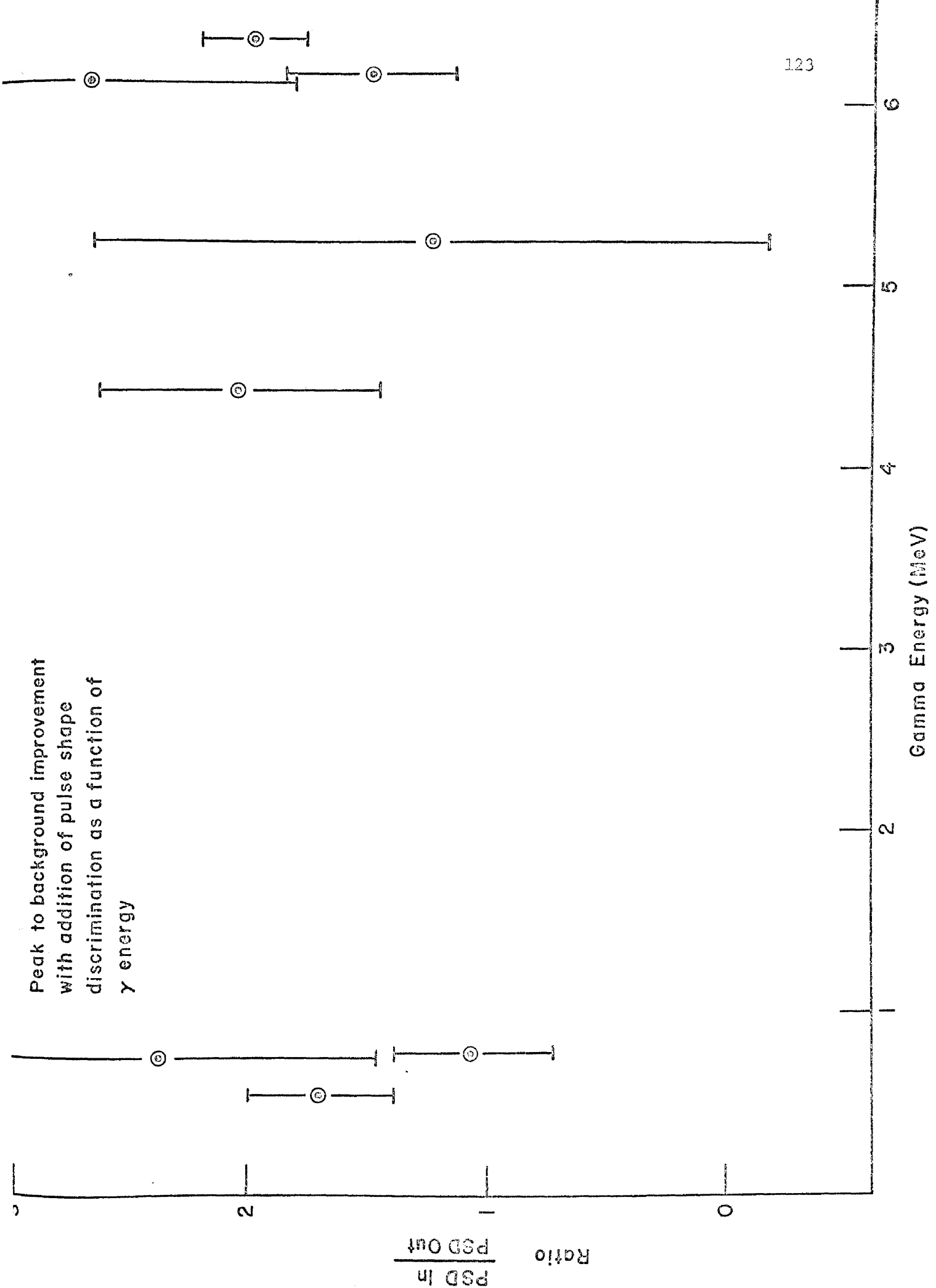
(b)

(c)

(d)

Figure 22

Peak to background improvement
with addition of pulse shape
discrimination as a function of
 γ energy



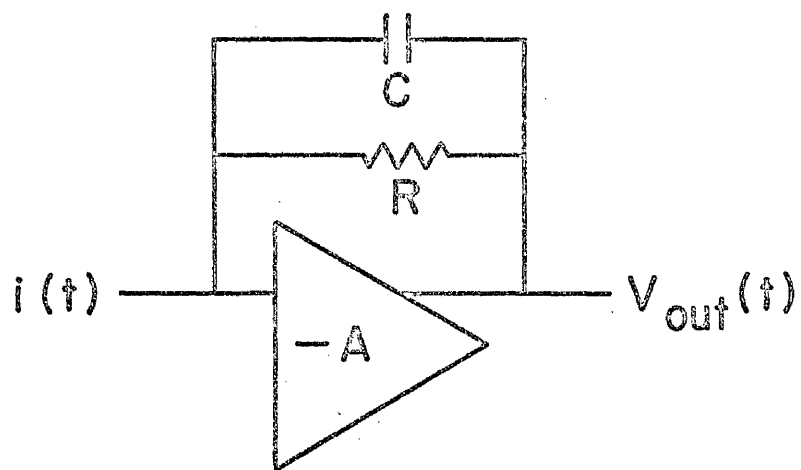
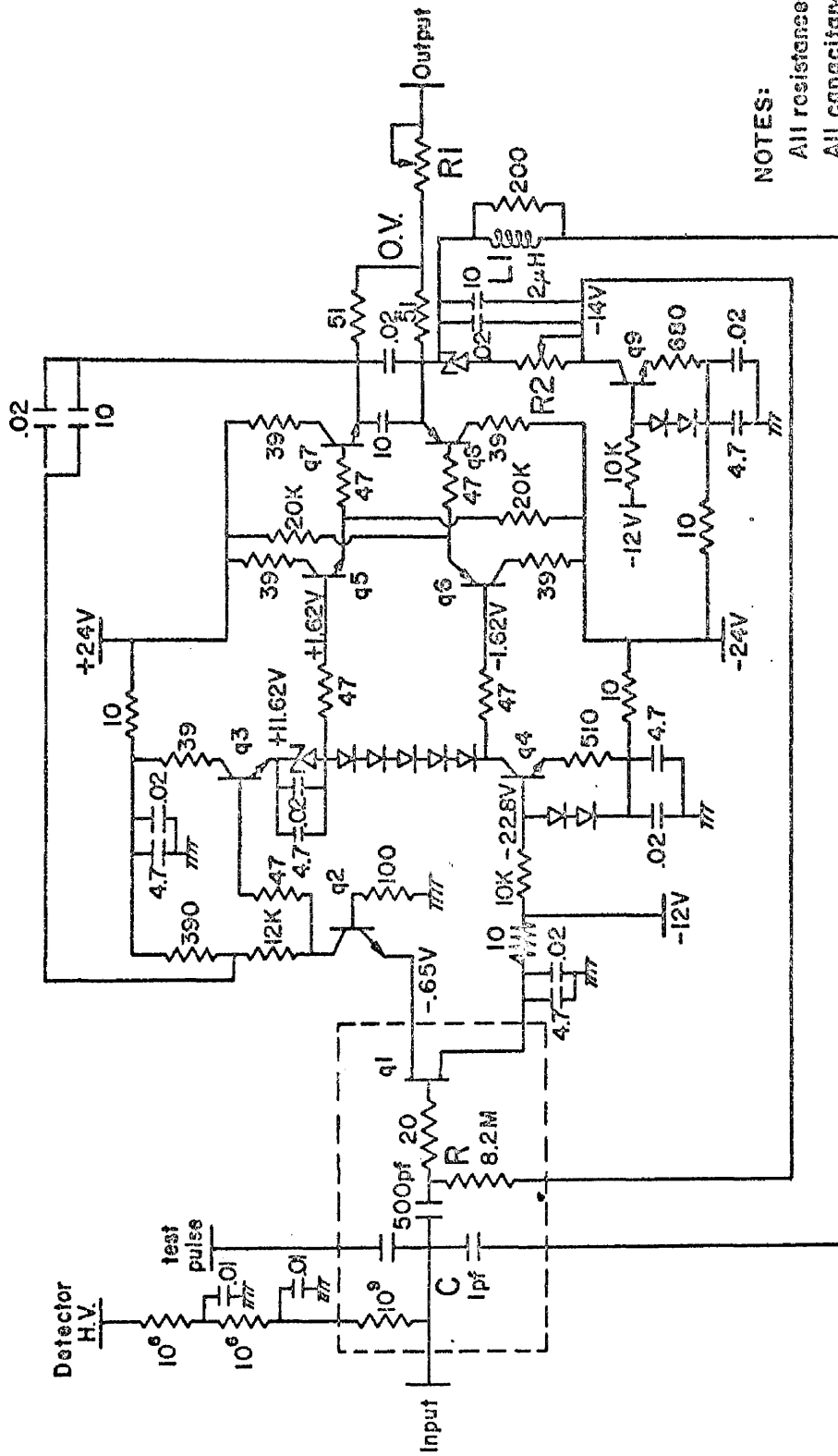


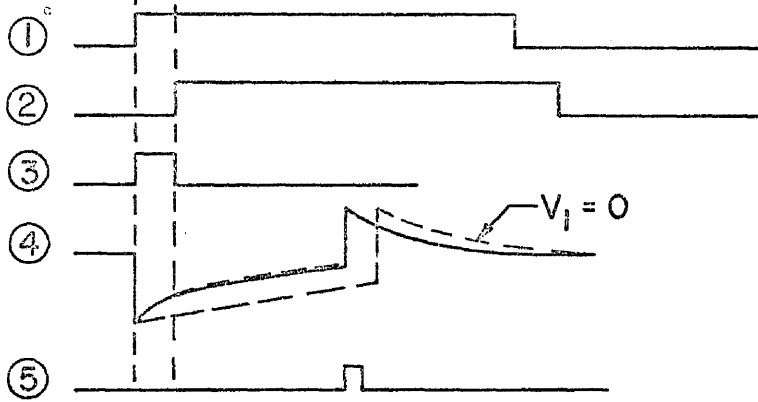
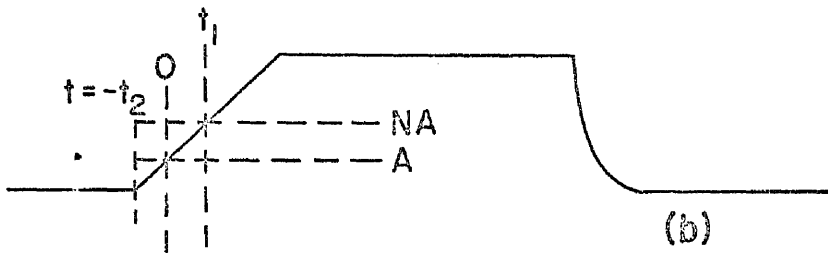
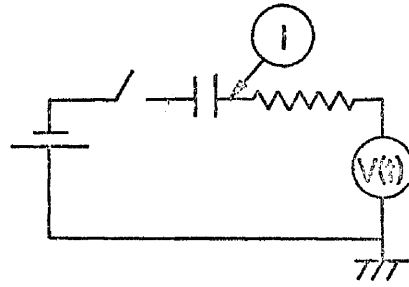
Figure 26



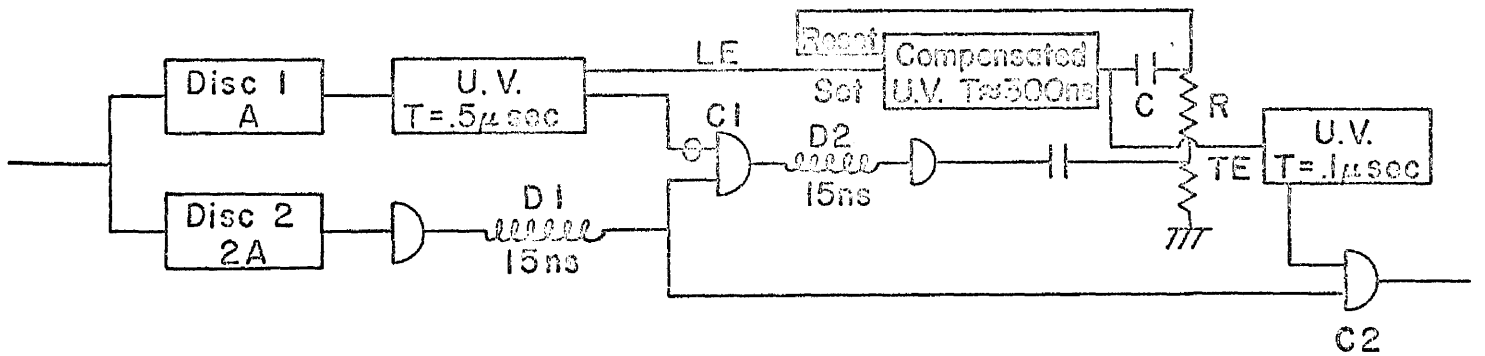
NOTES:

- All resistances in ohms.
- All capacitance in mfd unless noted.
- q1 → T1S42.
- q2, q3 → 2N4252.
- All others 2N3504 or 2N3503.
- Diodes silicon 1N914.

Figure 27



(c)



(d)

Figure 28

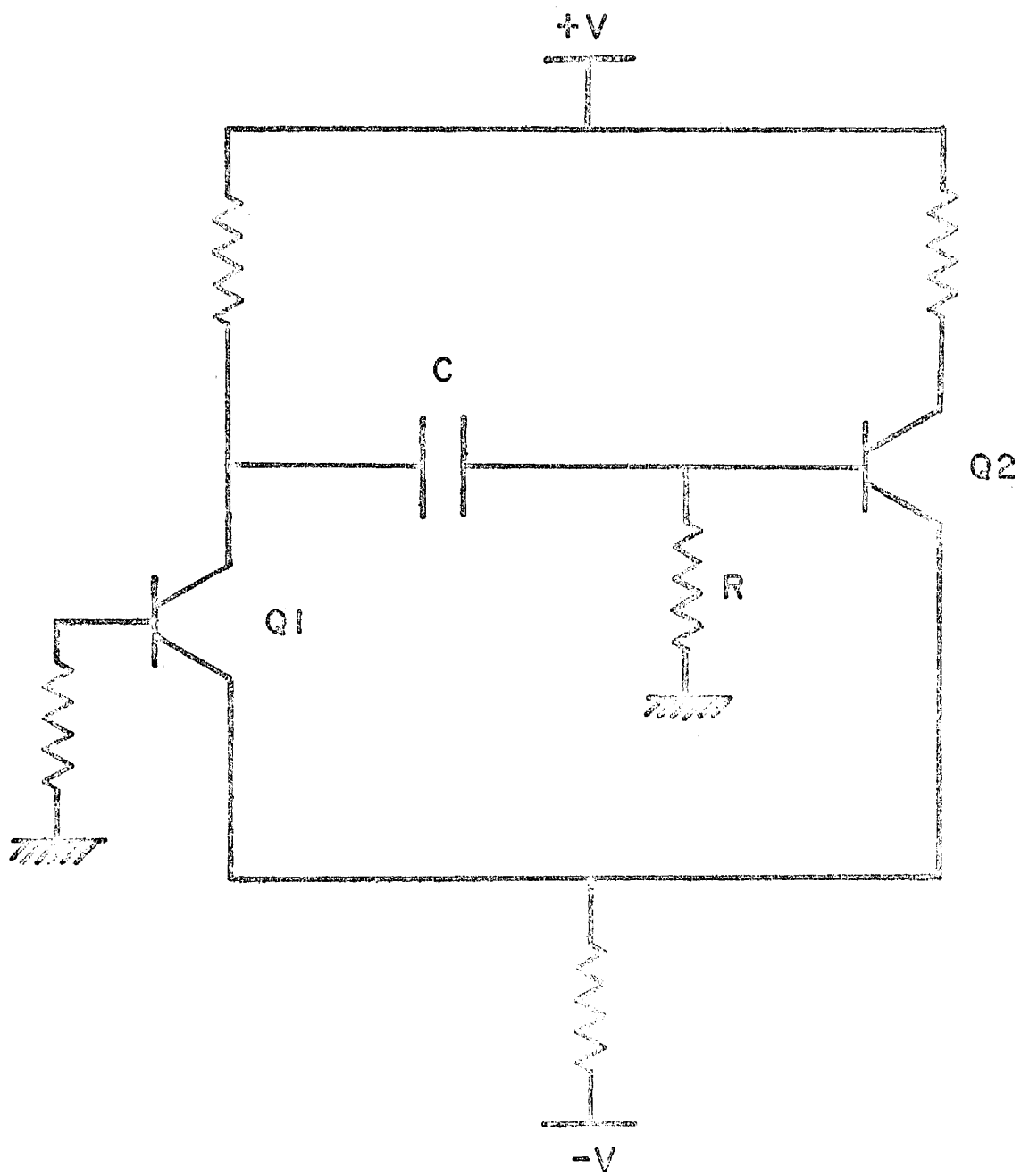


FIGURE 29

APPENDIX C

The use of lithium drifted germanium detectors for high energy γ -ray spectroscopy results in some special problems. This is because the path length of the ionizing particle(s) (e^- (and e^+)), which is of the order of one mm for a 1 MeV electron, becomes an appreciable fraction of the sensitive depth ($\approx 5\text{mm}$) of the detector. When the ionizing particle exits from the sensitive volume, energy determination is no longer insured. The behaviour of the detector under these conditions, however, lends itself well to discrimination methods. This appendix will give the physical basis for the γ -ray interaction and describe the method of discrimination used in this experiment to minimize the effects of events in which some of the energy information was lost. Appendix D gives the details of a preamplifier necessary to allow this discrimination.

The construction of a simple planar detector^{56, 57, 58} is shown in Figure 18. The γ -ray interacts in the germanium via photo-electric absorption, Compton scattering, or pair production. The energy of the initial γ ray is thus related to the kinetic energy of the electron created in the interaction (total energy of the electron-positron pair in the case of pair production). These ionizing particles then lose their energy by the generation of electron-hole (eh) pairs in the germanium. For accurate energy

determination, all these eh pairs must be collected and delivered to the external circuitry for integration. The detector is divided into three principle regions which are:

1. A highly doped, highly conductive front surface (a in Figure 18).
2. A junction region in which the carries have been compensated by the lithium-drift procedure (b in Figure 18); this process ideally gives the junction region the conductive properties of pure, intrinsic germanium.
3. An uncompensated region of P-type germanium (c in Figure 18).

In operation a high reverse bias is applied across the junction region to collect the eh pairs created by the interaction. This field appears across the intrinsic region (see 2 above). In practice the highly doped region (see 1 above) is made as thin as possible and it will be ignored in the remainder of this discussion.

The eh pairs created in the junction region are thus swept out in a time given by

$$t_i = W/\mu E \quad C(1)$$

where: μ is the carrier mobility,

W is the thickness of the junction region, and

E is the electric field.

For a detector operated at 1000 V/cm, with a depletion depth of 5mm, and a carrier mobility of 3×10^4 cm²/Vsec, $t_i = 17$ nsec.

However, if carriers are created in the nondepleted region (see 3 above) they must diffuse to the junction region to be collected.

This process is much slower, being given by

$$t_n = d^2/\xi \quad C(2)$$

where: ξ is the diffusion constant, and

d is the diffusion length.

For a mean diffusion length of 1mm and diffusion constant of $39 \frac{\text{cm}^2}{\text{sec}}$,

$$t_n = 250 \text{ } \mu\text{sec.}$$

This difference in collection times for the two regions will yield a corresponding difference in pulse shape, i.e., an interaction which occurs solely in the intrinsic region will have all the eh pairs collected in a very short time and will thus be a "good" event while an interaction which has some or all of the eh pairs created in the nondepleted region will have a slowly collected component. This slow component is undesirable for two reasons:

1. Since the diffusion time is of the same order of magnitude as the minority carrier lifetime in germanium, some of the eh pairs will be lost to trapping centers and by recombination.

2. Subsequent band-passing stages of amplification (which must have clipping times $\approx 1 \mu\text{sec}$ in order to sustain the required instantaneous counting rate) will remove the slow component and the linear signal will thus not be simply related to the energy of the original γ ray.

In order to study these points in more detail, the charge

distribution from a Ge(Li) detector for a γ ray which interacted in the nondepleted region was put into the response equation for a charge sensitive preamplifier and the resulting equation was integrated to yield the voltage signal out of the preamplifier. The assumptions made in this calculation were:

1. the charge collection time in the junction region is negligible,
2. the diffusion component will be considered in one dimension only, that is, the eh pairs will be assumed to diffuse along the path of the ionizing particle (which is the direction of the electric field) back to the depleted region, and
3. dE/dx for the ionizing particle is constant.

The first assumption need not be considered since we are looking for effects with times $\approx \mu\text{sec}$; however, the second emphasizes the contribution from nondepletion carriers. With these assumptions, the charge distribution for nondepletion region pairs is given by the current which flows over the boundary between the depleted and nondepleted regions.

$$i_n(t) = \frac{dq}{dt} = \frac{dq}{dx} \frac{dx}{dt}$$

$$i_n(t) = \frac{dq}{dx} e^{-t/\tau} \frac{1}{2} \sqrt{\xi/t} \quad C(3)$$

where: ξ is the diffusion constant for germanium and

τ is the lifetime of the minority carriers in germanium.

The exponential factor is to account for loss of carriers on trapping

centers and through recombination.

From Appendix D, the voltage signal out of the charge sensitive preamplifier for an input current source $i(t)$ is given by

$$V_p(t) = -\frac{e^{-t/RC}}{C} \int_0^t i(t') e^{t'/RC} dt' \quad D(1)$$

where: RC is the time constant of the preamplifier,

R is the preamplifier feedback resistance, and

C is the preamplifier feedback capacitance.

This equation is for the feedback loop of Figure 26. Putting $i(t)$ from C(3) into equation D(1) gives

$$V_p(t) = -\frac{e^{-t/RC}}{C} \int_0^t \frac{1}{2} \frac{dq}{dx} \sqrt{\xi/t'} e^{t'/RC} e^{-t/\tau} dt' \quad C(4)$$

Equation C(4) was integrated numerically to obtain the voltage waveforms out of the preamplifier. The results of this integration are shown in Figure 20 which gives a set of curves for difference amounts of charge being released in the nondepleted region of the detector. The parameters of the preamplifier and detector used in the calculation are shown in the figure. For comparison, the curves have been normalized to the same initial amplitude, i.e., the 50 per cent curve (labeled IV) has been multiplied by 2, the 25 per cent curve (labeled III) by 4/3, et cetera. The acceptability of each pulse is indicated by the difference between it and the pulse from a similar interaction which occurred totally in the depleted region. These differences are shown in Figure 20 as IIA, IIIA, and IVA. That is

$$IIA = II - I,$$

signals for a "good" and a "bad" event, respectively.

The method of pulse shape discrimination used in this experiment is a modification of the system first used by Tamm, et al.⁵⁹ in which the initial amplitude is compared to the later amplitude at a specific time. A block diagram of this system is shown in Figure 22a. The preamplifier output signal is clipped to 600 ns to allow high count rates and is then divided to three paths. In path II the signal is delayed and clipped a second time to a width of 50 nsec. The amplitude of this signal is an indication of the initial charge collected by the detector. This delayed and inverted signal is added to the preamplifier signal in path III. Proper adjustment of the gain in path II will cause the output of the adder to follow the input for the first .5 μ sec and then return to the baseline at .5 to .6 μ sec for a "good" event; in contrast, for a "bad" event, the output of the adder will remain above the baseline for the duration of the input pulse. This adjustment of the linear portion of the pulse shape discriminator made the circuit independent of input pulse amplitude (assuming perfect linearity in paths II and III); however, it also puts severe restrictions on the behaviour of the discriminator which follows the adder. This discriminator was operated as a bi-stable device with its threshold and hysteresis adjusted so that it triggered just above the system noise level and reset at the baseline. This adjustment of the system was the principal improvement over the original design of Tamm, et al.

The reset transition of the discriminator is thus used to discriminate events. For a good event, the time of reset comes .5 μ sec after the beginning of the pulse. This time correlation is assured by the discriminator in path I which opens the final "and" circuit for the duration of the input pulse thus rejecting those signals in which the reset occurs at the end of the input signal. The waveforms for a "good" and "bad" pulse are shown in Figure 22b and c, respectively.

The complete schematic diagram of the unit is shown in Figures 23 and 24. The linear stages were based on circuits by Millard.⁶⁰ The discriminators were tunnel diode units due to Huam and Smedsdal.⁶¹ These units were modified to operate as bi-stable devices by removing the reset circuitry of the original design. The "and" gates and pulse forming circuits were RCA CD2150 integrated circuits and their use and details of connection are described in RCA ICAN-5025. The characteristics of the discriminator circuitry are enumerated in Table 23.

The performance of the unit under actual run conditions is shown in Figure 25. These data were taken with 600 MeV protons incident on an oxygen target. The graph shows the ratio of signal to background for PSD IN/PSD OUT. The error bars are due to statistical fluctuations. From this figure it may be seen that the pulse discriminator provides a factor of two reduction in background over the energy range of .5 to 6 MeV.

An additional advantage of this method of pulse shape discrimination is that it rejects analysis of events in which two γ rays

occur with .05 to .5 μ sec of each other, thus eliminating another source of background, i.e., pulse pile-up. The details of this rejection may be seen in Figure 22d which shows the waveforms for two pulses occurring within the previously stated time interval. Even though a "good" event signal is presented by the pulse shape discriminator, it occurs with the wrong time relation to the leading edge of the input signal. Both signals will thus be rejected; the first by the pulse shape discriminator, the second by subsequent timing stages.

APPENDIX D

The charge sensitive preamplifier constructed for this experiment had three main design objectives:

1. to make a minimum contribution to the noise of the linear signal,
2. to maintain a large high-frequency bandpass in order to accurately determine the time distribution of charges delivered by the γ -ray detector, and
3. to involve relatively short integration times so as to withstand high instantaneous rates.

These objectives were met with a single charge-sensitive feedback loop amplifier with a high-gain, high-bandpass field effect transistor (FET) in the first stage.

In comparison to other units, the final preamplifier exhibited a relatively large noise contribution limiting the resolution of the linear signal (see Table 23). For the present application which involved Doppler broadened lines, this resolution proved sufficient. The short integration time and fast rise time this loss of resolution permitted, allowed effective pulse shape discrimination (see Appendix C) and sustainment of much higher instantaneous data rates. The final design was thus a compromise with background suppression and count rate being stressed,

Figure 26 shows the feedback configuration used. The response function of this circuit for large open-loop gain is given by

$$V_{\text{out}}(t) = -\frac{e^{-t/RC}}{C} \int_0^t i(t') e^{t'/RC} dt' \quad \text{D(1)}$$

where:

$i(t')$ is the input current signal, and

R and C are the feedback resistance and capacitance, respectively.

Equation D(1) is obtained from the loop equations for Figure 26.

For the case of a current signal whose time duration t' is $\ll RC$ this reduces to the familiar form:

$$V_{\text{out}}(t) = \frac{q}{C} e^{-t/RC}$$

where

$$q = \int_0^{RC} i(t') dt'$$

A detailed schematic diagram of the complete preamplifier is given in Figure 27.

The first stage (region enclosed in dashed box in Figure 27) of the preamplifier was enclosed in a separate removable housing to provide shielding and to allow cooling of the FET if this became necessary. The first gain stage is a boot-strapped cascade stage for good high-frequency response. This is followed by a predriver (q3, q4) and a symmetric cable driver (q5, 6, 7, 8). The AC feedback consists of L1 (to suppress high frequency oscillations) and C. The DC feedback is accomplished by biasing transistor q9 as a constant

current source. The variable resistor R_2 allows adjustment of the DC operating point of the FET. The output is series terminated and resistor R_1 allows matching to various cable impedances. Parasitic suppression resistors were included in all appropriate transistor leads and supply voltages were isolated upon entry into the circuit.

Tests were made of preamplifier noise versus integration time constant. These indicated that our relatively short integration time doubled the best figure obtained (5 keV FWHM for an integration time constant of 10^{-3} sec). The value chosen was thus the best compromise to satisfy design objectives. The large high-frequency bandpass made the preamplifier sensitive to input capacitance. It showed instabilities when the input capacitance was not properly matched. In practice a range of 20 to 75 pF could be tolerated with no degradation in performance. This range could be altered by changing in value of L_1 in the feedback loop.

The final specifications for the preamplifier are given in Table 23.

The circuit was constructed on a printed circuit base and housed in an 8-inch section of 3-1/2 x 1-1/4-inch aluminum wave guide.

APPENDIX E

The derivation of accurate timing signals from the charge delivered by lithium drifted germanium detectors is complicated by two factors:

1. statistical variations in the charge collection process, and
2. variation in rise time due to the location of the γ -ray interaction in the detector and differing mobilities for electrons and holes. This second factor leads to variations in rise time of from 20 to 60 nsec for a typical detector (see equation C(1)).

Due to the variations in rise times the zero-crossing technique of timing is not advisable since the zero-crossing time of a doubly differentiated signal corresponds to the half amplitude point of the input signals. This can be seen as follows:

Figure 19a shows a typical double delay line clipping circuit. With the input signal of Figure 19b, i.e., a monotonically increasing signal $f(t)$ from $t = 0$ to $t = t_1$, $f(t) = 0$ for $t < 0$ and $f(t) = 1$ for $t > t_1$ the output of the clipping circuit is

$$g(t) = f(t) - (A+1) f(t-D1)$$

where: A is the gain of the second stage and $D1$ is the delay period of the delay lines ($D1 > t_1$)

$g(t)$ is shown as 3 in Figure 19 and $f(t)$ by 1. The time of interest is when $g(t)$ crosses zero and this occurs for $D1 < t < 2D1$ during which time equation E(1) is valid. Thus, for the usual case of $A = 1$, the time for zero crossing, t_x , is given by

$$\frac{F(t_x - D1)}{F(t_x)} = \frac{1}{2}$$

Since $t_1 < D1$ and $t_x > D1$, $f(t_x) = 1$ and the time of zero crossing corresponds to the half amplitude point of the input function. This timing method is thus accurate only for signals which have constant rise times.

For accurate timing, the timing discriminator threshold should be as low as possible and the timing of this discriminator should be independent of input pulse rise time. The circuit described here is a leading edge discriminator compensated to first order for rise time variations. This also eliminates time slewing due to amplitude variations. Compensation is accomplished by using two discriminators with different thresholds. The time difference between these discriminators is used as a measure of the pulse rise time to adjust the timing signal which is referenced to the lowest threshold discriminator.

Consider the simple circuit of Figure 28a where V is a constant voltage and $v(t)$ is a voltage source. If the switch is closed at time $t = 0$, then the voltage at 1 ($v_1(t)$) is given by

$$v_1(t) = V e^{-t/RC} \left(1 - \frac{1}{VRC} \int_0^t v(t') e^{t'/RC} dt' \right) \quad E(1)$$

where:

R and C are the resistance and capacitance of the circuit elements in Figure 28a,

V is the constant voltage, and

$v(t)$ is the voltage source.

Equation E(1) is obtained by solving the circuit equations for Figure 28a.

$$\begin{aligned} \text{If now } v(t') \text{ takes the form } v(t') &= V_1 \text{ for } 0 < t' < t_1 \\ &= 0 \text{ for } t' > t_1 \end{aligned}$$

where V_1 is a constant voltage ($v(t)$ is just a square pulse of amplitude V_1 and width t_1), and if $t_1 \ll RC$ then $v_1(t)$

$$v_1(t) = V e^{-t/RC} \left(1 - \frac{V_1}{V} \frac{t_1}{RC} \right) \quad \text{E(2)}$$

for $t > t_1$.

Figure 29 shows the timing elements of a typical univibrator. Note that except for the absence of the voltage source, $v(t)$, the circuit is identical to Figure 28a with the collector of q_1 replacing the switch and the base of q_2 sampling $v_1(t)$. If $v(t)$ is included in the univibrator of Figure 29, its period, T, becomes

$$T = RC \ln \frac{V}{V_T} \left(1 - \frac{V_1}{V} \frac{t_1}{RC} \right)$$

where: V_T is the reset threshold voltage of q_2 . The time difference, ΔT , between this circuit and a standard univibrator ($v(t) = 0$) is then

$$\Delta t = T(v(t) = 0) - T(v(t))$$

$$= RC \ln \frac{1}{1 - \frac{V_1}{V} \frac{t_1}{RC}} \approx \frac{V_1}{V} t_1$$

for $t_1 \ll RC$.

For linearly rising signals proper adjustment of V_1 and t_1 will make the fall time of a univibrator fired at fixed threshold independent of its rise time.

With reference to Figure 28b, consider a linearly rising signal $F(t) = a(t + t_2)$ which fires a discriminator with threshold A . For input signals with differing slopes, a , there will exist a difference in the time the discriminator fires. If we consider that the pulses originate at time $t = -t_2$, then t_2 may be considered the timing "error." This discriminator starts the compensated univibrator and turns on $v(t)$. The second discriminator, with threshold NA turns off $v(t)$, thus,

$$t_2 = A/a$$

and

$$t_1 = \frac{A(N-1)}{a}$$

t_1 is the time between disc. 1 (threshold A) and disc. 2 (threshold NA)--(same as t_1 of equation E(2)) and t_2 is the time from origination of signal to disc. 1 (threshold A). Since t_2 is the timing error of the basic univibrator and Δt is the change in its width, if the falling edge of the univibrator is to be properly compensated

$$t_2 = \Delta t$$

which gives

$$\frac{V_1}{V} (N-1) = 1 \quad E(3)$$

In the circuit shown, $V_1 = V$ and the thresholds are thus A and $2A$. Note that the slope, a , of the input signal does not occur in equation E(3); the circuit effectively calculates \underline{a} for each input signal and properly compensates the timing of its output pulse.

Figure 28d shows a block diagram of the circuit and Figure 28c shows waveforms at various locations. Discriminator 1 is set to fire at ≈ 15 mv and return to its initial state after a time slightly less than the positive portion of the input signal. This discriminator starts the compensated univibrator. Discriminator 2 fires at ≈ 30 mv and resets at the zero-crossing time of the input. A coincidence is formed in C1 between (disc 1) (disc 2) the output of which is the correction voltage $v(t)$. The output of discriminator 2 is delayed slightly in D1 to allow for the finite rise time of C1. The output of C1 is delayed slightly in D2 to allow the compensated univibrator to stabilize and is then applied as the correction voltage $v(t)$. $v(t)$ is thus a square pulse whose amplitude is constant and whose width varies depending on the rise time of the input signal. This variation allows compensation of the timing signal assuming a linearly rising input signal. A standard pulse is formed on the trailing edge of the univibrator which is then put into a final coincidence with the output of discriminator 2 to assure that both discriminators fired and that the pulse was properly compensated.

The complete schematic diagram for the circuit is shown in Figures 23 and 29. It should be noted that the fast amplification stages and discriminator 2 were shared with the pulse shape discriminator and all comments in Appendix C concerning them are relevant.